MAMMALIAN AND BACTERIAL TOXICITY OF NANOPARTICLES USED IN HAZARDOUS WASTE TREATMENT AND ENVIRONMENTAL REMEDIATION

Thomas C. Long

A dissertation submitted to the faculty of the University of North Carolina at Chapel Hill in partial fulfillment of the requirements for the degree of Doctor of Philosophy in the Department of Environmental Sciences and Engineering, School of Public Health.

Chapel Hill, NC
2007

Approved by:

Michael D. Aitken, Advisor

Louise M. Ball

Steven W. Peretti

Frederic K. Pfaender

Ivan I. Rusyn

ABSTRACT

THOMAS C. LONG: Mammalian and Bacterial Toxicity of Nanoparticles Used In Hazardous Waste Treatment and Environmental Remediation
(Under the direction of Michael D. Aitken)

The increased use of engineered nanomaterials in pharmaceuticals, materials science, and consumer products has raised questions regarding the potential risks of these nanoproducts to human and ecological health. Environmental applications for in situ site remediation and water treatment can provide a route for human exposure and are especially appropriate for toxicity evaluation. This research investigated the response of bacteria and mammalian nerve cells to commercially available zero-valent iron (ZVI) and TiO_2 nanoparticles. In the first part of the research, immortalized mouse microglia (BV2) responded to non-cytotoxic concentrations of TiO_2 with a rapid and sustained release of reactive oxygen species (ROS) consistent with both the oxidative burst and interference with electron transport. Transmission electron microscopy documented engulfment of aggregates of nanosized particles. A second study found that extended exposure of microglia to TiO_2 produced loss of nuclear staining consistent with DNA degradation. Gene expression analysis in microglia indicated up-regulation of inflammatory, apoptotic, and cell cycling pathways and down-regulation of energy metabolism following TiO_2 exposure. TiO_2 did not produce cytotoxicity in immortalized dopaminergic neurons (N27), but primary cultures with mixed neuronal and glial

populations showed neuronal loss and microscopic evidence of neuronal apoptosis, indicating potential involvement of glia in neuronal cytotoxicity.

Experiments with *Escherichia coli* K-12 indicated that ZVI, but not TiO_2, caused significant viability loss in the absence of photoactivation. Gene expression analysis found that ZVI induced genes in the oxidative phosphorylyation pathway, primarily those associated with electron transport. This result was corroborated by increased respiration following ZVI exposure, consistent with increased activity of the electron transport chain. Neither effect was observed after TiO_2 exposure. Electron microscopy documented localization of ZVI nanoparticles on the cell surface, potentially interfering with maintenance of the proton-motive force necessary for ATP generation. Consistent with its lack of toxicity, TiO_2 induced cell maintenance functions and down-regulated stress response pathways, and did not associate with cell membranes. Considering the results from all studies, it appears that ZVI and TiO_2 provoke different responses in bacterial and mammalian cells and may act via separate modes of action.

ACKNOWLEDGEMENTS

I would like to thank:

- My dissertation advisor, Professor Michael D. Aitken, for his support and guidance, and for modeling a thorough, analytical approach to the conduct of research.
- Dr. Bellina Veronesi for introducing me to and guiding me through the world of neurotoxicology and nanoparticles, and for her encouragement of my research.
- The members of my doctoral committee for their thoughtful comments and insights into navigating the dissertation process.
- My lab colleagues, especially Dr. David Singleton, Dr. Joanna Park, Dr. Aaron Law, Dr. Glenn Walters, Preethi Sama, and Julianne Tajuba, for helpful discussions and creative suggestions.
- Several individuals who provided technical support for various aspects of this research: Dr. Bellina Veronesi of the U.S. Environmental Protection Agency provided leadership and laboratory facilities for the neurotoxicology research. Dr. David DeMarini of the U.S. EPA contributed to the bacterial research with fruitful discussions on experimental design. Dr. Veronesi also provided key laboratory supplies for the bacterial work, including several of the microarrays, the Degussa P25 TiO_2, and the use of a sonicator for preparing nanoparticle suspensions. Drs.

Ram Ramabhadran and Steve Simmons of the U.S. Environmental Protection agency for providing laboratory space and assistance with bacterial culturing. Dr. Joanna Park of the Department of Environmental Sciences and Engineering at UNC provided extremely helpful advice on working with the mutant *E. coli* strains. Dr. Carol Swartz of the Department of Environmental Sciences and Engineering at UNC provided helpful suggestions on nucleic acid purification and quantitation. Mike Vernon of the Neuroscience Center at UNC provided assistance with hybridization and scanning of the microarrays, and Dr. Jianping Jin of the Center for Bioinformatics at UNC provided guidance on analysis software for the raw expression data. Dr. Susan Hester of the U.S. Environmental Protection Agency provided helpful advice on the biological interpretation of microarray data. Dr. Greg Lowry, Dr. Navid Saleh, and Tanapon Phenrat of the Department of Civil and Environmental Engineering at Carnegie Mellon University assisted with physicochemical property measurements and provided iron content analysis. Dr. John Hong of the National Institute of Environmental Health Sciences, RTP, NC provided a gift of the BV2 and N27 cell lines. Wallace Ambrose of the School of Dentistry and Victoria Madden of the Microscopy Services Laboratory at UNC-Chapel Hill provided expert preparation of electron microscopy samples, and Dr. Veronesi obtained electron micrographs of neural cells. Preethi Sama provided expert immunohistochemical staining of brain cell cultures.

- My family, including my late parents, for their unconditional love and support.

TABLE OF CONTENTS

LIST OF TABLES

LIST OF FIGURES

1. INTRODUCTION

1.1 Background

Engineered nanomaterials have generated a large amount of interest recently due to their enhanced physicochemical properties compared to the corresponding bulk phase materials. Nanomaterials are defined as having one or more characteristic dimensions in the 1-100 nm range. Particles of this size have greatly increased surface area and much higher density of surface features (e.g., charge, functional groups) than larger particles, increasing their reactivity and catalytic activity. This makes them particularly suitable for use in pollutant transformation processes in air purification, water treatment, and site remediation. The same properties also create the potential for biological effects in humans and other organisms exposed to nanoparticles.

Two widely used nanomaterials for treatment and remediation are zero-valent iron (ZVI) and TiO_2. Micron-sized particles of these materials are being replaced with nanosize versions to improve treatment efficiency because of their increased surface area and catalytic activity. More than 20 pilot- and field-scale sites have applied nanoscale ZVI for treatment of chlorinated solvents (*1*). It is also being tested for use in reductive treatment of arsenic and other metals (*2, 3*), polychlorinated biphenyls (*4*), and nitrate-containing compounds such as munitions (*5*). As a reductant, ZVI itself is oxidized to form magnetite (Fe_3O_4) and other iron oxides, which have lower reducing power, but can still support heterogeneous catalysis on their surfaces. ZVI is typically injected into the subsurface as a slurry and has

limited mobility, adsorbing to mineral surfaces close to the injection site at length scales of centimeters to meters (*6*). Rapid agglomeration is observed for ZVI, as with other nanoparticles, but the rate is enhanced due to magnetic effects (*7*). Efforts are underway to increase mobility and targeting of non-aqueous-phase contaminants by surface modification of ZVI with polymers and surfactants (*8, 9*).

TiO_2 has been used for photocatalytic applications in combination with UV light to oxidize contaminants in air, drinking water, and soil (*10-13*). TiO_2 acts as a semiconductor when irradiated with UV light of sufficient energy (wavelength <380 nm) to dislodge electrons from the crystal structure. These electrons may recombine or form reactive oxygen species (ROS), which participate in redox reactions with inorganic and organic pollutants (*14, 15*). Of the two primary crystalline forms of TiO_2 in commercial use (anatase and rutile), anatase is the more photoactive. Doping of TiO_2 with other elements such as nitrogen is being pursued to expand the photocatalytic activity into the visible range (*16*). Catalysis in the absence of light activation is greatly reduced or negligible.

Toxicity testing has been identified as a critical part of the development of new nanotechnologies (*17*). A relatively small portion of the overall US research budget for nanotechnology is allocated to health effects research, but initial studies have been conducted in this area to investigate the in vitro and in vivo effects of nanoparticles. Several researchers have examined the toxicity of ZVI or its oxidation product magnetite in mammalian cells, including liver cells and human dermal fibroblasts (*18-20*). Surface coatings such as polyethylene glycol, polysaccharides, and chelating agents have been tested for use with magnetic nanoparticles in drug delivery and imaging and tend to decrease toxic effects (*18, 20-22*). Other studies have found that magnetic nanoparticles coated with dimercapto

succinic acid (DMSA) diminish viability and capacity of PC12 neurons to extend neurites (*23*) and exhibited weak toxicity in human dermal fibroblasts (*22*). TiO_2 has been one of the most studied metal oxide nanoparticles in pulmonary research and has been considered a negative control in some studies due to its low relative toxicity compared to particles such as coal dust, silica and urban particulates (*24-26*). More recent studies have found mammalian toxicity in lung cells and human dermal fibroblasts (*27-29*) and in animals (*30-32*). Inflammatory responses and stimulation of macrophages to produce ROS have been suggested as potential modes of action for toxicity of TiO_2 and other nanoparticles (*33*).

Researchers have found evidence that nanoparticles can cross biological barriers and translocate to other organ systems (*34-37*), including regions in the brain (*38*). Nanoparticles have also been shown to cross the tight blood-brain barrier (*39*), of possible benefit for pharmaceutical applications, but creating concerns about the potential neurotoxicity of environmental nanoparticles. Another reason for such concern is the tendency of nanoparticles to stimulate inflammatory and oxidative stress responses (*40*), which are of particular relevance to the brain due to the involvement of these processes in neurodegenerative diseases such as Alzheimer's, Parkinson's, and amyotrophic lateral sclerosis (*41-44*). The brain's high consumption of energy makes it especially vulnerable to oxidative stress resulting from the leakage of oxygen radicals during electron transport in actively respiring mitochondria (*45*).

The response of the brain to foreign substances is mediated by microglia, phagocytic cells related to macrophages found in other organ systems (*46*). Microglia are activated at a very early stage in the brain's injury response and act to engulf and phagocytize invading microorganisms as well as debris from lysed cells (*47*). Activated microglia also rapidly

release ROS in a process known as the oxidative burst. Overproduction of ROS through prolonged activation is damaging to surrounding tissue (*48*). The occurrence of such activation in association with nanoparticle exposure is a potential mode of action for nanoparticle toxicity in the brain. Another potential source of damaging ROS is escape of superoxide ($O_2^{\cdot -}$) from the electron transport chain in mitochondria, which at low levels is neutralized by intracellular antioxidant mechanisms. Interference with electron transport and oxidative phosphorylation can result in high levels of superoxide, which converts to other damaging species such as hydrogen peroxide, hydroxyl radical, and reactive nitrogen species (*45*).

Toxic effects of metal and metal oxide nanoparticles such as MgO, ZnO, CeO_2, and Ag have been observed in bacteria (*33, 49-59*), with most research to date conducted on silver nanoparticles. Most effects appear to be related to membrane disruption (*33, 49-54*). For example, silver nanoparticles associate with the cell membrane and cause membrane damage leading to leakage of cellular contents and interference with the proton-motive force necessary for ATP generation (*54*). Other types of nanoparticles, such as fullerenes (*55, 56*), have been observed to be toxic to bacteria, and this toxicity is mitigated by surface derivatization. Although photoactivated TiO_2 is used in antimicrobial applications, in the absence of light it is less toxic to bacteria than other oxide nanoparticles (*50*). No published reports are available on nanoscale ZVI toxicity to bacteria or other organisms in the environment. The limited evidence available to date indicates that particle composition, as well as charge and other surface properties, affect the biological response to nanoparticles.

1.2 Objectives

The objectives of this research were to investigate the toxicity and gene expression profiles of commercially available ZVI and TiO_2 nanoparticles in bacteria and neural cells involved in oxidative stress. In the first part of the research, the response of immortalized mouse microglia to non-cytotoxic concentrations of Degussa P25 TiO_2 (P25) was evaluated by measuring ROS release and examining the engulfment of P25 by the cells. Physicochemical properties of P25 suspensions in biological buffers were measured at time points and concentrations relevant to the biological response.

The second objective was to examine the possible toxicity of P25 to immortalized microglia and neurons as well as primary cultures of mixed glial and neuronal populations. Microglia were examined for DNA degradation after extended exposure to P25, and gene expression analysis was performed on microglia exposed to sub-lethal concentrations of P25 to identify pathways associated with induced and repressed genes. The effect of P25 on viability of immortalized neurons was measured, and primary cultures were examined for neuronal loss and evidence of apoptosis using immunohistochemical staining.

The third and final objective was to investigate the potential effects of commercially available ZVI and TiO_2 nanoparticles on bacteria. The viability of *Escherichia coli* was determined following ZVI and TiO_2 exposure, and gene expression analysis was performed on *E. coli* cultures using whole-genome microarrays following sub-lethal exposures to these particles. An OS-sensitive mutant strain was used to evaluate the possible role of oxidative stress in toxicity. The effect of these nanoparticles on oxygen uptake and energy metabolism was determined with respirometry, and the association of the particles with the cells was examined using both scanning and transmission electron microscopy.

1.3 Organization of the Dissertation

The dissertation is organized into three main chapters, each devoted to one of the primary research objectives, followed by a chapter that summarizes the conclusions of the research. Each of the three main chapters is a published paper or a draft manuscript intended for submission to a peer-reviewed journal. The summary and conclusions chapter discusses the relationships among the findings, reviews possible mechanisms for the observed effects, suggests future research, and describes the implications of the research for human health, environmental effects, and treatment and remediation strategies.

Chapter 2 has previously been published (Long, T.C.; Saleh, N.; Tilton, R.D.; Lowry, G.V.; Veronesi, B. *Environ. Sci. Technol.* **2006**, *40*, 4346-4352). Chapter 3 has been published online (Long, T.C.; Tajuba, J.; Sama, P.; Saleh, N.; Swartz, C.; Parker, J.; Lowry, G.V.; Veronesi, B. *Environ. Health Perspect.* **2007**, doi:10.1289/ehp.10216). Chapter 4 is a draft manuscript intended for submission to a peer-reviewed journal. The co-authors for each manuscript are listed in a footnote at the beginning of the corresponding chapter.

2. TITANIUM DIOXIDE (P25) PRODUCES REACTIVE OXYGEN SPECIES IN IMMORTALIZED BRAIN MICROGLIA (BV2): IMPLICATIONS FOR NANOPARTICLE NEUROTOXICITY*

2.1 Introduction

The novel physical and chemical properties of engineered nanoparticles make them attractive for use in medical, agricultural, industrial, manufacturing and military sectors. Although hundreds of tons of nanoparticles enter the environment annually, little is known of their interactions with biological systems, and recent studies indicate that some are not completely benign to biological and environmental targets (*60*). Such reports have the potential to transform the focus of environmental protection. The federal government, aware of this possibility, has not only articulated the need for research on the environmental and health effects of nanotechnology (*61*), but is actively supporting such research (*62*). Of the many types of nano-products in current use, toxicity testing should obviously begin with those that pose the highest risk of environmental exposure (*17*). Nanosize titanium dioxide (TiO_2) is a reasonable candidate for study since it is widely used in manufacturing (*63, 64*), in the environment to decontaminate air, soil and water (*12, 13, 65-67*), and more recently in consumer products (e.g. toothpastes, sunscreens, cosmetics, food products, etc.) (*68, 69*). Such widespread use and its potential entry through dermal, ingestion and inhalation routes suggests that nanosize TiO_2 poses considerable exposure risk to humans, livestock and eco-relevant species (e.g., fish, daphnia, nematodes, and plankton). Although exposure to

* Originally published as Long, T.C.; Saleh, N.; Tilton, R.D.; Lowry, G.V.; Veronesi, B. *Environ. Sci. Technol.* **2006**, *40*, 4346-4352.

different TiO_2 particle sizes and formulations (nanosize, pigment grade, and surface coated) has produced only marginal results in rodents (*70-72*), numerous in vitro studies report that TiO_2 nanoparticles cause oxidative stress (OS)-mediated toxicity in diverse cell types, including human colon cells (*73*), osteoblasts (*74*), endothelia (*75*), epithelia (*27*), skin fibroblast (*76*), liver (*19*), alveolar macrophages (*31, 77, 78*) and *Salmonella* bacteria (*79*). The potential neurotoxicity of TiO_2 in culture has yet to be examined.

Several studies report that inhaled or injected nanoparticles enter systemic circulation (*36, 37, 80*) and migrate to various organs and tissues, raising concern that they may cause damage to biological systems through OS pathways (*81*). The brain is especially vulnerable to OS damage, and recent studies indicate that nanosize particles can cross the blood brain barrier (*82*) and enter the central nervous system (CNS) of animals (*35, 37, 38*). In the CNS, OS is largely mediated by the microglia, a macrophage-like, phagocytic cell that is normally inactive unless confronted by potentially damaging, exogenous stimuli (e.g., xenobiotics, chemicals, particles). Their immediate response to such stimuli is known as the "oxidative burst" (*83, 84*) and involves a rapid sequence of events that includes an increase in metabolic activity, a change in cell shape and size, and cytoplasmic engulfment (i.e., phagocytosis) of the offending stimuli. During phagocytosis, the plasma membrane of the phagocyte surrounds the foreign substance, invaginates, and internalizes the membrane bound material (i.e., phagosome). The signaling mechanisms for the subsequent oxidative burst are not well defined, but invagination of the plasma membrane appears prerequisite for the activation of a multi-component enzyme system known as NADPHox and the initiation of the oxidative burst. This activation results in the immediate production of superoxide anions ($O_2^{\cdot -}$) which convert to multiple reactive oxygen species (ROS) including hydrogen peroxide (H_2O_2),

hydroxyl radicals ($OH^{\cdot}$) and peroxynitrites that can destroy the offending stimuli through OS pathways. The excess $O_2^{\cdot -}$ and its dismutation product H_2O_2 are either retained within cytoplasmic granules, providing a immediate supply of intracellular oxidants or allowed to diffuse from the microglial plasma membrane where they can potentially damage the proteins, lipids, and DNA of neighboring cells, especially neurons (*85, 86*). Microglia-mediated neuronal damage through OS pathways has been proposed to underlie neurodegenerative diseases such as Amyotrophic Lateral Sclerosis, Parkinson's and Alzheimer's (*41-43*).

Although the oxidative burst is the major source of ROS in the activated microglia, $O_2^{\cdot -}$ is also generated as a byproduct of normal mitochondrial energy production (i.e., bioenergetics) in the quiescent cell. Mitochondria produce cellular energy (ATP) by transferring electrons along a series of enzymatic complexes (Complex I-IV) known as the electron transport chain (ETC) (*45*). During this transfer, single electrons escape and reduce molecular oxygen to $O_2\cdot^-$. This is the fate of approximately 1% of all oxygen consumed and defines the ETC as the major producer of ROS in non-phagocytic cells and tissues. Although the levels of $O_2^{\cdot -}$ generated from ETC are relatively low and efficiently neutralized by matrix-located antioxidant enzyme systems (i.e., endogenous scavengers), the rate of $O_2^{\cdot -}$ generation can be significantly increased if one or more of the ETC enzyme complexes is inhibited.

The $O_2^{\cdot -}$ formed by the oxidative burst or from ETC leakage is quickly reduced to the more stable H_2O_2 by superoxide dismutase, an enzyme located in intracellular microsomes, peroxisomes and within the mitochondria matrix. Although $O_2^{\cdot -}$ radicals can be directly toxic, they have limited reactivity to lipids. However, in the presence of transition metals, most notably ferrous iron, superoxides can convert to the highly reactive hydroxyl radical

($OH^{\cdot}$) via the Fenton reaction. The hydroxyl radical is considered the primary agent of lipid peroxidation.

Several recent articles have prescribed a formal protocol for nanotoxicity testing (*17, 87*) which suggests that physicochemically described nanoparticles should first be tested in cultures of relevant target cells for the production of ROS. This is followed by toxicity testing in more complex cultures, in eco-relevant species and ultimately in animals. The present study follows this format by first measuring the ROS response of microglia (BV2) exposed to physicochemically characterized nano-TiO_2 (Degussa P25). Microglia were chosen in view of their responsiveness to xenobiotics and their pivotal role in OS-mediated neurodegeneration. The BV2 is an immortalized cell line that responds to pharmaceutical agents, particulates, and environmental chemicals with characteristic signs of OS (*88-90*). In the present study, BV2 were exposed to non-cytotoxic doses of P25, and the immediate and prolonged release of ROS was measured over a 120 min exposure period using various fluoroprobes. Transmission electron microscopy (TEM) was used to document the phagocytic response of the microglia to P25 exposure. Physicochemical properties of P25 (e.g., particle size distribution, zeta potential, and dispersion stability) were measured in culture media and physiological buffer at time points relevant to the biological response.

2.2 Methods

*2.2.1 Physicochemical Characterization***.** Commercial grade, nano-size TiO_2 (Degussa Aeroxide P25) was a gift from Degussa Corp. (Parsippany, NJ) and used without further purification or treatment. Although the physicochemical properties (e.g., particle size distribution, zeta potential, and dispersion stability) of P25 have been previously reported

(*64, 91, 92*), they were re-measured in the present study in the vehicles used to maintain and expose the cell cultures. These included Hank's Basic Salt Solution (HBSS) and Dulbecco's Modified Eagle's Medium (DMEM). Both HBSS and DMEM are high ionic strength solutions with high concentrations of divalent cations that cause P25 to aggregate. DMEM also contains low amounts of glucose and amino acids. The physicochemical properties of P25 were measured in a slurry prepared from a 1 g/L suspension of P25 in HBSS or DMEM. Slurry concentrations (5-120 ppm) similar to those used to expose cells were used immediately after 1 min sonication. The particle size distribution was measured by dynamic light scattering (Malvern Zeta Sizer Nano ZS, Southborough, MA) over a 3 hr period to monitor the growth of the aggregates and to determine a stable aggregate size. For calculating particle size (volume average), the refractive index of the anatase form of TiO_2 (n_D=2.49) (*93*) was assumed. The zeta potential was determined in both HBSS and DMEM from electrophoretic mobility (EM) measurements of a 30 ppm slurry (Malvern Zeta Sizer Nano ZS). The Helmholtz-Smoluchowski equation was used to correlate electrophoretic mobility to zeta potential. The N_2-BET specific surface area was measured using a Nova 2200e BET surface area analyzer (Quantachrome, Boynton Beach, FL). Samples were degassed in helium for 1 hr at 150°C prior to analysis (*94*). The dispersion stability, operationally defined as the resistance to sedimentation, was determined by measuring the sedimentation rate of P25 suspensions in HBSS or DMEM. The optical density (λ=508 nm or 450 nm) of the suspension was monitored for 18 hr in a UV-visible spectrophotometer (Varian, Palo Alto, CA). There was a linear relationship between TiO_2 concentration and UV response for all TiO_2 concentrations evaluated.

2.2.2 Cell Culture Maintenance and Exposure. BV2 microglia were grown in 225-cm^2 cell culture flasks in DMEM supplemented with 10% Fetal Calf Serum (FCS) and 1% penicillin-streptomycin (ATCC, Manassas, VA). After reaching 85% confluency, cells were transferred to Corning 96-well plates. To minimize light scatter during the spectrophotometric readings, cells were plated in clear bottom, black (fluorescence) or white (chemiluminescence) 96-well culture plates (Corning Inc., Corning, NY) and examined with a Molecular Devices (Sunnyvale, CA) Spectramax Gemini EM (fluorescence) or Lmax II 384 plate reader (chemiluminescence). Non-cytotoxic exposure concentrations were determined from measures of intracellular ATP taken after 1, 6, and 18 hr exposure to P25 (2.5-120 ppm) using the CellTiter-Glo® assay. For all ROS measurements, P25 was ultrasonicated (~1 min) in 10X stock concentrations in HBSS and exposed to the cells immediately before spectrophotometric readings were taken.

2.2.3 Probes. Fluorescent and chemiluminescent probes were chosen to measure the immediate generation of H_2O_2 resulting from the oxidative burst and that resulting from interference with mitochondrial ETC (*95*). All probes were purchased from Molecular Probes (Eugene, OR) except for the chemiluminescent assay CellTiter-Glo® (Promega, Madison, WI). The concentrations and incubation times for each assay were empirically derived and are described in the figure legends. For each fluorescent assay, cells, exposed to the fluorescent probe (i.e., "loaded"), were washed with HBSS to remove any extracellular probe from the cell's external environment. In this way, only intracellular levels of ROS were measured. Because it has been reported that P25 can be photo-activated by visible light (*96*),

all cell culture procedures (probe "loading", washings, P25 exposures, etc.) were done under darkroom "safe-lights".

The production of intracellular H_2O_2 generated from the oxidative burst was measured at 3, 5 min intervals with Image-iT™ and at 5-15 min intervals with OxyBURST® H_2HFF Green BSA. For Image-iT, cells were incubated (30 min, 37°C) with 25 µM probe in HBSS, washed and exposed to P25. Fluorescence was recorded at 495/529 nm (excitation/emission). For OxyBURST, cells were incubated with 10 µg/mL (30 min, 37°C) probe in reduced-serum media, washed and exposed to P25. Fluorescence was recorded at 508/528 nm. The production of $O_2^{\cdot -}$ resulting from interference with the mitochondria's ETC was measured using the mitochondrial specific fluorescent probe MitoSOX™ at 20 min intervals over a 0-120 min exposure. Cells were incubated with 2 µM probe (10 min, 37°C), washed, and exposed to P25. MitoSOX fluorescence was recorded at 510/580 nm. Changes in the mitochondrial membrane potential, an indicator of the membrane's net charge, were monitored with MitoTracker® Red over 20 min intervals. Cells were incubated with 25 nM probe (10 min, 37°C), washed, and exposed to P25. Fluorescence was recorded at 579/612 nm. Intracellular levels of ATP, an index of cell viability, were measured at 1, 6, and 18 hr post-exposure with a lucerifase-based chemiluminescence assay, CellTiter-Glo®.

2.2.4 Statistics. All data were collected using SoftMax Pro 4.8 software (Molecular Devices, Sunnvale, CA). Graphing and statistics were performed with either Excel 2003 (Microsoft, Redmond, WA) or GraphPad Prism 4.02 (GraphPad Software, San Diego, CA). The mean value (n=6) at each concentration was graphed to show a time-course response. At least five time points are depicted for each assay. Data were analyzed using an unpaired two-tailed

Student's T-test to determine the lowest statistically significant concentration relative to its unexposed baseline control. The exposure concentration/time point at which a statistically significant difference was observed is indicated on the graphs (*, $p \leq 0.05$) and described in the figure legends.

2.2.5 Transmission Electron Microscopy (TEM). BV2 cells, grown to 85% confluency in 6-well Costar plates (Corning), were exposed to P25 particles (2.5 ppm) in 1% reduced serum DMEM for 6 and 18 hr. After exposure, cells were washed in warm HBSS to remove all non-internalized particles and fixed overnight in cold 4% cacodylate-buffered glutaraldehyde (Poly Scientific, Bayside NY). Cells were centrifuged (1100 rpm, 5 min) and processed as a pellet for TEM using standard procedures (*97*). Polymerized blocks were sectioned at 500-700 nm thickness and examined with a Philips CM12 electron microscope.

2.3 Results and Discussion

2.3.1 Physicochemistry. The toxicity of nanosize particles has been associated with several physicochemical characteristics, such as the N_2-BET specific surface area, the zeta potential, and particle aggregate size. These properties were measured in cell culture media (DMEM) and the physiological buffer (HBSS) used to expose the cells. The N_2-BET specific surface area of P25 was measured at 52.7 ± 3.6 m^2/g and is consistent with the manufacturer's data and with previous reports (*91, 92, 94, 98*). The zeta potentials of P25, measured in DMEM (pH=7.5) and HBSS (pH=7.6) were -11.6 ± 1.2 mV and -9.25 ± 0.73 mV, respectively. The negative surface charge at physiological pH (pH=7.5-7.6) was consistent with the commonly reported isoelectric point of pH_{IEP}=6.4 for Degussa P25 (*92, 94, 98*). Degussa P25 is a

mixture of the rutile and anatase forms of TiO_2 (70% anatase / 30% rutile) with a reported primary crystallite size of ~30 nm (*91*). P25 rapidly aggregates in both HBSS and DMEM. Both HBSS and DMEM are high osmolarity fluids with approximate ionic strengths of 155 mM and 166 mM, respectively, and both contain high concentrations of the monovalent cations Na^+ and K^+ (160 mM) and the divalent cations Ca^{2+} and Mg^{2+} (2 mM). Aggregation

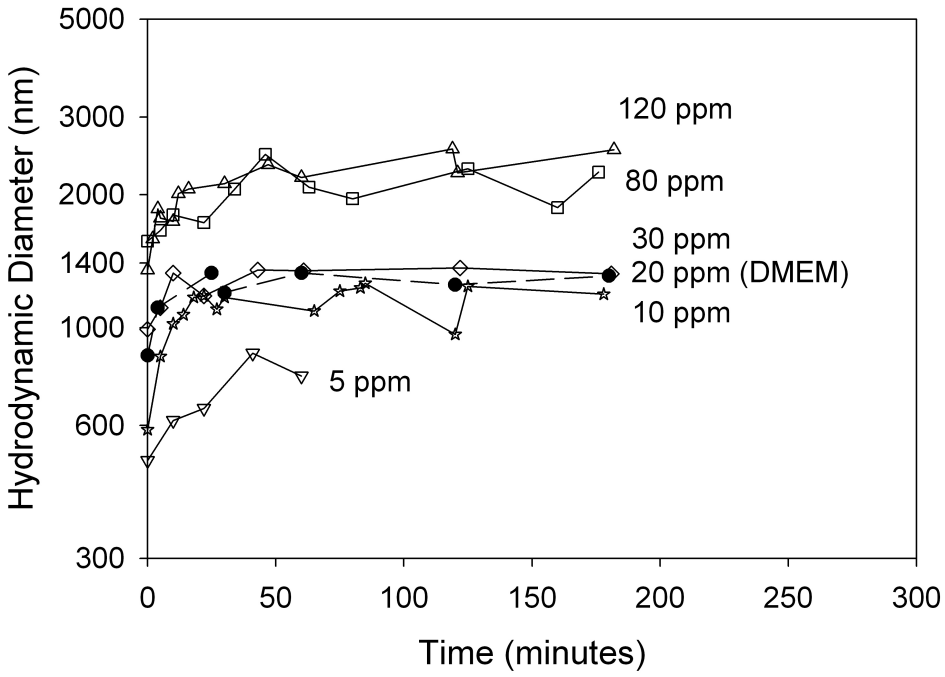

Figure 2.1. Particle aggregation over time at various concentrations of Degussa P25 TiO_2 in HBSS (open symbols) and in reduced serum DMEM (closed symbols). The steady state aggregate sizes are reported in Table 2.1.

continued for 20-45 min after sonication (1 min), until a steady-state stable aggregate size formed (Figure 2.1). The steady state aggregate size increased from 800 nm to 2400 nm as the concentration increased from 5 ppm to 120 ppm (Table 2.1). The size of P25 aggregates was the same in both HBSS and DMEM as these fluids had nearly identical ionic strength

and composition. The amino acids and serum present in reduced-serum DMEM (but not in HBSS) did not significantly affect the rate of aggregation or the size of the aggregates.

Table 2.1. Initial and steady state particle geometric mean hydrodynamic diameter for Degussa P25 TiO_2 in HBSS or DMEM.

TiO_2 Dose Concentration	**Hydrodynamic Diameter (nm)**	
	Initial	**Steady-state**
5 ppm	500 ± 3[a]	826 ± 69[b]
10 ppm	590 ± 3	1164 ± 85
20 ppm	865 ± 32[c]	1284 ± 57[c]
30 ppm	992 ± 19	1316 ± 68
80 ppm	1570 ± 20	2090 ± 180
120 ppm	1350 ± 30	2368 ± 163

[a] Errors represent one standard deviation based on 3 replicate measurements.
[b] Average particle size measured after reaching steady state (~30 min). Error bars represent 1 standard deviation of these values.
[c] Measured in DMEM.

During the 6, 18 hr exposure times described in the TEM studies, BV2 cells (which adhere to the bottom of the cell culture plate/well), were exposed by particle diffusion or sedimentation of aggregates. Such conditions are characteristic of cell culture studies and could produce higher particle exposures than that described by the concentration (*99*). The sedimentation of P25 aggregates was measured in low serum media at 6, 18 hr exposure to estimate the fraction of particles that settled onto the cells during the TEM exposure (Figure 2.2). By the end of the 18 hr exposure ~20% of the particles remained suspended in reduced serum DMEM. The higher sedimentation rate seen at higher concentrations is consistent with larger sized aggregates formed at the higher test concentrations of P25 (see Table 2.1).

A correlation of P25 aggregate size (measured in HBSS) and the concentrations/times needed for significant ROS production is described in the Biological Effects section below.

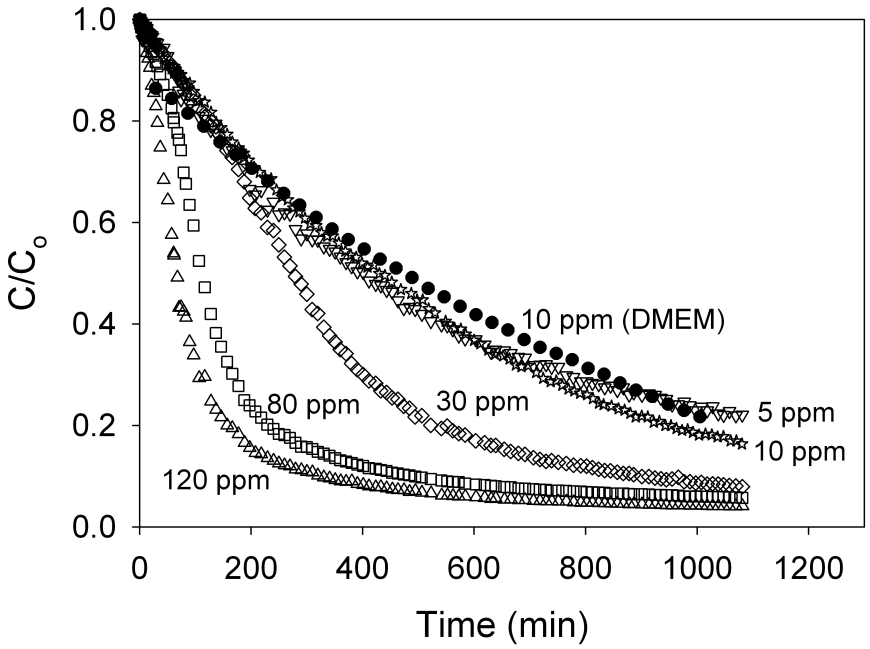

Figure 2.2. Degussa P25 sedimentation over 18 hours in HBSS or reduced serum DMEM at various concentrations. Suspensions were sonicated for 1 minute prior to introduction into a cuvette. Absorbance was linear over the range of concentrations at the wavelengths used (λ=508 nm or 450 nm).

2.3.2 Biological Effects. $O_2^{\cdot -}$ is an unstable molecule which is quickly reduced to the more stable and measurable H_2O_2. Kinetic analysis of H_2O_2 production measured both an immediate production of ROS as generated by the oxidative burst (Figure 2.3-A, 2.3-B) and by later release caused by disruption of mitochondrial ETC (Figure 2.4-A). Microglia responded to P25 (≥ 10 ppm) with rapid (< 3-5 min) concentration-dependent formation of H_2O_2 as measured with Image-iT™ and OxyBURST® (Figure 2.3-A, 2.3-B). In contrast to

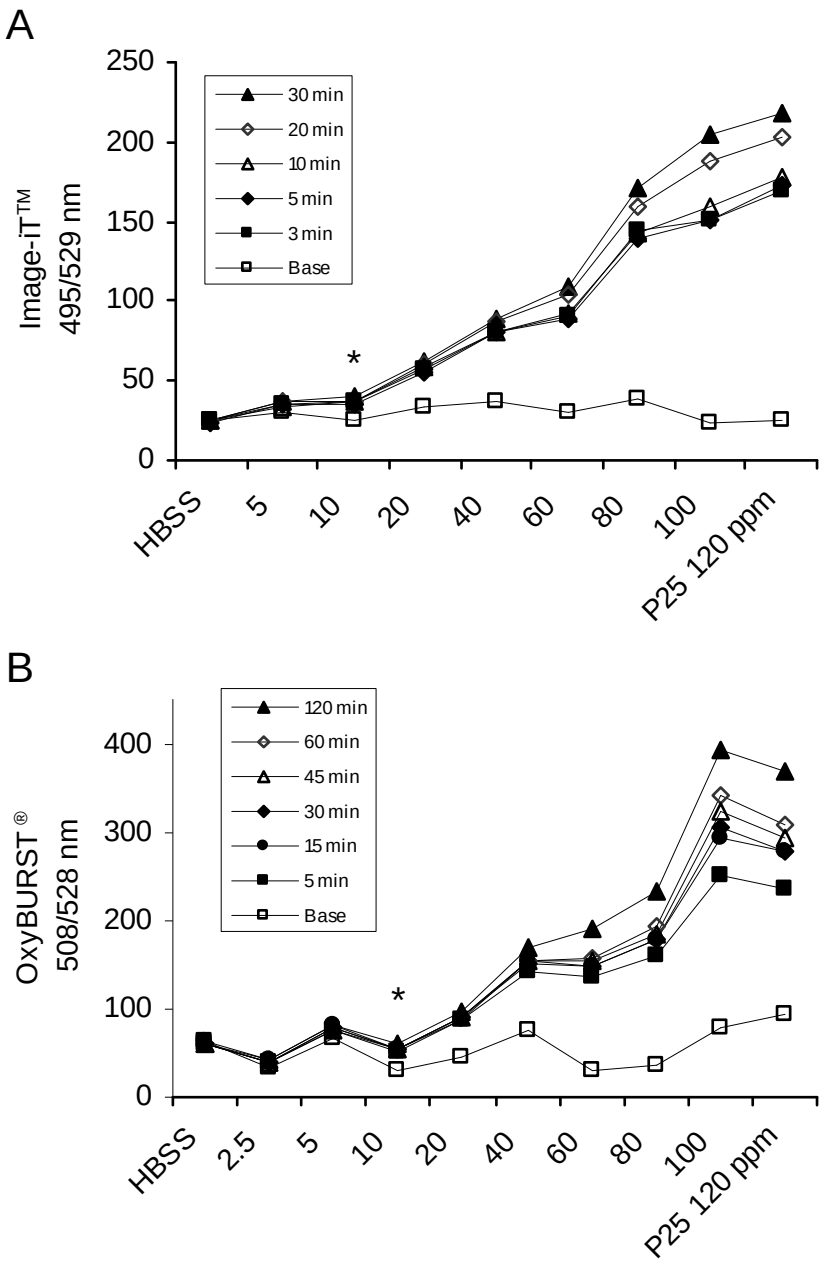

Figure 2.3. The extracellular release of H_2O_2 following P25 exposure was measured using Image-iT™ (A) and OxyBURST® (B). An asterisk marks the lowest concentration/earliest timepoint with a significant ($p < 0.05$) increase in fluorescence relative to baseline, occurring at 3 min for Image-iT and 5 min for OxyBURST.

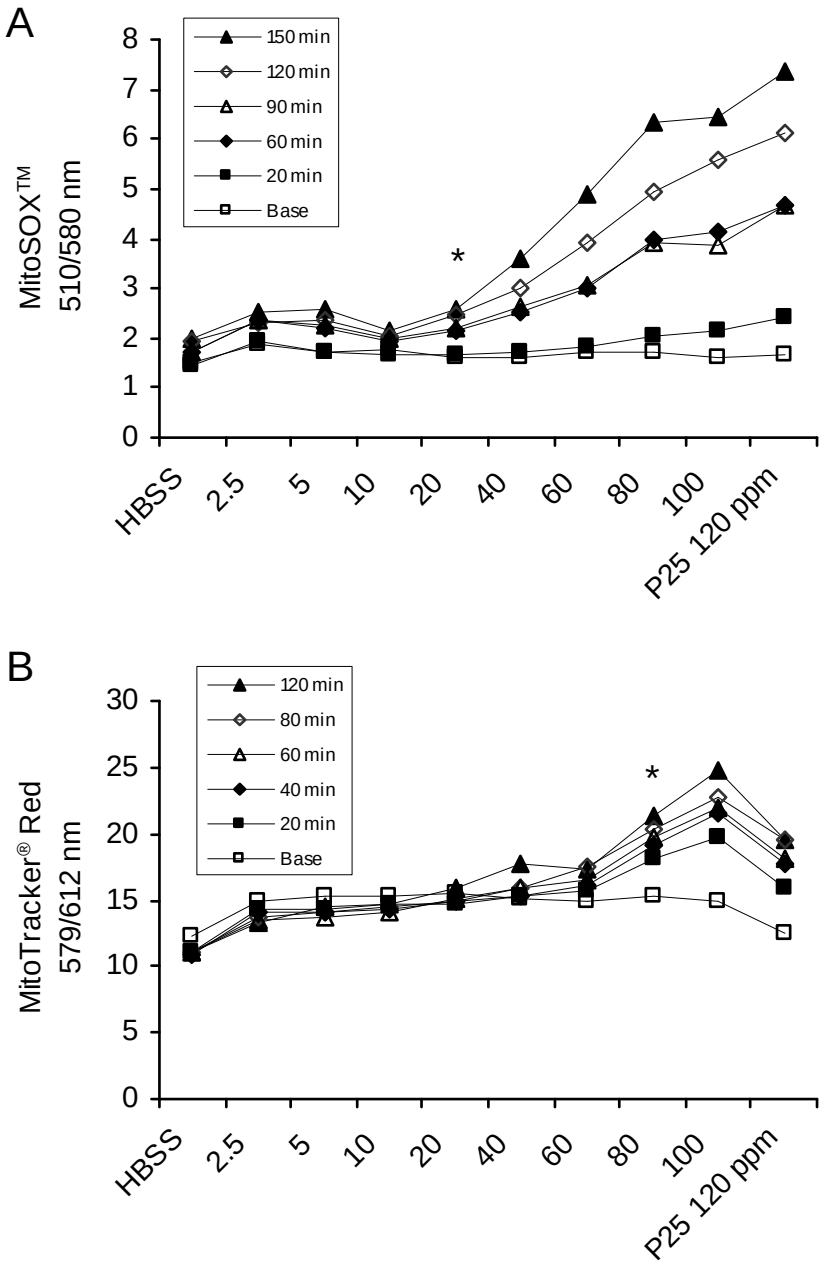

Figure 2.4. (A) Increases in $O_2^{\cdot -}$ were measured by the fluorescent probe MitoSOX™ Red. (B) Mitochondrial membrane potential was monitored with MitoTracker® Red. An asterisk marks the lowest concentration/earliest timepoint with a significant ($p < 0.05$) increase in fluorescence relative to baseline, occurring at 60 min for MitoSOX™ and 20 min for MitoTracker® Red.

the rapid increases in H_2O_2 generated by the oxidative burst, significant release of ROS did not occur until 60 min post-exposure (≥ 20 ppm) as measured by MitoSOX™ (Figure 2.4-A). MitoTracker® Red is a potential-dependent dye. Increases in MitoTracker® Red staining intensity indicate increases in the mitochondria's membrane potential (i.e.,hyper-polarization). The fluorescent MitoTracker molecules, which are initially distributed throughout the cytoplasm, accumulate on negatively charged (anionic) membranes. The increased fluorescence suggests a steady exposure concentration-dependent accumulation of net negatively charged $O_2^{\cdot -}$ within the mitochondrial membrane (Figure 2.4-B). This plausibly resulted from P25's inhibition of one or more of the ETC enzymatic complexes (Complex I, III). Depolarization of the mitochondrial membrane is normally associated with a reduction of membrane permeability, an opening of the mitochondrial transition pore, and the initiation of necrotic or apoptotic pathways (*45, 85*). MitoTracker® Red did not indicate membrane depolarization in response to P25. This was supported by measures of intracellular ATP (Figure 2.5) which were maintained at all P25 concentrations throughout the 120 min exposure period, confirming that all cellular expressions of ROS release were measured in actively respiring and viable microglia.

A correlation between the size of P25 aggregates (Figure 2.2) and the "effective" exposures (i.e., earliest time point and lowest concentration resulting in significant ROS production) was examined. ROS generated from the oxidative burst (Image-iT™, OxyBURST®) indicated that significant increases occurred at 3-5 min in response to ≥10 ppm P25. At this time and concentration, P25 aggregate size was ~750-800 nm. Significant increases in ROS generated from the mitochondrial ETC occurred >60 min exposure, in response to ≥20 ppm P25 as measured with MitoSOX™ probes. At this time and

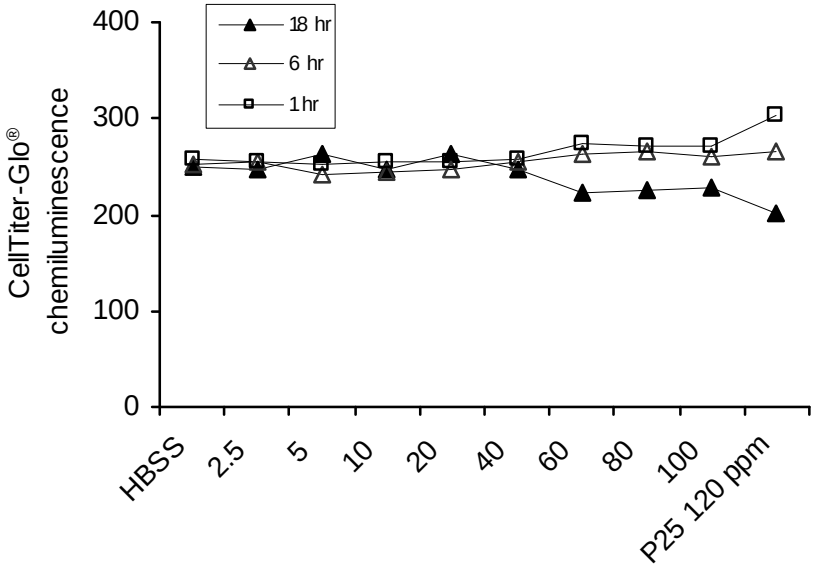

Figure 2.5. ATP levels in BV2 cells measured by CellTiter-Glo® chemiluminescence. ATP levels remained stable at all measured time points, indicating that all ROS and TEM measures were collected on viable microglia.

concentration, P25 aggregate size was ~1300 nm. The relationship between "effective" exposures and aggregate size should be routinely measured in nanoparticle toxicity studies since aggregate size can have a profound impact on the cell's uptake of particles and their response to that uptake.

TEM indicated that after 6 hr exposure, P25 aggregates were phagocytized in small clusters and internalized within the microglia's cytoplasm where they aggregated into electron-dense ~0.5-2 micron clumps (Figure 2.6 A, B). The appearance of small (100-300 nm) and large (800-2000 nm) particle aggregates was consistent with the recorded particle size distribution data (Figure 2.2). Phagocytes (e.g., macrophages, microglia) preferentially engulf particles in the 1-3 µm range (*100*). In contrast, nanosize particles (<100 nm) are not phagocytized in the strict sense, rather, they are engulfed through other, non-specified

mechanisms which involve electrostatic, van der Waals and steric interactions (*101*). Ultrastructural evidence of swollen and disrupted mitochondria lying in close proximity to the aggregates of P25 was recorded after 18 hr exposure (Figure 2.6 C, D). The appearance of swollen mitochondria suggests that the mitochondrial membrane permeability transition

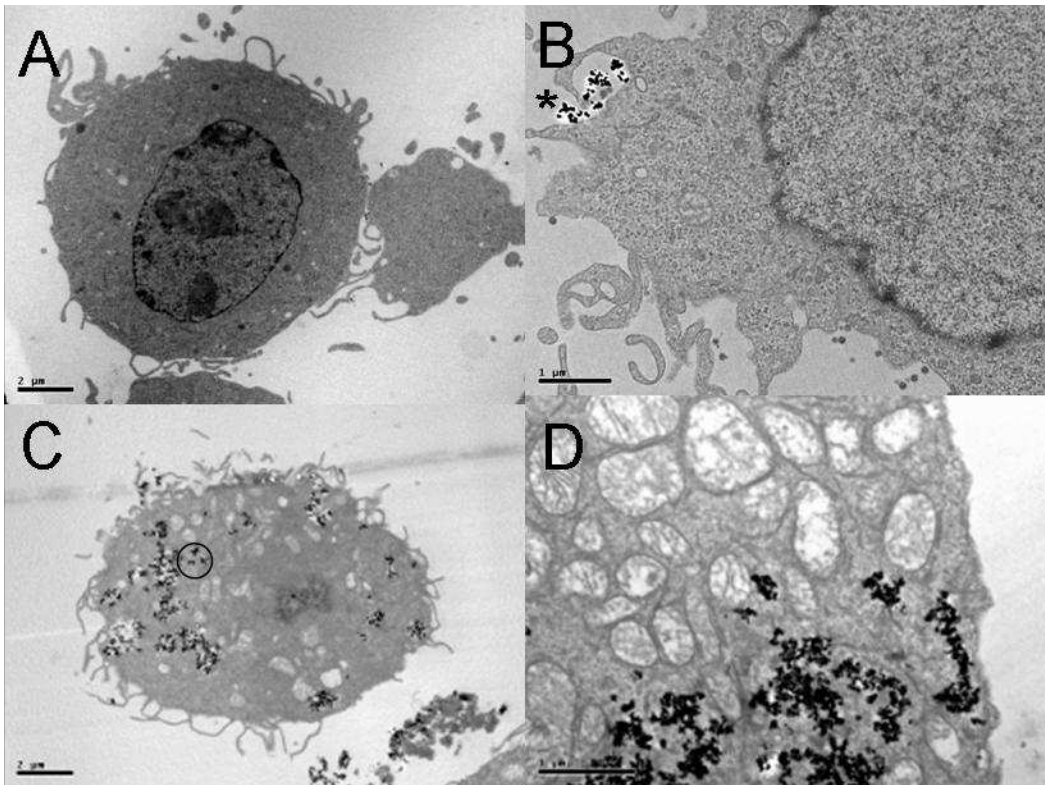

Figure 2.6. Electron micrographs of BV2 microglia exposed to P25. (A) Quiescent microglia are large, 8-10 micron phagocytic cells with many oval-shaped mitochondria visible in their cytoplasm. (B) An early (6 hr exposure) response of microglia to 2.5 ppm P25 was the elaboration of numerous pseudopodia which engulfed small groups of electron-dense particles (*). (C) Within 18 hr post exposure, multiple vacuoles containing P25 aggregates were seen in proximity to pale-staining, swollen mitochondria. (D) Higher magnification showed swelling and disruption of mitochondria lying in close proximity to the aggregates.

pore has begun to open and apoptotic or necrotic signals initiated (*85, 86*). Still, the microglia remained viable in response to P25 exposure, since ATP intracellular levels showed no measurable reductions even after 18 hr exposures (Figure 2.5).

In summary, these data demonstrate that nanosize P25 particles stimulate microglia to produce ROS through the oxidative burst and through interference with mitochondrial ETC. Nevertheless, the microglia remained viable at all concentrations of P25, in keeping with their known resistance to ROS damage (*41, 102*). Whether the microglia's release of ROS translates into neuronal damage *in situ* is not addressed in this study, but pilot data indicate that P25 stimulates apoptotic pathways in cultured neurons at concentrations >20 ppm after 24 hr exposure (*103*). In contrast to earlier reports (*104, 105*), but in agreement with others (*27*), photo-activation of P25 does not appear necessary to stimulate ROS in microglia.

Certain physical characteristics (e.g., surface charge, size, and surface area) of "incidental" nanosize particles such as airborne particulate matter (PM) are known to influence their toxicity. It is plausible that similar physical properties of engineered nanoparticles could affect biological targets through OS or more novel toxicity pathways (*17, 106, 107*). Defining the causal mechanism(s) linking those physical properties with their biological effects should be a primary focus of nanotoxicity studies. Studies on the inflammatory toxicity associated with nanosize particulate matter offer some insights into possible mechanisms. Nanosize PM particles appear to mediate toxicity through OS pathways. The pulmonary inflammation associated with their inhalation has been related to the large surface area of the ultrafine particles which exposes a high number of reactive groups on the particle's surface (*87, 108*). PM inflammation has also been correlated with the negative surface charge carried by the PM particle (*109*). Polymodal, sensory receptors

embedded in the membrane of microglia and macrophages are possible target sites that could react to negatively charged nanoparticles. For example, the activation of TRPV1 vanilloid sensory receptors by the negative surface charge carried on PM particles stimulates OS inflammatory pathways and the subsequent release of inflammatory cytokines from both respiratory epithelial cells (*110*) and BV2 microglia (*111*). Scavenger receptors, found on microglia and macrophages (*112*), are also sensitive to repeating patterns of charge that may be found on ordered crystalline metal oxide nanoparticles. Such receptors have been implicated in mediating cytotoxicity in alveolar macrophages exposed to TiO_2 (*113*). In the present study, the negative zeta potential of P25 particles and the ordered arrangement of charged O^- sites on their surface could be activating either type of receptor and subsequent OS pathways in the microglia. Future studies will examine the causal relationship between the surface charge of nanoparticles and OS mediated events in neurons and other cell types to better understand how the physical properties of particles interact and activate biological systems.

3. NANOSIZE TITANIUM DIOXIDE STIMULATES REACTIVE OXYGEN SPECIES IN BRAIN MICROGLIA AND DAMAGES NEURONS, IN VITRO*

3.1 Introduction

The increased use of engineered nanoparticles in medical, agricultural, industrial, manufacturing, and military sectors raises legitimate concerns as to their adverse effects on environmental and biological targets. Nanosize titanium dioxide (TiO_2) is used in a variety of consumer products (e.g. toothpastes, sunscreens, cosmetics, food products) (*69*), manufacturing, paints and surface coatings (*64*) and in the environmental decontamination of air, soil, and water (*12*). Such widespread use and its potential entry though dermal, ingestion, and inhalation routes suggest that nanosize TiO_2 could pose an exposure risk to humans, livestock, and eco-relevant species. Although earlier studies have reported equivocal toxicity in experimental animals exposed to different particle sizes and formulations (nanosize, pigment grade, and surface coated) (*72*), more recent studies clearly indicate TiO_2 toxicity in eco-relevant species (i.e., *E. coli*, daphnia) (*50*) and mammals (*30, 32*). Numerous in vitro studies have reported OS-mediated toxicity in various cell types (*27-29, 73, 78, 114*). However, the response of nerve cells to nanosize TiO_2 has not been investigated in vitro or in vivo, outside of a companion study (*115*).

Because of their size and unusual properties, nanoparticles can enter the body and cross biological barriers relatively unimpeded. Several studies have reported that inhaled or injected particles enter systemic circulation (in low numbers) and migrate to various organs

---

* Long, T.C.; Tajuba, J.; Sama, P.; Saleh, N.; Swartz, C.; Parker, J.; Lowry, G.V.; Veronesi, B. *Environ. Health Perspect.* **2007**, doi:10.1289/ehp.10216.

and tissues (*35-37*) where they could accumulate and damage organ systems that are especially sensitive to oxidative stress (OS). The brain is one such organ, being highly vulnerable to OS because of its high energy demands, low levels of endogenous scavengers (e.g., vitamin C, catalase, superoxide dismutase, etc.) and high cellular concentration of OS targets (i.e. lipids, nucleic acids, and proteins). Recent experimental studies indicate that nanoparticles can cross the blood-brain barrier (*39*) and enter (in low numbers) the central nervous system (CNS) of exposed animals (*35, 38*).

In the brain, OS damage is mediated by the microglia, a macrophage-like, phagocytic cell that is normally inactive unless confronted by potentially damaging xenobiotics. Their immediate and characteristic response (i.e., "oxidative burst") to foreign stimuli involves cytoplasmic engulfment (i.e., phagocytosis), an increase in metabolic activity, and a change in cell shape, size and proliferation (*48*). The NADPH-oxidase driven "oxidative burst" can be monitored by the immediate production and release of superoxide anions ($O_2^{\cdot -}$) that convert to multiple ROS such as hydrogen peroxide (H_2O_2), hydroxyl radicals, and peroxynitrites. The excess $O_2^{\cdot -}$ arising from the oxidative burst can diffuse from the microglial plasma membrane and damage the proteins, lipids, and DNA of neighboring cells, especially neurons. Current thinking indicates that microglial-generated ROS underlies neurodegeneration (*48*). Although the oxidative burst is the major source of ROS in the activated microglia, $O_2^{\cdot -}$ is also generated as a by-product of normal mitochondrial energy production. This results from the inefficient transfer of electrons along the electron transport chain (ETC) (*45*). The levels of $O_2^{\cdot -}$ generated from the ETC are relatively low and efficiently neutralized by matrix-located antioxidant enzyme systems (i.e., endogenous

scavengers). However, the levels of ETC-generated $O_2^{\cdot -}$ can increase significantly if one or more of the enzymatic complexes in the ETC is inhibited.

To examine the possible neurotoxicity of TiO_2, nerve cells critical to the pathophysiology of neurodegeneration (i.e., microglia, neurons) were exposed to a commercially available nanomaterial, Degussa P25. The BV2 microglia is an immortalized mouse cell line that responds to pharmaceutical agents, particulates, and environmental chemicals with characteristic signs of OS (*88, 89*). Its biochemical, morphological and genomic response to P25 exposure was examined in the present study. Since certain neuronal populations (such as dopaminergic (DA) neurons found in the brain striatum) are especially vulnerable to OS (*116*), the neurotoxicity of P25 was studied in the N27, an immortalized rat DA neuronal cell line (*117*) and complex CNS cultures of embryonic rat striatum, which contains high numbers of DA neurons (*118*). Throughout the study, the physicochemical properties of P25 were described under exposure conditions that paralleled the biological response of these cells.

3.2 Materials and Methods

3.2.1 Physicochemical Characterization. Commercial grade, nanosize Degussa P25 is a mixture of the anatase and rutile forms of TiO_2 (70% anatase/30% rutile). Anatase is the preferred form for use in catalysis due to its enhanced redox activity (*119*). Several physicochemical properties of nanosize particles such as zeta potential (i.e., surface charge) and particle aggregate size (*120, 121*) have been associated with toxicity. A companion study measured the effect of P25 concentration on aggregate size in physiological buffer and culture media (*115*). In the current study, the aggregate size and zeta potential of P25 at a

median concentration (20 ppm) was studied under conditions (vehicle, time point, temperature) that paralleled the biological response. Physicochemical properties of P25 (20 ppm) were measured in Hank's Basic Salt Solution (HBSS) at 25°C over a 120-min period to parallel the exposure parameters of ROS release in microglia. Measures were also taken in low serum (1%) culture media (RPMI 1640) at 37°C over 48 h to parallel the neurotoxic response of N27 neurons. A Zeta Sizer Nano ZS (Malvern, Inc., Southborough, MA) was used to measure the hydrodynamic diameter (size) of P25 using the intensity-averaged distribution and the electrophoretic mobility of P25 was used to calculate its zeta potential using the Helmholtz-Smoluchowski equation.

3.2.2 Cell Culture. Immortalized mouse BV2 microglia and rat N27 mesencephalic neurons were grown, respectively, in Dulbecco's Modified Eagle's Medium (DMEM) or RPMI 1640 medium that was supplemented with 10% Fetal Calf Serum (FCS) and 1% Penicillin Streptomycin (ATCC, Manassas, VA). Neurotoxicity studies, with exposure times ranging from 3-72 h, used low (1%) serum RPMI 1640 exposure media. Tissue plugs of embryonic rat (Sprague-Dawley) brain striatum were purchased (BrainBits^{TM}, Springfield, IL, http://www.brainbitsllc.com) and upon receipt were triturated and plated on poly-D-lysine-coated 96-well plates (Nalge Nunc International, Rochester, NY) in Neurobasal/B27 media (InVitrogen, Carlsbad, CA).

3.2.3 Assays. Fluorescent and chemiluminescent probes were chosen to measure the changes resulting from the oxidative burst and interference with mitochondrial ETC (Invitrogen Corp. 2005). The immediate production of intracellular H_2O_2 generated from the oxidative burst

was measured in BV2 microglia with Image-iT™ LIVE Green, a dichlorodihydrofluorescein diacetate-based compound that reacts with intracellular esterases and fluoresces in the presence of ROS. BV2 cells were incubated (30 min, 37°C) in 25 µM Image-iT™ LIVE Green, washed, and exposed to P25. The production of $O_2^{\cdot -}$ resulting from interference with the mitochondria's ETC was measured by incubating cells in 2 µM MitoSOX™ Red (10 min, 37°C), washing, and exposing to P25. The viability and cytotoxicity of neuronal (N27) cultures were monitored using a lucerifase-based, chemiluminescence assay that measures intracellular levels of ATP (CellTiter-Glo®). Increases of caspase activity, an index of apoptotic entry, was measured in both BV2 microglia and N27 neurons with Caspase-Glo® 3/7. Loss of nuclear material (i.e., cytotoxicity) was measured with Hoechst 33342 (InVitrogen), a fluorescent probe that binds to adenine-thymine-rich regions of double-stranded nuclear DNA and indicates apoptotic loss of nuclear material (Oancea et al. 2006). All fluorescent probes were purchased from Molecular Probes (Eugene, OR) except for the chemiluminescent assays, CellTiter-Glo® and Caspase-Glo® 3/7 (Promega, Inc., Madison, WI).

For exposures, P25 (2.5-120 ppm) was ultrasonicated (~1 min) in 10X stock concentrations in either HBSS or low serum exposure media. For ROS measurements, cells were exposed to the fluorescent probe (i.e., "loaded") and washed with HBSS to remove any extracellular probe from the cell's external environment.

3.2.4 Genomics and Bioinformatics. BV2 microglia were exposed (n = 3 wells/treatment) in 6-well plates to P25 (20 ppm) for 3 h. Total RNA was extracted using TRIzol reagent (InVitrogen), purified, and its concentration determined using a NanoDrop ND-1000

Spectrophotometer (Wilmington, DE). Large-scale gene analysis was performed by Expression Analysis (Durham, NC) using the Affymetrix Mouse Genome 430 2.0 GeneChip oligonucleotide array (Affymetrix, Santa Clara, CA) which measures approximately 39,000 transcripts. Target was prepared and hybridized according to the *Affymetrix Technical Manual* (www.expressionanalysis.com).

Affymetrix CEL files were analyzed using GC-RMA (Wu et al. 2004) for array normalization and estimation of probe set intensities. Significance analysis of microarrays (SAM) (*122*) was used to identify genes differentially expressed between P25-treated samples and the media control. Significantly different up- and down-regulated genes were analyzed by Ingenuity Pathway Analysis (IPA) software (Ingenuity Systems, Redwood City, CA, http://ingenuity.com/index.html) to determine p-values associated with Core canonical (metabolic and signaling) pathways and Tox Solution, which identifies relevant toxicity phenotypes and clinical pathology endpoints. Probesets that related to OS genes were analyzed separately using an IPA master list. The ratio of list genes to pathway genes is presented along with the Fisher exact test p-value. Pathways above a p-value threshold of 0.1 were discarded.

3.2.5 Immunohistochemistry (IHC) and Morphometry. Cultures were fixed for 30 min in 3.7% paraformaldehyde, blocked with a mixture of 1% BSA, 0.4% Triton X-100, and 4% normal horse serum (20 min, room temperature, RT), and incubated in a 1:200 dilution of monoclonal mouse anti-human, neuron-specific enolase (NSE) for 30 min at RT (Dako Inc., Ft. Collins, CO). Visualizaton with streptavidin followed protocol of the LSAB 2 System-HP kit from Dako. IHC stained striatal cultures were analyzed morphometrically for neuronal

loss. Six (10X) photographs of each well (n = 3/treatment) were taken using a Nikon TE300 inverted microscope and a cooled-frame CCD camera (Orca I, Hamamatsu, Inc.). Each digitized image was analyzed using MetaMorph 7.0 software (Molecular Devices). Populations of control, NSE-stained neurons were "binned" according to size and shape parameters using the Integrated Morphometric Analysis mode. The total area of NSE-stained figures (cell bodies with attached axons) that fell within these parameters was calculated and compared to cultures treated with P25 (5 ppm; 6-48 h). Data were collected in Excel 2003 (Microsoft, Redmond, WA) and transferred to GraphPad Prism 5 (Graphpad Software, Inc., www.graphpad.com, San Diego, CA) for graphing of the histogram.

3.2.6 Light (LM) and Transmission Electron Microscopy (TEM). For TEM examination, cells were exposed in 6-well plates to P25 particles (20 ppm) for 3 h. After exposure, cells were washed in warm HBSS to remove all non-internalized particles and fixed overnight in cold 2.5% cacodylate-buffered glutaraldehyde (Poly Scientific, Bayside NY). Cells were processed for TEM using standard procedures (*97*) and examined with a Zeiss LEO electron microscope. LM preparations were examined as toluidine blue stained 1-μm epoxy sections or in unstained glutaraldehyde-fixed samples. Both types of LM samples were photographed with a Nikon TE300 inverted microscope.

3.2.7 Statistics. Spectrophotometric data were collected using SoftMax Pro 4.8 software (Molecular Devices). Graphing and statistics were done using Excel or GraphPad Prism 5. The mean response value (n = 6) of each concentration treatment was calculated. Data from several time intervals were normalized to show a time-course response. Data were analyzed

using a one-way ANOVA with Dunnett's Test to determine significance ($p < 0.05$) relative to its unexposed control. Error bars representing the standard error of the mean are presented for data that are significantly different from the control. The earliest time point and lowest concentration at which a significant difference was observed is indicated by an asterisk.

3.3 Results

3.3.1 Viability of BV2 Microglia. Measures of H_2O_2 released from both the oxidative burst

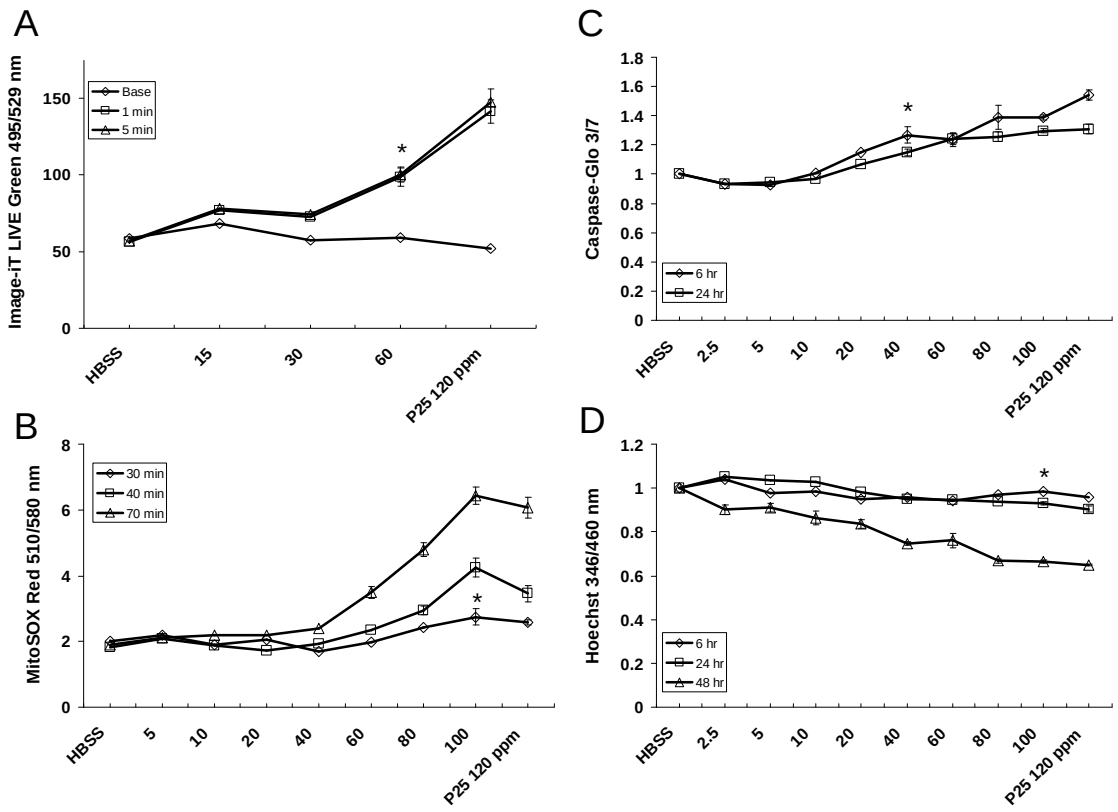

Figure 3.1. Response of BV2 cells to P25 exposure. (A) H_2O_2 released by the oxidative burst as measured by Image-iT™ LIVE Green. Standard error bars indicate significance, and the asterisk indicates the lowest concentration and earliest significant response. (B) Mitochondrial superoxide generation measured by MitoSOX™ Red. (C) Caspase 3/7 activity, an indicator of apoptosis. (D) Apoptotic loss of nuclear material measured with Hoechst stain.

and inhibition of the ETC were collected. BV2 microglia responded to P25 at ≥ 60 ppm with a rapid (1-5 min) release of H_2O_2 as measured with Image-iT™ LIVE Green (Figure 3.1-A). Significant release of $O_2^{\cdot -}$ as measured by MitoSOX™ Red first occurred at 30 min in response to ≥ 100 ppm P25 and only responded to concentrations ≥ 60 ppm after 70 min exposure (Figure 3.1-B). Significant increases in Caspase 3/7 activity, which signal the cell's entry into apoptosis (*45*), were first measured at 6 hr in response to ≥ 40 ppm P25 and remained at this level by 24 hr (Figure 3.1-C). BV2 cells showed reduced nuclear staining in response to ≥ 100 ppm P25 after 24 h and ≥ 2.5 ppm P25 after 48 h exposure as measured by

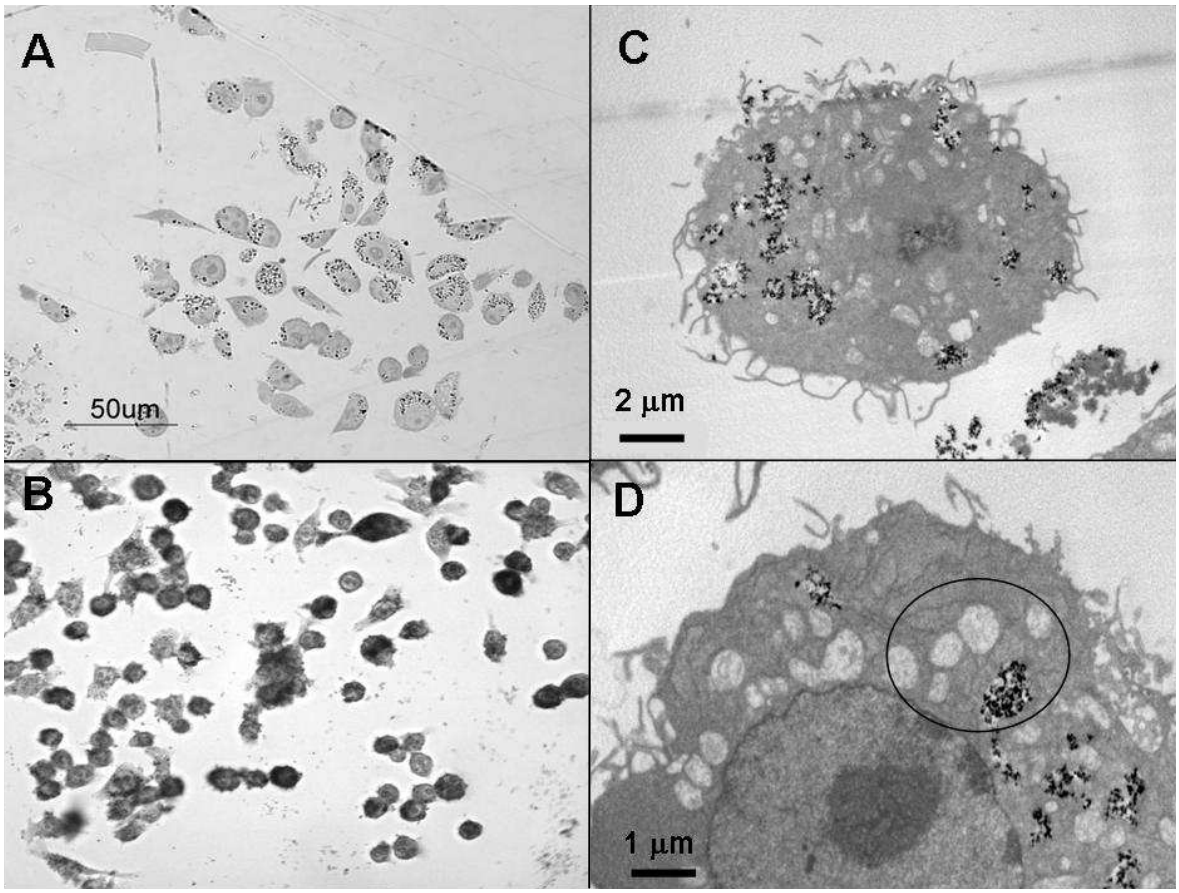

Figure 3.2. Light (A, B) and transmission electron (C, D) micrographs of BV2 microglia exposed to 20 ppm P25. (A) Toluidine blue stained BV2 microglia, 3 h exposure. (B) Unstained, fixed cells exposed to P25 for 48 h. (C, D) BV2 exposed to P25 for 3 h.

Hoechst dye (Figure 3.1-D). LM examination of BV2 microglia exposed to P25 (20 ppm) indicated that they internalized aggregates of P25 in small clusters by 3 h exposure (Figure 3.2-A) and by 48 h responded with fragmented cellular membranes and numerous condensed nuclear figures, suggestive of apoptosis (Figure 3.2-B). Ultrastructural examination of the BV2 microglia indicated phagocytic internalization of the P25 (20 ppm, 3 h) (Figure 3.2-C) and swollen, disrupted microglia in the vicinity of these aggregates (Figure 3.2-D).

3.3.2 BV2 Genomics and Bioinformatics. SAM identified 1755 probesets that were differentially expressed (1195 up-regulated, 560 down-regulated) in P25-treated cultures relative to medium controls. Core analysis with IPA indicated that the up-regulated genes were clustered around signaling pathways involved with B-cell receptor (gene transcription in the immune response), the death receptor (TNF receptor family; apoptotic initiating pathways; caspase activation), apoptosis, calcium and inflammation (NF-κB). Up-regulated cell cycling and maintenance pathways included ERK/MAPK signaling (growth factors for cell proliferation, differentiation, migration, survival, and fate) (Figure 3.3-A). Analysis of the up-regulated genes using the toxicity pathway feature of IPA indicated major pathways associated with inflammation (NF-κB), cell cycling, oxidative stress (peroxisomes) and pro-apoptotic activities (Figure 3.3-B). The down-regulated pathways associated with P25 exposure included several that were associated with adaptive change (e.g., B Cell receptor, ERK/MAPK) and energy production (glycolysis, gluconeogenesis, oxidative phosphorylation) (Figure 3.4-A). Toxicity analysis indicated that pathways triggered by response to low oxygen availability (i.e., hypoxia-inducible factor), peroxisomes, and NRF-2

mediated oxidative stress were also downregulated (Figure 3.4-B). IPA core analysis of OS genes affected by P25 indicated that key energy pathways involving oxidative

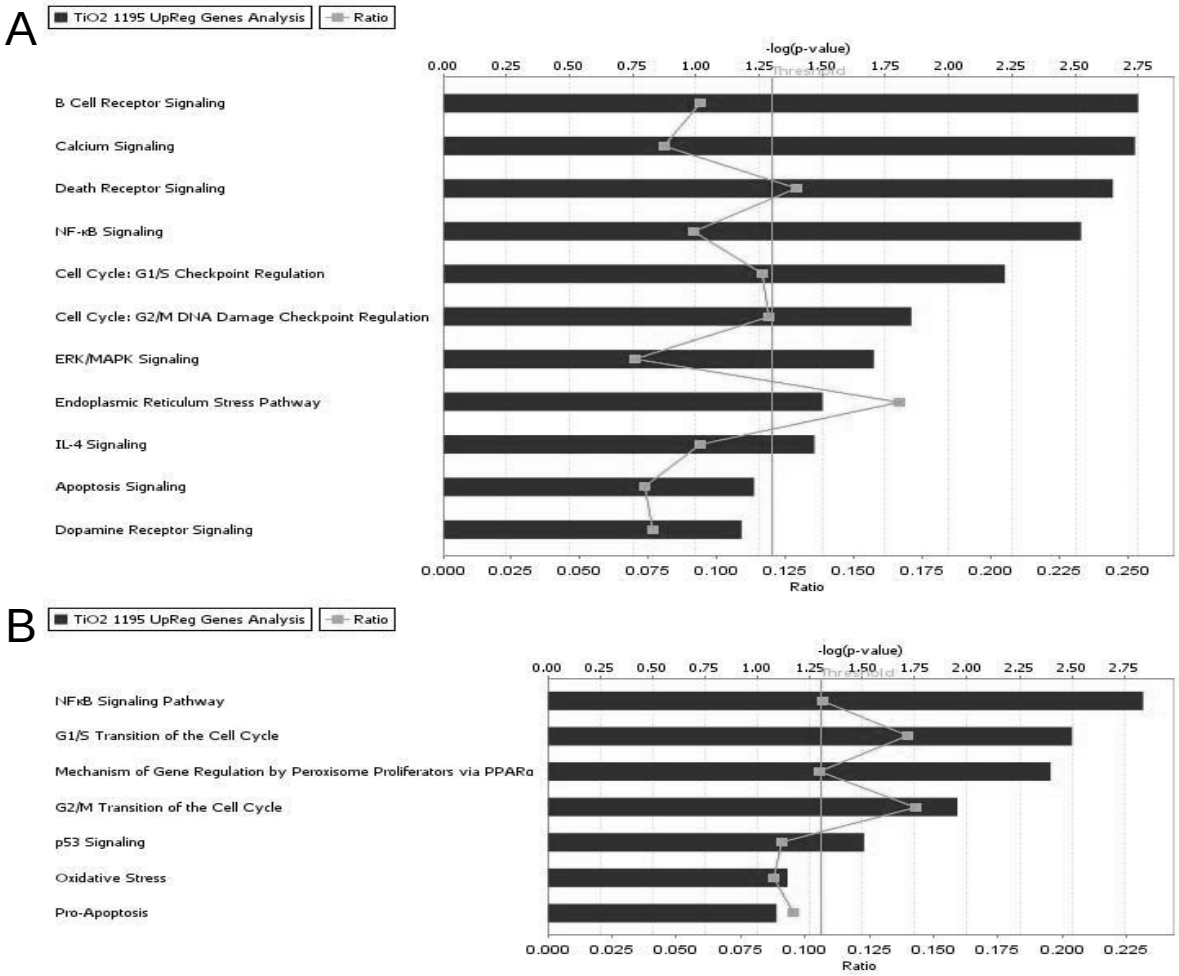

Figure 3.3. Pathways significantly associated with up-regulated genes following exposure of microglia to P25 (20 ppm, 3 h). Ratio represents the fraction of total pathway genes that were identified as up-regulated. (A) IPA core metabolic and signaling pathways. (B) IPA toxicity pathways.

phosphorylation, biosynthesis of ubiquinone (involved in shuttling electrons in the ETC) and the citric acid cycle were primarily down-regulated (Figure 3.5-A). Toxicity pathway

analysis indicated that P25 OS related genes were exclusively clustered around pathways associated with mitochondrial dysfunction (Figure 3.5-B).

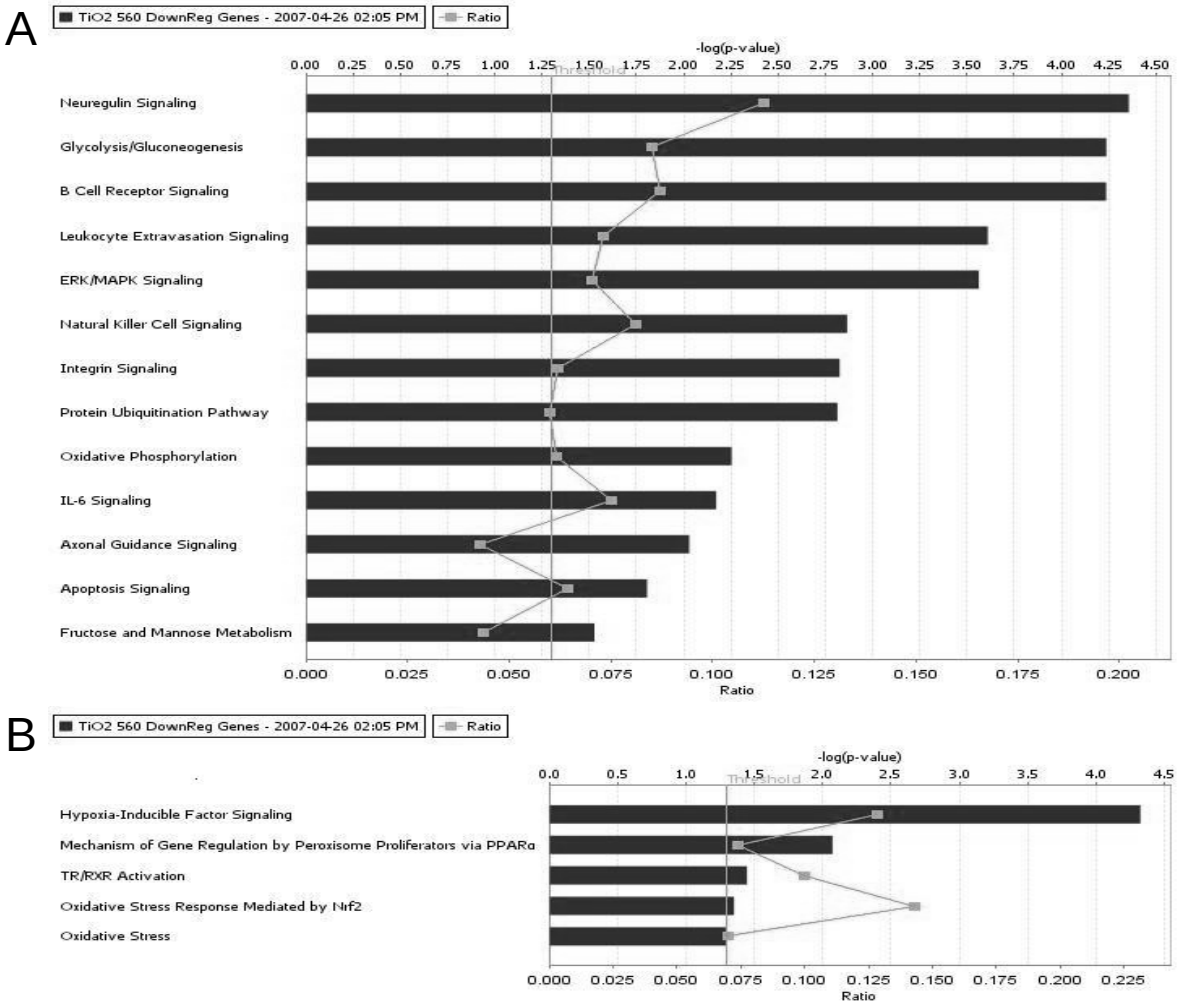

Figure 3.4. Pathways significantly associated with down-regulated genes following exposure of microglia to P25 (20 ppm, 3 h). Ratio represents the fraction of total pathway genes that were identified as down-regulated. (A) IPA core metabolic and signaling pathways. (B) IPA toxicity pathways.

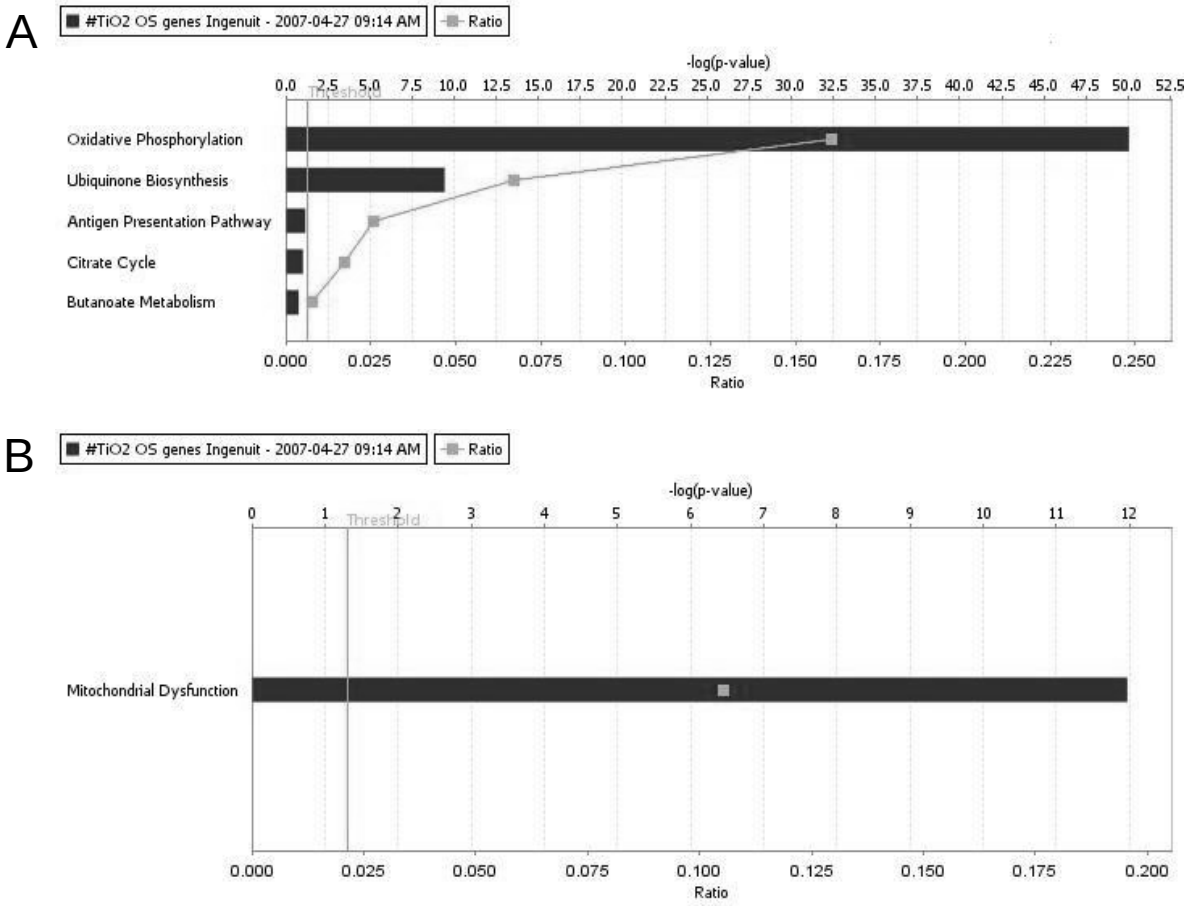

Figure 3.5. Pathways significantly associated with oxidative stress genes following exposure of microglia to P25 (20 ppm, 3 h). Ratio represents the fraction of total pathway genes that were differentially expressed in microglia. (A) IPA core metabolic and signaling pathways. (B) IPA toxicity pathways.

3.3.3 Neurotoxicity. The direct (in the absence of microglia) neurotoxicity of P25 and that mediated by microglia-generated ROS was addressed, respectively, in isolated rat DA neurons (N27) and in primary cultures of rat striatum. P25 increased intracellular levels of ATP in N27 beginning at 1 h (≥ 80 ppm) and continued over 48 h (≥ 40 ppm) (Figure 3.6-A). Caspase 3/7 activity, an indicator of apoptosis, significantly increased at both 24 h and 48 h exposure (≥ 40 ppm) (Figure 3.6-B). Apoptotic damage to isolated N27 neurons, using

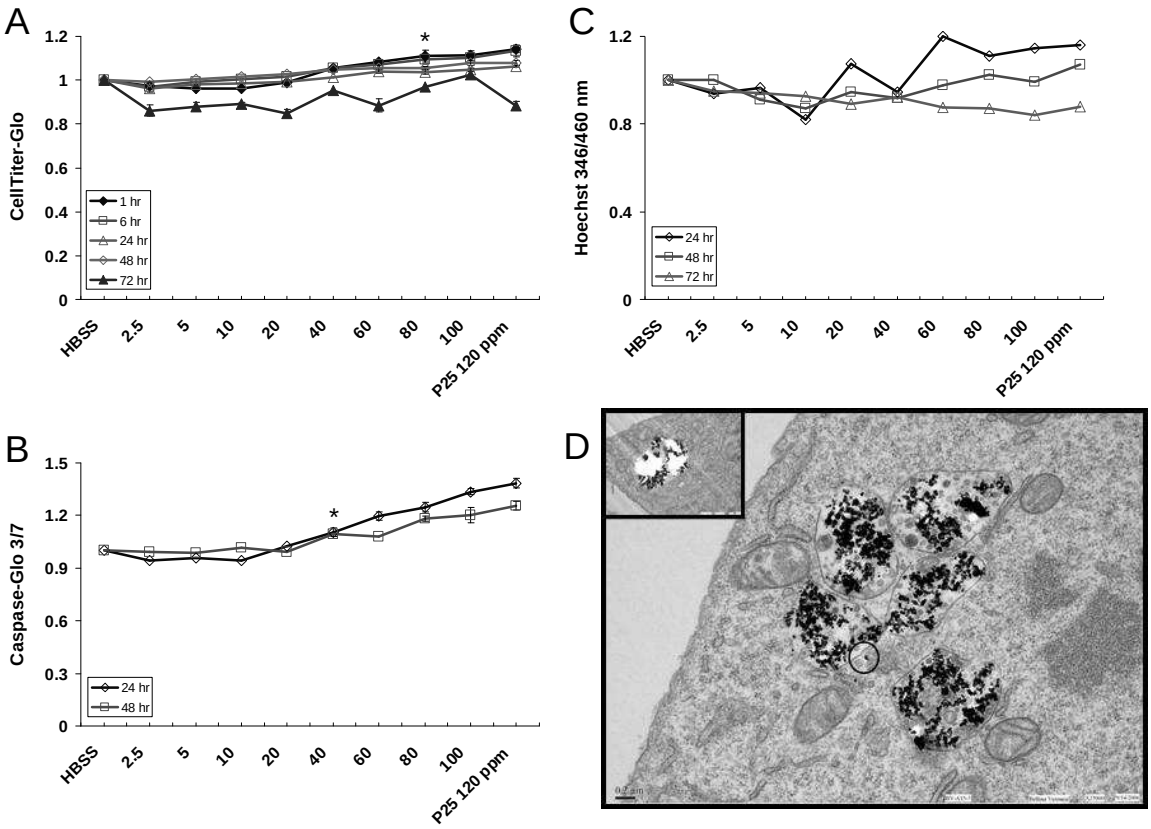

Figure 3.6. Response of N27 neurons to P25 exposure. (A) ATP levels in N27 neurons following exposure to P25. (B) Caspase activity in N27 neurons in response to P25 exposure. (C) Hoechst nuclear staining of N27 neurons after P25 exposure. (D) Transmission electron micrographs of N27 neurons exposed to P25 (20 ppm, 3 h). An amorphous substance was seen within the vacuoles (inset).

Hoechst 33342 nuclear stain, was not seen even after a 72 h exposure to P25 (2.5-120 ppm) (Figure 3.6-C).

Ultrastructurally, both nanosized and large aggregates of P25 were seen in the N27 cytoplasm after 3 h exposure to P25 (20 ppm). P25 aggregates were randomly located thoughout the neuronal cytoplasm (Figure 3.6-D) and appeared to be encased in membrane-bound vacuoles (Figure 3.6-D, inset). No evidence of phagocytosis or pinocytosis (i.e.,

elaboration of pseudopodia) was observed, suggesting that the particles impacted the cell body by sedimentation. In contrast to the disrupted organelles noted above in BV2 microglia, mitochondria appeared ultrastructurally normal in the N27 neurons, in spite of their close proximity to P25 aggregates.

IHC stained cultures of rat brain striatum, exposed to P25 (5 ppm) were photographed (Figure 3.7-A-D) and analyzed morphometrically. Results indicated that the total area of

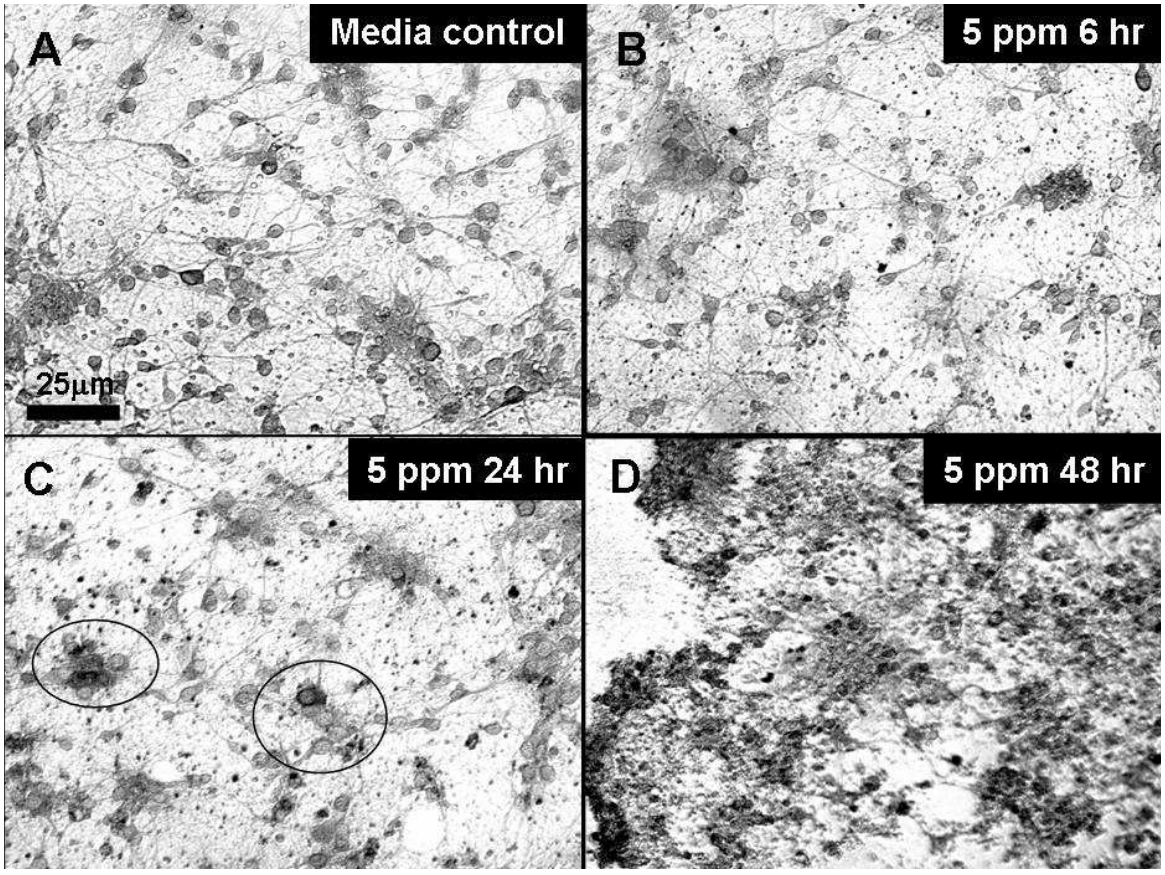

Figure 3.7. Light micrographs of immunohistochemically stained primary cultures of embryonic rat striatum. (A) Untreated confluent cultures containing neurons and glia. (B) Axonal beading and cellular granularity were seen as early as 6 h post-exposure. (C) Evidence of apoptosis (circles) was documented by 24 h. (D) Complete disruption and loss of cellular integrity was noted by 48 h post-exposure to 5 ppm P25.

NSE stained neurons was reduced by 14% after by 6 h exposure and by 19% after 24 h exposure (data not shown).

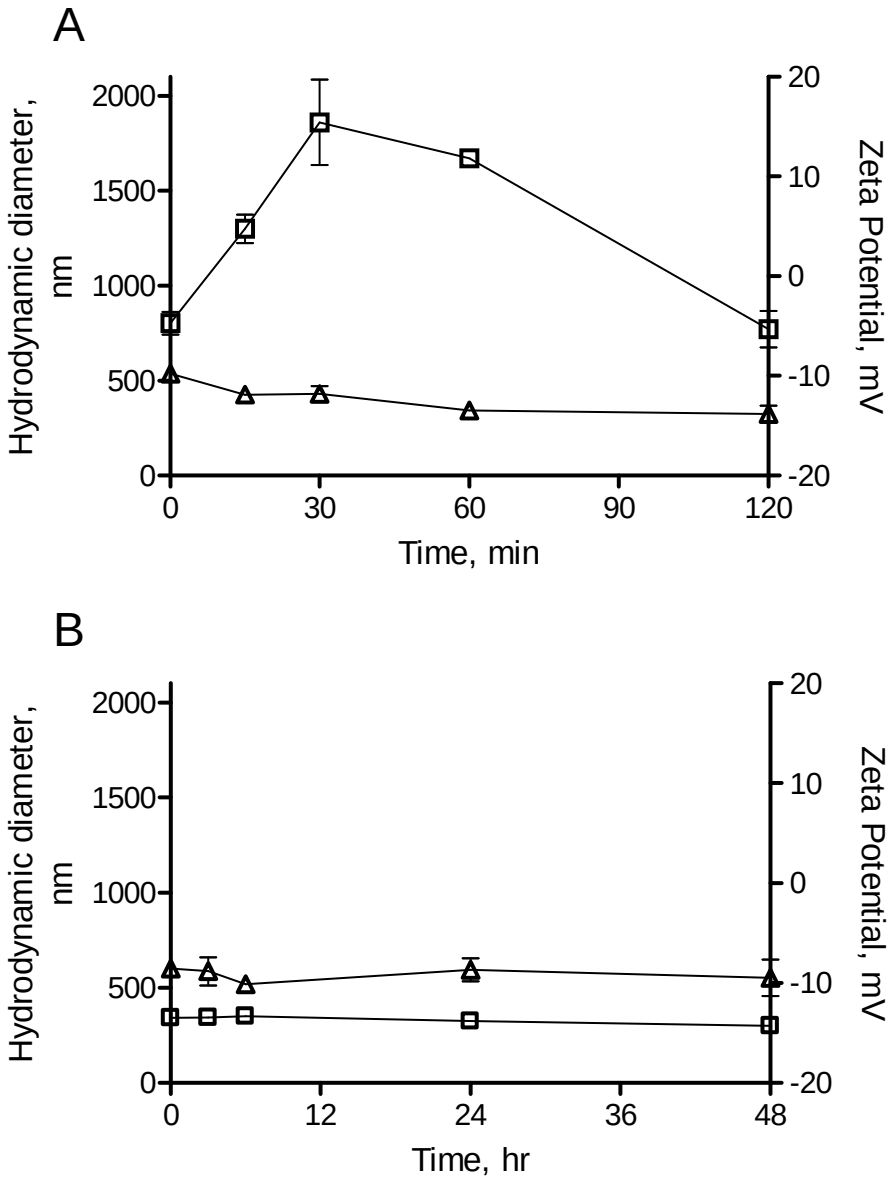

Figure 3.8. Size and zeta potential measurements of 20 ppm P25 in HBSS (A) and RPMI media (B) at times that paralleled the exposure times for the biological responses. Open squares, aggregate size; open triangles, zeta potential.

3.3.4 Physicochemistry. The aggregate size and zeta potential of P25 (20 ppm) were measured in relevant exposure vehicles (HBSS, RPMI) at time points that paralleled the biological response (Figures 3.8-A, 3.8-B). In HBSS, the hydrodynamic diameter of P25 aggregates ranged from 800 to 1900 nm (30 min) and decreased to 770 nm (2 h) as the larger aggregates settled from solution. The zeta potential of P25 (20 ppm) in HBSS (pH = 7.6) ranged from -9.78 to -13.8 mV after 2 h (25°C) (Figure 3.8-A). In low-serum RPMI exposure medium, P25 quickly aggregated but remained relatively stable in suspension (300-350 nm) over the 48 h exposure period. The zeta potential ranged from -8.54 to -10.1 mV over 0-48 h (37°C) in low-serum RPMI media (Figure 3.8-B).

3.4 Discussion

The present data indicate that Degussa P25 stimulates BV2 microglia to release ROS and affects genomic pathways associated with cell cycling, inflammation, apoptosis and mitochondrial bioenergetics. Adaptive pathways such as ERK/MAP kinase signaling (*123*) were differentially affected, indicative of attempts to adjust to the exposure conditions. The significant association of differentially expressed genes with the biosynthetic pathway for ubiquinone, which functions as an electron carrier in the mitochondrial ETC and also acts as an antioxidant (*124*), and with mitochondrial bioenergetic pathways involving oxidative phosphorylation and glycolysis may reflect high levels of ROS and ultimately OS in the cell (*45*). P25 appeared to be non-toxic to isolated DA neurons (N27) even after 72 h. However, when examined in primary cultures of brain striatum which contain microglia, neuronal loss occurred by 6 h in response to only 5 ppm. This shift in dose-response, coupled with cellular and genomic evidence of P25's effect on inflammatory and apoptotic pathways and

disruption of energy pathways in BV2 microglia, suggest that the potent neurotoxicity of P25 seen in complex cultures was mediated though microglia-generated ROS. Apoptosis is a type of OS-mediated cell death (*125*). The microglia's release of H_2O_2 from the oxidative burst and ETC, if excessive, can activate caspase 8 and its downstream effectors caspase 3/7, inducing apoptosis though ''extrinsic'' cell death pathways (*85*). Stimulation of mitochondrial apoptotic pathways (e.g. caspase 3/7) was noted biochemically and by gene-expression analysis in BV2 microglia, and apoptotic morphology was shown in both isolated BV2 microglia and in cultures of striatum. These data indicate that OS-mediated apoptosis played a signature role in P25 neurotoxicity.

Ultrastructurally, the phagocytosis of P25 aggregates by BV2 microglia and the strong association of mitochondrial disruption with these aggregates have been previously reported (*115*). Fractal aggregates can maintain their large surface area, sharp crystallite edges, and other characteristics of individual nanoparticles (*7*). Membrane-bound P25 aggregates were also seen within the N27 cytoplasm. However, no morphological evidence of phagocytosis, pinocytotosis or endocytosis was noted. Because of this, the possibility that P25 aggregates sedimented from the exposure medium onto the cells and became incorporated into cytoplasmic lysosomes cannot be excluded. Nanosize particles were also documented lying free in the neuronal cytoplasm. The manner by which such nanoparticles enter the cell cytoplasm is still a matter of discussion and is thought to involve mechanisms distinct from phagocytosis and endocytosis (*34*); also, no effect of surface charge or particle composition was seen in entry of nanoparticles into red blood cells (*126*). However, particle agglomeration may reduce translocation (*127*).

The biological interactions of nanoparticles are associated with physical properties such as surface area, particle shape, zeta potential, and aggregate size (*120*). For valid interpretation of nanoparticle toxicity data, these properties must be determined under conditions that parallel the biological exposures. These data indicated that the exposure conditions (i.e., vehicle, temperature) significantly modified P25's particle size and zeta potential which could affect its interaction with biological systems and its ultimate toxicity. Particle (or aggregate) size determines if a particle enters the cellular environment though ROS-producing phagocytosis, through endocytosis, or some undefined mechanisms (*128, 129*). The surface charge or zeta potential of a particle affects its aggregation in solution and its behavior in an electric or ionic field. The surface charge of a particle also determines its interactions with specific biological receptors. Polymodal receptors located in the cellular membrane of microglia and macrophages (e.g., TRPV1, Mac-1 etc.) are sensitive to protons (i.e., charge) or repeating patterns of charge (*48, 112, 130*) like those found on crystalline metal oxide nanoparticles. The activation of these receptors triggers various signal transduction pathways that determine the cell's ultimate fate. Scavenger receptors have been implicated in mediating the cytotoxicity of alveolar macrophages exposed to TiO_2 (*113*). Studies have also shown that TRPV1 receptors located on rat primary microglia stimulate OS-mediated apoptotic cell death (*131*). The role of these receptors in mediating P25 apoptosis in BV2 microglia is currently being examined using pharmacological and electrophysiological endpoints.

In summary, this study describes the in vitro neurotoxicity of a widely used nanomaterial, P25. This material appears to be non-toxic to isolated N27 neurons but stimulates BV2 microglia to produce ROS and damages OS-sensitive neurons in cultures of brain striatum.

4. TOXICITY TO *ESCHERICHIA COLI* AND CORRESPONDING GENE EXPRESSION PROFILES FOLLOWING EXPOSURE TO ZERO-VALENT IRON AND TIO_2 NANOPARTICLES*

4.1 Introduction

The enhanced properties of manufactured nanomaterials relative to those of their bulk counterparts has driven much research into the use of nanotechnology in pharmaceuticals, materials science, consumer products, and environmental applications. As of July 2007, more than 500 consumer products claiming to incorporate nanotechnology were on the market (*132*). Environmental uses are another growth area for nanotechnology, with development of applications in sensing, drinking water treatment, air decontamination, and remediation of contaminated soil and groundwater (*4, 133-137*). As research and development on nanotechnology continues, accompanying risk research will be critical for environmental protection and for public acceptance of these technologies (*120, 138*).

Two of the most widely used nanomaterials at present for treatment and remediation are zero-valent iron (ZVI) and TiO_2. Micron-sized particles of both of these materials have been widely used, and nanosize versions are being investigated as improvements due to increased surface area and catalytic ability (*139*). Nanoscale ZVI has been applied at more than 20 pilot- and field-scale sites since 2001 for treatment of chlorinated solvents (*1*), and is being evaluated for treatment of arsenic and other metals (*2, 3*), polychlorinated biphenyls (*4, 134*), and nitrate-containing compounds such as munitions (*5*). ZVI acts as a reductant in the environment, and correspondingly oxidizes to form magnetite (Fe_3O_4) and other iron oxides.

* coauthored with Ambrose, W.; Swartz, C.; and Aitken, M.D.

These oxides have less reducing power, although catalytic activity can occur on their surfaces (*140*). ZVI is typically injected into the subsurface as a slurry and has limited mobility, adsorbing to mineral surfaces close to the injection site at length scales of centimeters to meters (*6*). Rapid agglomeration is observed for ZVI, as with other nanoparticles, but the rate is enhanced due to magnetic effects (*7*). Efforts are underway to increase mobility and targeting of non-aqueous-phase contaminants by surface modification of ZVI (*8, 9*). Despite agglomeration of unmodified ZVI, nano-scale features of the aggregates are still observable (*7*).

TiO_2 has been used for photocatalytic applications in combination with UV light to oxidize contaminants in air, drinking water, and soil (*10-13*). TiO_2 acts as a semiconductor when irradiated with UV light of sufficient energy (wavelength >380 nm) to dislodge electrons from the crystal structure. These electrons may recombine or form reactive oxygen species (ROS), which are available for redox reactions with inorganic and organic pollutants (*14, 15*). Of the two primary crystalline forms of TiO_2 in commercial use (anatase and rutile), anatase is the more photoactive. Doping of TiO_2 with other elements such as nitrogen is being pursued to expand the photocatalytic activity into the visible range (*16*). Catalysis in the absence of light activation is greatly reduced or negligible.

Several investigators have begun to explore the toxicity of nanoparticles, including ZVI and TiO_2. The toxicity of ZVI or its oxidation product magnetite has been examined in mammalian cells (*19, 20, 141*), but no published reports are available on nanoscale ZVI toxicity to bacteria or other organisms in the environment. TiO_2, one of the most studied nanoparticles, has been found to exhibit mammalian toxicity in vitro (*27, 29, 115*) and in vivo (*30, 32*), possibly through inflammatory responses and stimulation of macrophages to

produce ROS. In species that do not possess these response mechanisms, TiO_2 is less toxic in the absence of light than other oxide nanoparticles such as MgO and ZnO, which can disrupt microbial membranes (*33, 50, 58*). Toxic effects on bacteria have also been observed for other types of nanoparticles, such as fullerenes (*55, 56*), which can be mitigated by surface derivatization (*59*). Of the limited evidence available, it appears that particle composition, as well as charge and other surface properties, affect the biological response to nanoparticles.

The present study was designed to extend the research on potential effects of commercially available ZVI and TiO_2 nanoparticles to microorganisms. *E. coli* was chosen as the target species because its physiology is well understood and because whole-genome microarrays are commercially available for *E. coli*. The toxicity to *E. coli* was evaluated for up to 500 parts per million (ppm) ZVI and up to 2000 ppm TiO_2. Gene expression profiles of *E. coli* were then obtained with whole-genome microarrays after exposure to sublethal doses of each type of nanoparticle, and the results were corroborated with other biological endpoints (mutagenicity and respirometry). Electron microscopy was used to examine the localization of nanoparticles in exposed cells, and physicochemical properties of the nanoparticles were measured in the presence and absence of cells to characterize their agglomeration state and charge in biological media. To my knowledge, this is the most comprehensive investigation of effects of environmentally relevant nanoparticles on bacteria conducted to date.

4.2 Materials and Methods

4.2.1 Physicochemical Characterization of Nanoparticles. Nanoscale ZVI was obtained from Toda Kogyo (Hiroshima, Japan) in Februrary 2007 (Lot No. 061203) and stored in an

anaerobic chamber (1% H_2, balance N_2). Single-use aliquots were prepared in the chamber in 1.8-mL crimp-cap vials to limit ZVI oxidation. These particles have a core-shell structure, with a core of Fe^0 and a magnetite shell (Fe_3O_4). The physical and chemical properties of nano-ZVI have been published (*7*, *134*, *142*). The manufacturer reported a primary particle size of 28 nm and a BET specific surface area of 20 m^2/g. The iron content was measured to be 38%. Just prior to use, the slurry was sonicated and diluted 100-fold in phosphate-buffered saline (PBS, Gibco) to yield a 3.3 g/L stock suspension. This stock was further diluted to make 2X working suspensions, which were sonicated (~1 min) prior to bacterial exposure.

Nanoscale TiO_2 (Degussa P25) was obtained as a powder from Degussa Corp. (Frankfurt/Main, Germany). The manufacturer reports the crystal composition of P25 to be approximately 70% anatase and 30% rutile, with a primary crystallite size of 20-30 nm. The BET specific surface area of P25 was previously measured to be 53 m^2/g (*115*). Working suspensions (2X) were prepared in PBS and sonicated (~1 min) prior to bacterial exposure.

Particle size was measured by dynamic light scattering using a Zetasizer Nano ZS (Malvern, Southborough, MA). Both ZVI and TiO_2 formed aggregates that settled to the bottom of the culture tube during incubation/shaking. Samples of the suspension, which included visible bacterial turbidity as well as color indicating the presence of ZVI or TiO_2, were removed after 1 h exposure and analyzed for particle size. Size values are reported as the intensity distribution. Particle size was also measured in the absence of bacteria at t=0 and after 1 h shaking to mimic exposure conditions. Electrophoretic mobility measurements by the ZetaSizer were used to calculate the zeta potential of these suspensions with the Helmholtz-Smoluchowski equation.

4.2.2 Bacterial Cultures. Escherichia coli strain MG1655 (also referred to as *E. coli* K-12) was obtained from the American Type Culture Collection (Manassas, VA). Strain K-12 is a laboratory strain that has been used as the reference for *E. coli* genome sequencing (*143*). *E. coli* strains WP2 *uvrA* / pKM101 (designated strain IC188) and its derivative deficient in the OxyR protein, WP2 *uvrA oxyR* / pKM101 (designated strain IC203) were kindly provided by Dr. Manuel Blanco of the Prince Phillipe Research Institute (Valencia, Spain). These tryptophan auxotrophs are the basis of a reverse mutation assay similar to the Ames *Salmonella* assay for detecting the effect of ROS on promotion of mutagenesis. OxyR is a transcription factor that enhances the expression of antioxidant enzymes such as catalase, alkyl hydroperoxidase, and glutathione reductase (*144*), and its deficiency in strain IC203 is responsible for increased reversion rates relative to strain IC188 under conditions that lead to oxidative stress. Strains were re-isolated prior to reversion experiments according to standard protocols (*145*) on Luria-Bertani (LB) agar plates containing ampicillin; for strain IC203, plates were supplemented with 200 units of catalase to enhance growth.

4.2.3 Viability Assays. E. coli K-12 was grown overnight (~16 h, 37 °C, 250 rpm) in M9 minimal salts supplemented with 2 g/L glucose to reach an OD_{600} of approximately 1 absorbance unit. Cultures were exposed to nanoparticles by mixing with an equal volume of 2X suspension (treated) or PBS (controls). Exposed cultures were shaken and incubated in the dark for 1 h (37 °C, 250 rpm). After exposure, 10^6 dilutions of the cell suspensions were plated on M9-glucose plates (15% agar), incubated for 48 h at 37 °C, and counted for surviving colonies. Cultures were plated in duplicate, and each experiment was repeated at least three times. Statistical significance of pooled values from all experiments was

determined by one-way ANOVA with Dunnett's multiple comparison test.

4.2.4 Reversion Assays. Overnight cultures (14-16 h) of strains IC203 and IC188 were inoculated from frozen stocks and grown at 37 °C (no shaking) in Nutrient Broth No. 2 (Oxoid Ltd, Hampshire, UK) containing 25 µg/mL ampicillin. Pre-existing mutants were counted by plating 0.1 mL of overnight culture on minimal E4 plates (no tryptophan) containing 15 g Bacto-agar and 4 g glucose per liter of Vogel-Bonner E medium (*145*). Cultures were exposed to nanoparticles by mixing with an equal volume of 2X suspension (treated) or PBS (controls). Exposed cultures were incubated in the dark without shaking for 1 h at 37 °C. After exposure, 0.1 mL of culture was mixed with 2.5 mL of warm top agar (6 g/L agar, 5 g/L NaCl) and plated on ET4 plates (E4 supplemented with 0.5 mg/L tryptophan) to count Trp+ revertants arising spontaneously (control) and following exposure (treated). Menadione (2-methyl-1,4-naphthoquinone) and 4-nitroquinoline-1-oxide (4-NQO) were used as positive controls to induce reversion in strain IC203 and strain IC188, respectively.

4.2.5 Respirometry. Oxygen uptake rate (OUR) measurements were made with a water-jacketed reaction vessel (Gilson Medical Electronics, Middleton, WI) fitted with a Clark-type oxygen electrode that was connected to a YSI, Inc. (Yellow Springs, OH) Model 5300 biological oxygen monitor. Data were collected with a WinDAQ (DATAQ Instruments, Inc., Akron, OH) data acquisition system and downloaded to an Excel (Microsoft Corp., Redmond, WA) spreadsheet for processing. A single overnight culture was used for all exposures in each respirometry experiment. Cultures exposed in the same manner as for the viability assays (1 h) were added to the reaction vessel and the OUR measured. To test the

effect of additional substrate, a small volume of concentrated glucose solution was injected to produce a concentration increase of 2 g/L, and the initial rate of oxygen uptake was measured. Net OUR was calculated by subtracting the rate prior to glucose injection from the rate in the presence of glucose. The background OUR of ZVI and TiO_2 in cell-free suspensions was also measured.

4.2.6 RNA Extraction and Microarray Preparation. Overnight cultures of *E. coli* K-12 grown in M9/glucose media (~16 h, 37°C) were exposed to nanoparticle suspensions (1 h) as for the viability assays. Sub-lethal exposure concentrations for ZVI (50 ppm) and TiO_2 (200 ppm) were selected based on viability results. RNA was extracted with the Qiagen RNeasy Protect Bacteria Mini kit (Qiagen GmbH, Hilden, Germany) according to the manufacturer's protocols. Briefly, stabilization reagent was added to preserve the RNA expression profile, cells were enzymatically lysed with lysozyme, and the lysate was passed through a silica membrane to bind nucleic acids. DNase I was added to the membrane to digest DNA. After an ethanol-water rinse, RNA was eluted with RNase-free water. RNA quality (A_{260}/A_{280} ratio) and quantity (A_{260} absorbance) were measured with a NanoDrop (Wilmington, DE) ND-1000 spectrophotometer. RNA samples were also checked for degradation with an Agilent (Santa Clara, CA) 2100 Bioanalyzer. To obtain sufficient RNA quantity and concentration for microarray hybridization, RNA was extracted from duplicate samples and pooled in a 1:1 ratio, then concentrated using a vacuum evaporator. One such pooled and concentrated sample was used for each microarray.

Gene expression was measured using Affymetrix (Santa Clara, CA) *E. coli* 2.0 GeneChip microarrays. These arrays include approximately 5000 probesets from the

MG1655 (K-12) strain. Four arrays were used for PBS-exposed control cultures, and three arrays each were used for ZVI- and TiO_2-exposed cultures. Array hybridization, washing, and scanning procedures followed the Affymetrix GeneChip Expression Analysis Technical Manual. Briefly, cDNA was synthesized from the RNA using random primers, then cleaned up by column purification following NaOH degradation of RNA. The cDNA was fragmented and end-labeled with a biotinylated reagent, then loaded onto the microarray. Arrays were incubated overnight at 45 °C to hybridize fragmented and labeled cDNA to the oligonucleotides on the array. The arrays were then washed, stained with streptavidin, and scanned to measure hybridization intensity.

Pixel intensity values from the scanned images (DAT files) were converted to raw probe intensity values (CEL files) by Affymetrix GCOS software. The CEL files were imported into GeneSpring GX and GC-RMA (Robust Multi-array Average modified to consider probe GC content) was used for background correction and quantile normalization (*146*). The GC-RMA technique enables comparison of expression values across all arrays in the experiment by correcting for intensity differences arising during hybridization and scanning. Based on this analysis and review of the heat maps, one array (for TiO_2) was excluded from further analysis because of much lower overall intensity than the other nine arrays. SAM (Statistical Analysis of Microarrays) (*122*) was used to identify genes that were differentially expressed between treatments and controls. Results were restricted to genes whose expression differed by a factor > 2.0 with a false discovery rate (FDR) (*147*) less than 3%. Lists of up- and down-regulated genes were annotated for pathway and keyword associations using the Database for Annotation, Visualization, and Integrated Discovery (DAVID; National Institute of Allergy and Infectious Diseases;

http://david.abcc.ncifcrf.gov/home.jsp). Additional information was obtained from the primary databases compiled in DAVID, such as UniProt (http://www.pir.uniprot.org/index.shtml). Functional cluster analysis was performed using DAVID to identify common pathways and keywords associated with the entire lists of up- and down-regulated genes for ZVI and TiO_2. This technique uses a statistical approach (Fisher exact test) to determine whether more genes from the list are represented in a certain pathway than would be expected by random selection of genes from the entire genome. In this way, information from the entire list of genes can be used to identify biological themes rather than focusing on a few prominent genes.

4.2.7 Electron Microscopy. Overnight cultures of *E. coli* K-12 grown in M9/glucose media (~16 h, 37°C) were exposed to nanoparticle suspensions (1 h, shaking at 250 rpm) as for the viability assays at the same sub-lethal concentrations used in gene expression analysis. Suspended cells and particles were removed from the culture tubes and gently centrifuged to form a pellet. The pellet was resuspended in fixative (2.5% glutaraldehyde, 2% formaldehyde, 0.1 M cacodylate buffer) and fixed at 4°C for 1 h. For scanning electron microscopy (SEM), a drop of the suspension was placed on a poly-L-lysine-coated glass coverslip and allowed to attach for 30 min. The coverslip with attached cells was briefly washed, taken through a dehydration series (50%, 70%, 95% ethanol for 5 minutes each, then through two rinses of absolute ethanol for 10 minutes each) before critical-point drying (Polaron 3100, Quorum Technologies, Newhaven, UK) using liquid CO_2 as transition fluid. Coverslips were then mounted onto aluminum planchets with carbonized, double sided adhesive tabs and sputter coated (Polaron E5100) with a gold/palladium alloy. Samples were

imaged with a JEOL 6300 scanning electron microscope (JEOL America, Peabody, MA) operating at 15 kV accelerating voltage. The microscope was equipped with an X-ray microanalyzer (Kevex Sigma 3, Thermo Scientific, Waltham, MA) for spectroscopic elemental analysis.

For transmission electron microscopy (TEM), the fixed suspension was pelleted. The pellet was rinsed with 0.1 M cacodylate buffer and post-stained with 2% osmium tetroxide in the same buffer for 1 hour. After thorough rinsing with deionized water, the pellet was dehydrated with a series of ethanol solutions (50%, 70%, 95% five minutes each and then two changes of absolute ethanol for 10 minutes each) and finally transferred to two changes of propylene oxide for ten minutes each. Infiltration with epoxy resin (Eponate 12, Ted Pella, Inc., Redding, CA) was carried with a 50:50 dilution with propylene oxide for four hours with rotation, and then embedding was carried out with resin alone in vacuum overnight at room temperature. The samples were then placed into an oven to cure for two days. Specimen blocks were sectioned at 90 nm and mounted onto uncoated 200 mesh copper grids. Grids were stained with uranyl acetate and lead citrate and imaged with a Philips CM12 TEM (FEI Inc, Hillsboro, OR) at 100 kV accelerating voltage . All images were collected digitally in .TIF format.

4.3 Results

4.3.1 Toxicity to E. coli *K-12.* ZVI significantly reduced viable plate counts relative to unexposed cells after 1 h incubation at concentrations of 100-500 ppm (Figure 4.1-A). A slight, though not statistically significant, loss of viability was observed at 20-50 ppm (Figure 4.1-A). TiO_2 did not reduce plate counts after 1 hr at any concentration tested (50-2000 ppm)

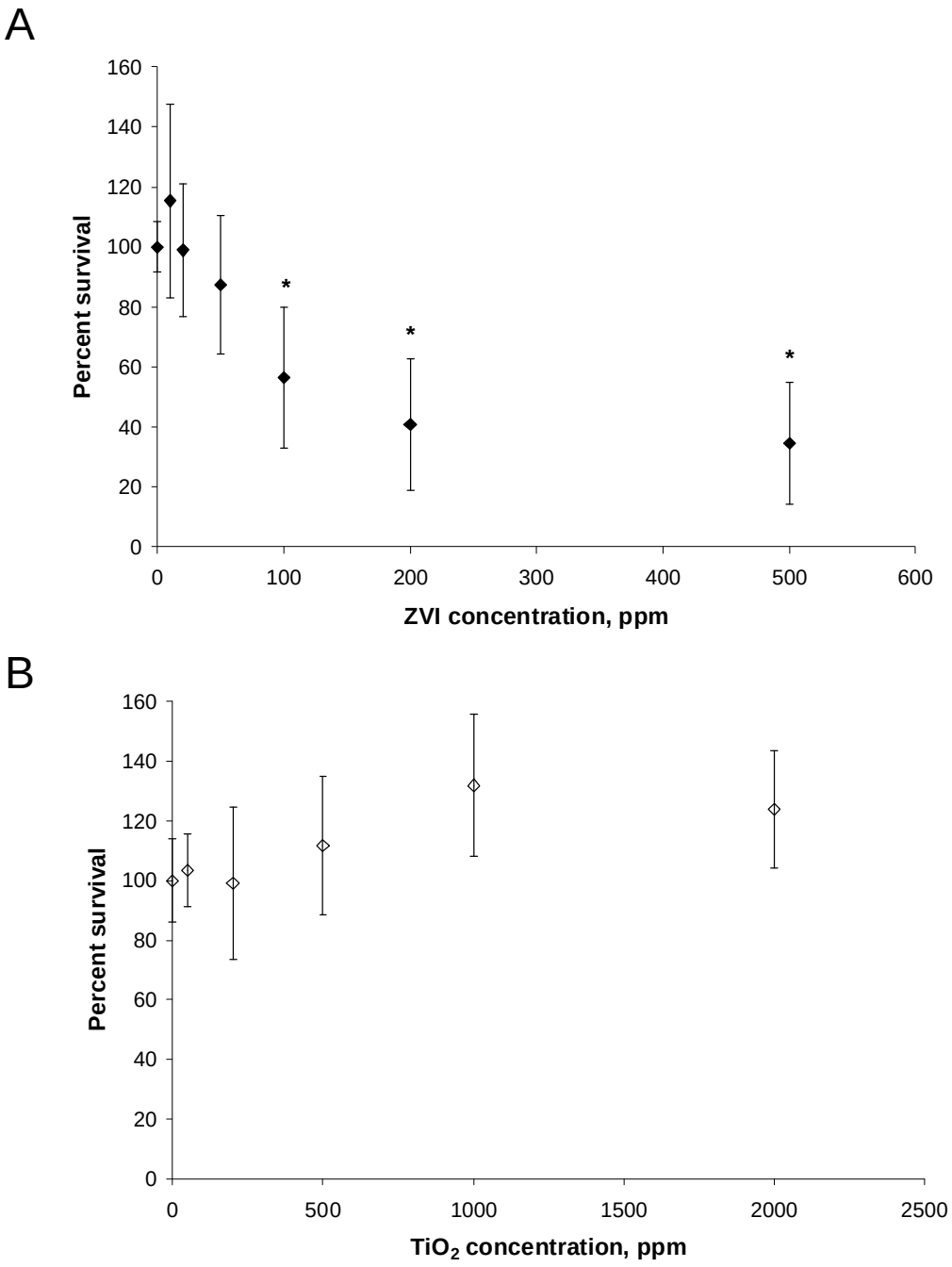

Figure 4.1. Effects on viability of *E. coli* K-12 cultures after exposure to ZVI (A) or TiO_2 (B) for 1 h at 37°C. Values and error bars represent the mean and standard deviation of at least three replicate experiments, each consisting of duplicate plates.

(Figure 4.1-B). Longer incubations (up to 24 hr) did not produce statistically significant reductions relative to 1 h incubations (data not shown). Cultures used for gene expression analysis did not show statistically significant loss of viability relative to controls at a ZVI concentration of 50 ppm or a TiO_2 concentration of 200 ppm.

4.3.2 Mutagenicity Assays. The change in reversion rate for treated cultures relative to control (unexposed) cultures is presented in Figure 4.2. A two-fold increase or greater is considered evidence of mutagenicity (*148*). ZVI exposure (Figure 4.2-A) did not significantly increase the reversion rate for either strain IC203 or strain IC188 at any concentration tested (20-500 ppm). An apparent decrease in reversion rate at high ZVI concentrations, which was not statistically significant, may have been due to toxicity; however, inspection of the plates did not reveal noticeable thinning of the background lawn normally associated with acute toxicity (*145*). Positive controls during ZVI experiments produced a 3- to 4-fold increase in revertants for strain IC203 and a 7- to 8-fold increase for strain IC188. Similar to the results for ZVI, no increase in reversion was observed for TiO_2 in either strain at concentrations of 50-2000 ppm (Figure 4.2-B), and no thinning of the background lawn was observed. Positive controls during TiO_2 experiments produced a 3- to 4-fold increase in revertants for strain IC203 and an 8- to 9-fold increase for strain IC188.

4.3.3 Gene Expression Profiles. A 1-h exposure to ZVI at a concentration (50 ppm) below that observed to cause a significant loss of viability induced overexpression of 141 genes and repression of 162 genes relative to unexposed cultures. The 90^{th} percentile genes with the largest changes (up or down) are listed in Table 4.1. TiO_2 exposure (200 ppm, 1 h) stimulated

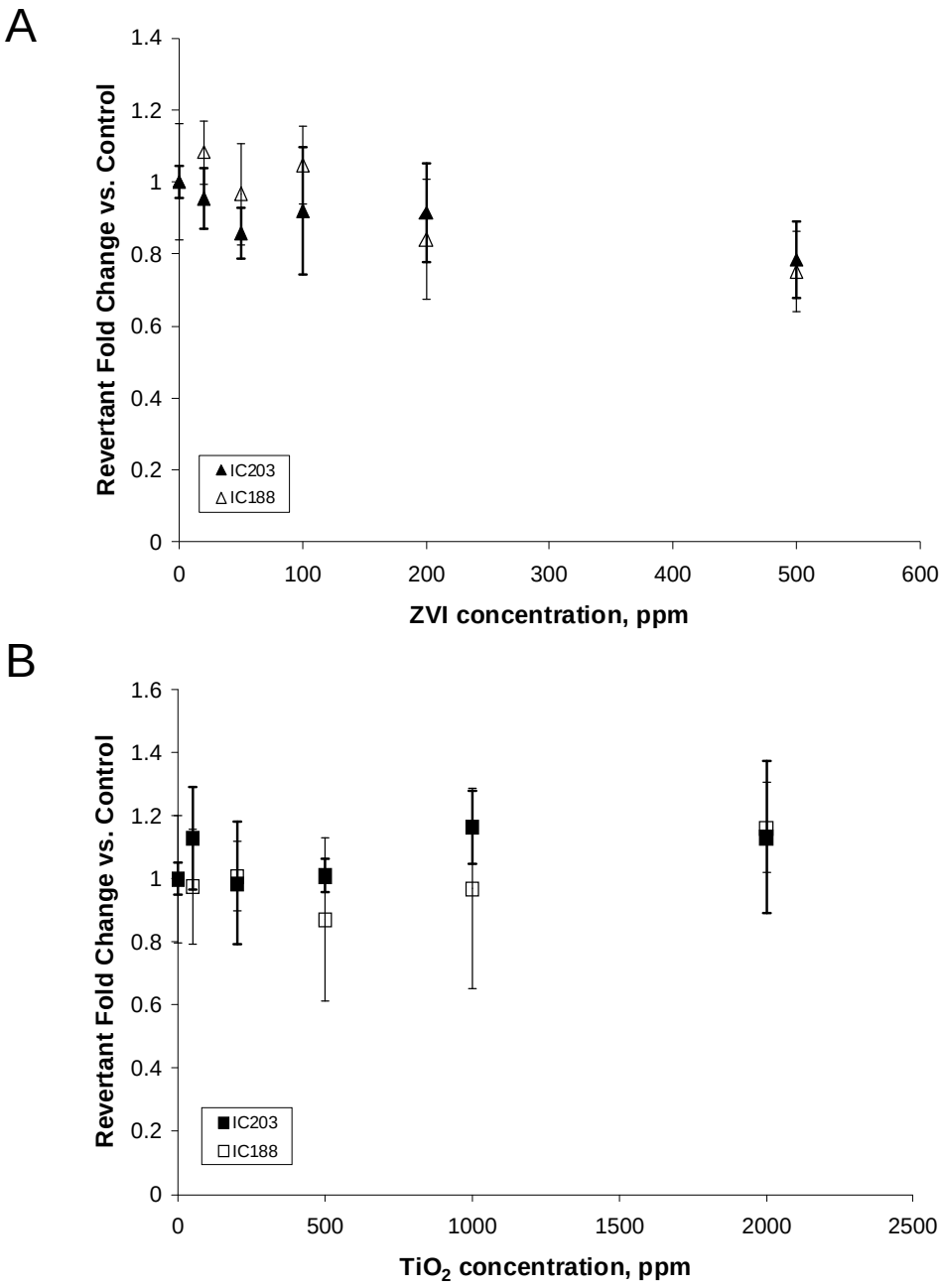

Figure 4.2. Effects on reversion of *E. coli* WP2 strain IC188 (open symbols, thin error bars) and its OxyR$^-$ derivative strain IC203 (closed symbols, thick error bars) after exposure to ZVI (A) or TiO_2 (B) for 1 h at 37°C. After subtracting counts of pre-existing mutants in the overnight culture, fold change was calculated as the number of revertants in treated cultures vs. controls. Values and error bars represent the mean and standard deviation of duplicate experiments, each consisting of duplicate plates.

Table 4.1. *E. coli* genes with the largest change (90th percentile) following 1-h exposure to 50 ppm ZVI relative to unexposed cells.

Gene Symbol	Description	Fold Change
Up-regulated genes		
yebN	Hypothetical protein yebN ; putative membrane protein, terpenoid synthase-like	62
yjdB	Putative transmembrane protein	26
ais	Ais protein ; protein induced by aluminum	23
yfbG	Putative formyltransferase	20
yfbF	Putative glycosyl transferase yfbF ; putative sugar transferase	16
yfbE	Hypothetical protein yfbE ; putative aminotransferase	16
yeiT	bifunctional: putative glutamate synthase (N-terminal); putative oxidoreductase (C-terminal)	14
metE	5-methyltetrahydropteroyltriglutamate-homocysteine methyltransferase	13
ftn	Ferritin 1 ; cytoplasmic ferritin (an iron storage protein)	12
yeiA	Hypothetical protein yeiA ; putative dihydropyrimidine dehydrogenase, FMN-linked	11
yfbH	Hypothetical protein yfbH ; hypothetical protein	8.0
recN	DNA repair protein recN ; protein used in recombination and DNA repair	7.9
yohL	Hypothetical protein yohL ; hypothetical protein	7.2
ykgE	Hypothetical protein ykgE ; putative dehydrogenase subunit	6.6
Down-regulated genes		
fhuF	ferric hydroxamate transport protein	-332
ycdN	pseudo	-270
entC	Isochorismate synthase entC ; isochorismate hydroxymutase 2, enterochelin biosynthesis	-153
nrdI	NrdI protein ; stimulates ribonucleotide reduction, flavoprotein	-118
nrdH	Glutaredoxin-like protein nrdH ; glutaredoxin-like protein; hydrogen donor	-117
bfd	Bacterioferritin-associated ferredoxin ; regulatory or redox component complexing with Bfr, in iron storage and mobility	-112
exbB	Biopolymer transport exbB protein ; uptake of enterobactin; tonB-dependent uptake of B colicins	-58
fecI	KpLE2 phage-like element; sigma 19 factor of RNA polymerase	-58
feoA	Ferrous iron transport protein A	-53
fes	Enterochelin esterase	-52
fhuA	Outer membrane pore protein, receptor for ferrichrome, colicin M, and phages T1, T5 and phi80	-49
sodA	Superoxide dismutase [Mn] ; superoxide dismutase, manganese	-46
fepB	Ferrienterobactin-binding periplasmic protein precursor ; ferric enterobactin (enterochelin) binding protein; periplasmic component	-44
entB	Isochorismatase ; 2,3-dihydro-2,3-dihydroxybenzoate synthetase, isochroismatase	-44
exbD	Biopolymer transport exbD protein ; uptake of enterobactin; tonB-dependent uptake of B colicins	-43
mntH	Manganese transport protein mntH ; high-affinity manganese transporter	-40

up-regulation of 11 genes and down-regulation of 201 genes relative to controls. Table 4.2 lists the top 5 up-regulated genes and the 90th percentile down-regulated genes for TiO_2. For

ZVI, up-regulated genes include transmembrane proteins (*yebN*, *yjdB*), iron sequestration (*ftn*), oxidoreductases and dehydrogenases (*yeiT*, *yeiA*, *ykgE*), transferases involved in evading cationic antimicrobial peptides (*yfbG*, *yfbF*) (*149*), and a DNA repair protein inducible by the SOS response (*recN*) (*150*). Most of the highly repressed genes listed in Table 4.1 are involved in iron uptake and transport, including several genes related to the

Table 4.2. *E. coli* genes with the largest change (90th percentile) following 1-h exposure to 200 ppm TiO_2 relative to unexposed cells.

Gene Symbol	Description	Fold Change
Up-regulated genes[a]		
yodA	Hypothetical protein yodA ; hypothetical protein	9.8
metE	5-methyltetrahydropteroyltriglutamate--homocysteine methyltransferase	7.2
ykgM	50S ribosomal protein L31 type B-1 ; putative ribosomal protein	7.1
ftn	Ferritin 1 ; cytoplasmic ferritin (an iron storage protein)	6.0
thrB	Homoserine kinase	3.7
Down-regulated genes		
fes	Enterochelin esterase	-20
nrdI	NrdI protein ; stimulates ribonucleotide reduction, flavoprotein	-17
nrdH	Glutaredoxin-like protein nrdH ; glutaredoxin-like protein; hydrogen donor	-15
ycdF	unknown CDS	-14
fecI	KpLE2 phage-like element; sigma 19 factor of RNA polymerase	-14
ycdN	pseudo	-13
mntH	Manganese transport protein mntH ; high-affinity manganese transporter.	-12
yciG	hypothetical protein	-11
ygaM	Hypothetical protein ygaM ; hypothetical protein	-10
fhuF	ferric hydroxamate transport protein	-10
fepB	Ferrienterobactin-binding periplasmic protein precursor ; ferric enterobactin (enterochelin) binding protein; periplasmic component	-9.5
sufA	SufA protein ; hypothetical protein	-8.9
ybgS	Hypothetical protein ybgS precursor ; putative homeobox protein	-8.2
yciF	Protein yciF ; putative structural proteins	-8.1
bfd	Bacterioferritin-associated ferredoxin ; regulatory or redox component complexing with Bfr, in iron storage and mobility	-8.1
ecnB	Putative toxin of osmotically regulated toxin-antitoxin system associated with programmed cell death ; entericidin B	-7.6
yodD	Hypothetical protein yodD ; unknown CDS	-7.5
yiaG	Hypothetical protein yiaG ; putative transcriptional regulator	-7.1
aidB	AidB protein ; putative acyl coenzyme A dehydrogenase	-7.0
exbB	Biopolymer transport exbB protein ; uptake of enterobactin; tonB-dependent uptake of B colicins	-7.0

[a] The top 5 of 11 total up-regulated genes are listed.

siderophore enterobactin (*fepB*, *exbB*, *exbD*, *entC*, *entB*, *fes*). Two of the down-regulated genes are relevant to oxidative stress response (*sodA*, *nrdH*). Genes up-regulated by TiO_2 exposure are involved in cell maintenance functions, except for the iron storage gene *ftn*. Down-regulated genes for TiO_2 include metal uptake (*mntH*, *fec1*, *fhuF*, *bfd*), siderophores (*fes*, *fepB*, *exbB*), osmotic stress response (*yciF*, *ecnB*), and oxidative stress response (*nrdH*).

The top functional clusters associated with up- and down-regulated genes following ZVI exposure are presented in Figures 4.3-A and 4.3-B, respectively. The enrichment score is the negative log of the Fisher exact test p-value, and is thus a measure of the strength of the association. Oxidative phosphorylation and electron transport were the most highly associated pathways/keywords for up-regulated genes, with an additional cluster of cell maintenance and biosynthesis pathways (Figure 4.3-A). Top clusters for down-regulated genes were iron transport and iron-deprivation-induced iron-sulfur assemblies (Figure 4.3-B). Other down-regulated clusters for ZVI were superoxide dismutase, ribonucleotide reductases, and glucose dehydrogenase. Clusters associated with TiO_2 exposure are shown for up-regulated (Figure 4.4-A) and down-regulated genes (Figure 4.4-B). The four up-regulated clusters with enrichment scores greater than 1.3 (equivalent to $p < 0.05$) were related to biosynthesis and cell maintenance functions (Figure 4.4-A). Down-regulated clusters for TiO_2 were glutathione-S-transferase, osmotic stress response, iron-deprivation-induced iron-sulfur assemblies, metal ion transport, and superoxide dismutase (Figure 4.4-B).

4.3.4 Respirometry. OUR measurements on *E. coli* K-12 cultures exposed to ZVI (50 ppm, 1 h), or TiO_2 (200 ppm, 1 h) and on control cultures are summarized in Table 4.3. Cell-free oxygen consumption by ZVI and TiO_2 was negligible compared to the OUR of overnight

A

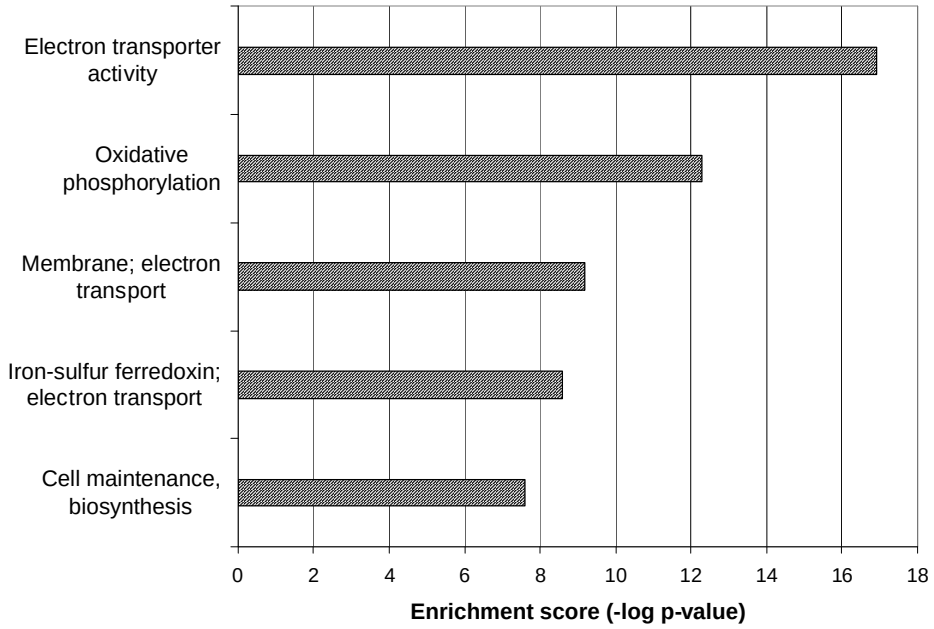

B

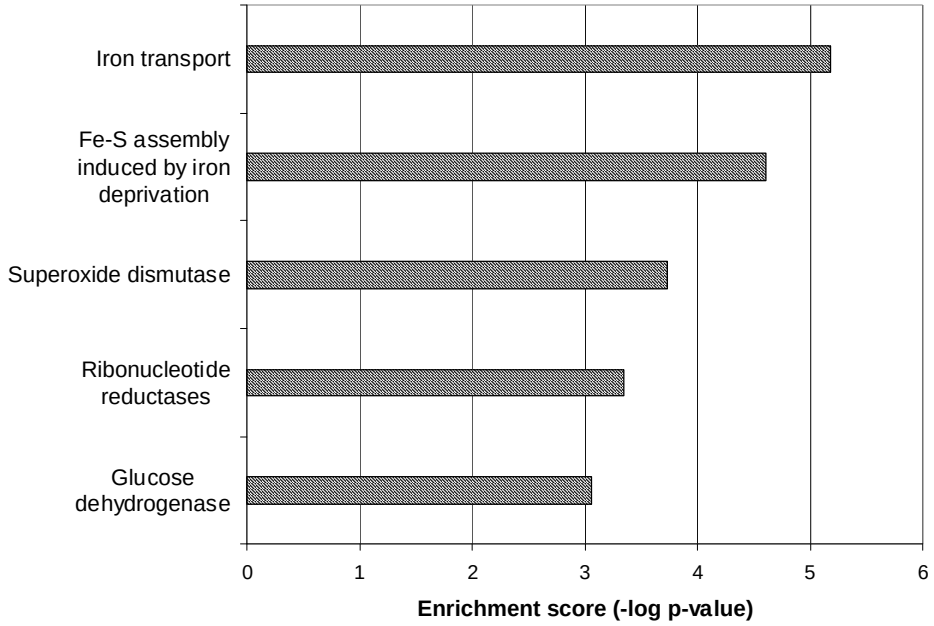

Figure 4.3. Functional analysis of pathways and keywords associated with induced (A) and repressed (B) genes in *E. coli* K-12 after 1 h exposure to ZVI (50 ppm) relative to control cultures. The enrichment score represents the likelihood that more differentially expressed genes are represented in a pathway than would be expected by random selection of genes from the entire genome.

A

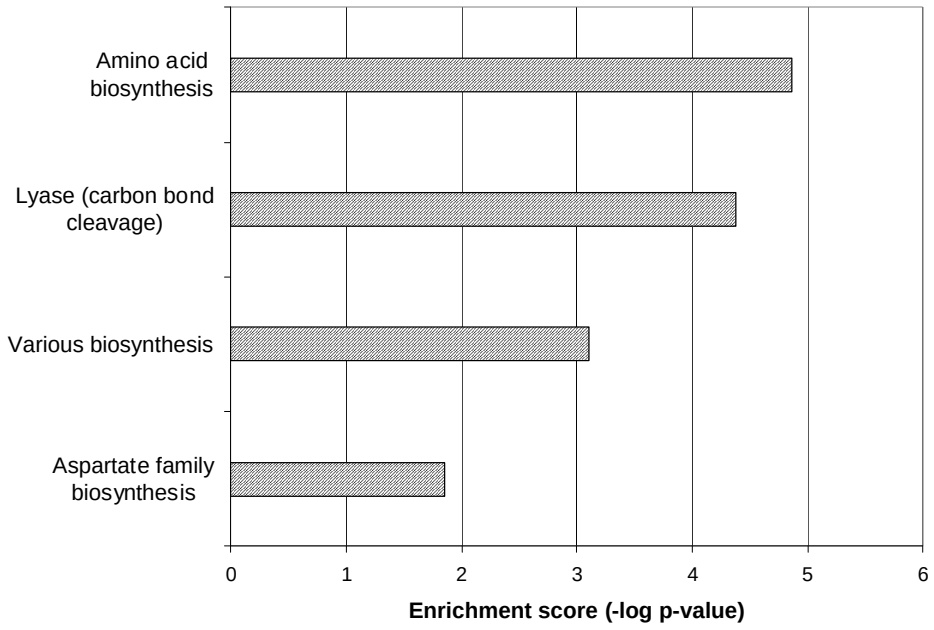

B

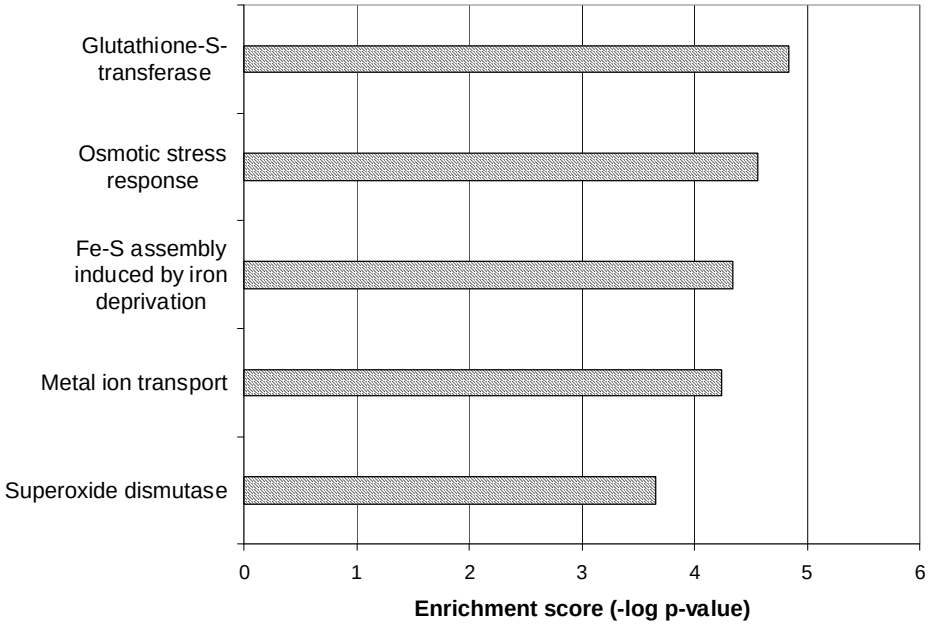

Figure 4.4. Functional analysis of pathways and keywords associated with induced (A) and repressed (B) genes in *E. coli* K-12 after 1 h exposure to TiO_2 (200 ppm) relative to control cultures.

Table 4.3. Oxygen uptake rate (mg L^{-1} h^{-1}) by *E. coli* K-12 in the presence of ZVI and TiO_2. Values are mean ± standard deviation (SD) of triplicate measurements.

Condition	**PBS Control**	**ZVI (50 ppm)**	**TiO_2 (200 ppm)**
No cells	--	1.6 ± 0.4	0.8 ± 1.4
overnight culture	18.5 ± 2.9	41.3 ± 7.3[a]	23.9 ± 2.7
+ 2 g/L glucose, total	25.0 ± 3.1	43.1 ± 2.7[a]	29.6 ± 3.8
+ 2 g/L glucose, net	6.5 ± 3.8	1.8 ± 5.2	5.7 ± 2.4

[a] Significantly different from PBS control ($p < 0.05$).

cultures. The OUR for cells exposed to ZVI was significantly higher than the rate for the control culture ($p < 0.05$). The rates for TiO_2-exposed cells and the net OUR after glucose addition for both treatments were not significantly different from the control OUR.

4.3.5 Electron Microscopy. SEM images of control and exposed cultures are presented in Figures 4.5 and 4.6. Aggregates of nanoparticles are visible among cells exposed to TiO_2 (Figure 4.5-B) and ZVI (Figure 4.5-C) that are not visible in the control (Figure 4.5-A). X-ray elemental analysis verified that the observed aggregates contained titanium and iron, respectively. Ultrastructural analysis at higher magnification showed smooth outer membranes for unexposed cultures (Figure 4.6-A) and for TiO_2-exposed cells, even those in close proximity to aggregates (Figure 4.6-B). ZVI-exposed cultures contained many cells with rough bumps on the surface in addition to smooth cells (Figures 4.6-C, 4.6-D).

Figure 4.7 presents TEM images of control (A) and exposed (B-D) cultures. TiO_2-exposed cells were not associated with TiO_2 aggregates, either externally or internally

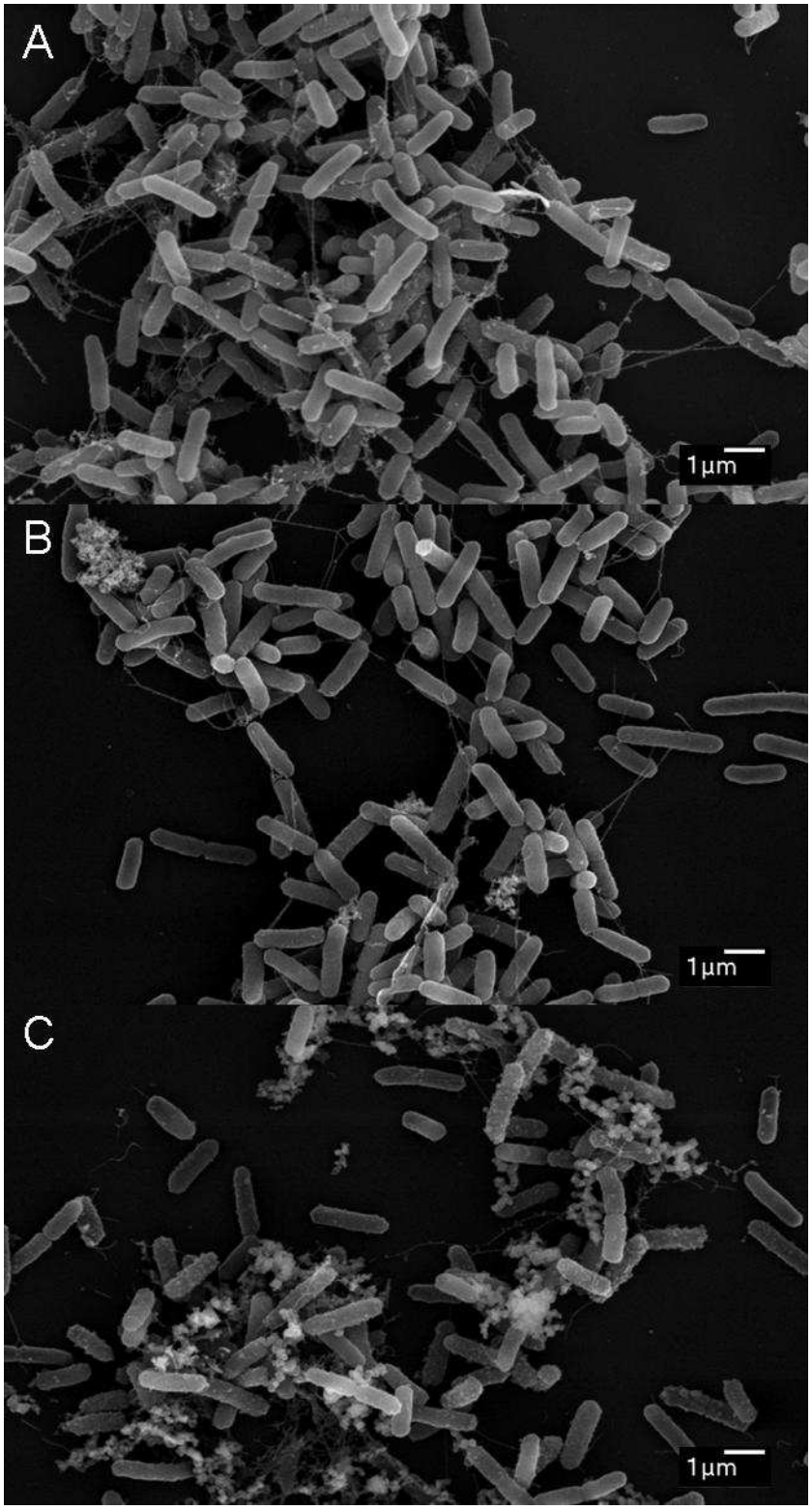

Figure 4.5. Scanning electron micrographs of *E. coli* K-12 for unexposed cultures (A) and cultures exposed for 1 h to 200 ppm TiO_2 (B) or 50 ppm ZVI (C).

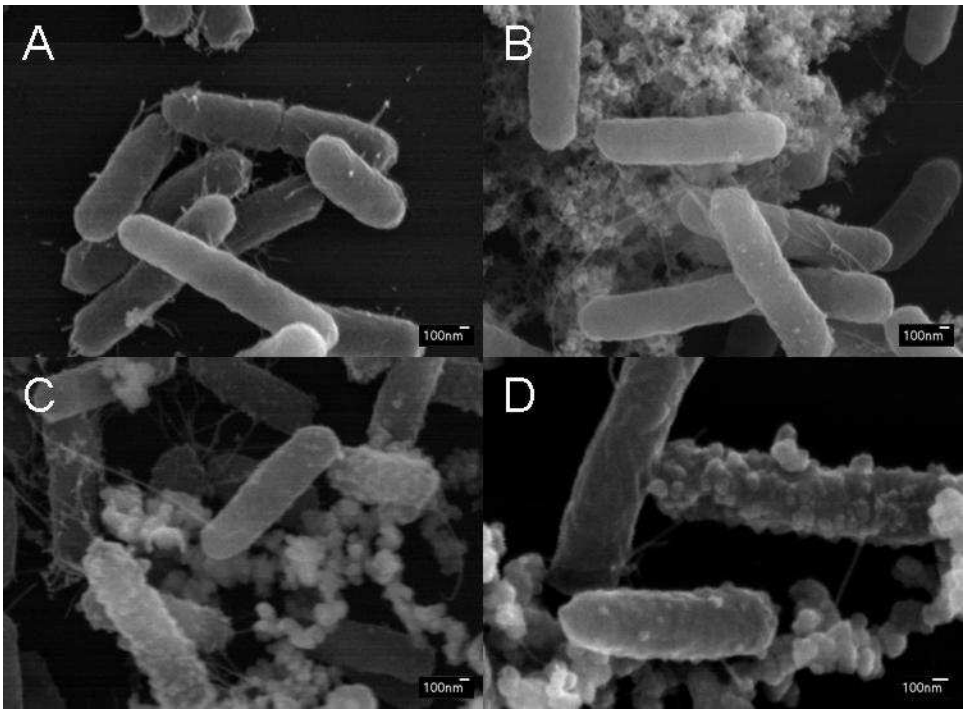

Figure 4.6. Scanning electron micrographs of *E. coli* K-12 for unexposed cultures (A) and cultures exposed for 1 h to 200 ppm TiO_2 (B) or 50 ppm ZVI (C, D).

(Figure 4.7-B). The dark-staining aggregates appeared to be composed of clusters of individual TiO_2 nanoparticles. ZVI nanoparticles were closely associated with the cell envelope (Figure 4.7-C, 4.7-D). Some particles were associated with the outer membrane, while others penetrated into the periplasmic space and appeared to associate with the cytoplasmic membrane; none of the particles appeared to be internalized. Membrane-associated ZVI appeared to be in small clusters (Figure 4.7-C) or individual particles (Figures 4.7-C, 4.7-D). Unassociated ZVI aggregates were also visible (arrow, Figure 4.7-C). The localization of ZVI nanoparticles at the cell surface is consistent with the bumps observed with SEM, although localized elemental analysis could not positively identify iron in the SEM images due to low signal/noise ratio. The bright spots and rough cell walls observed in

the TEM images are artifacts of incomplete dehydration during sample preparation.

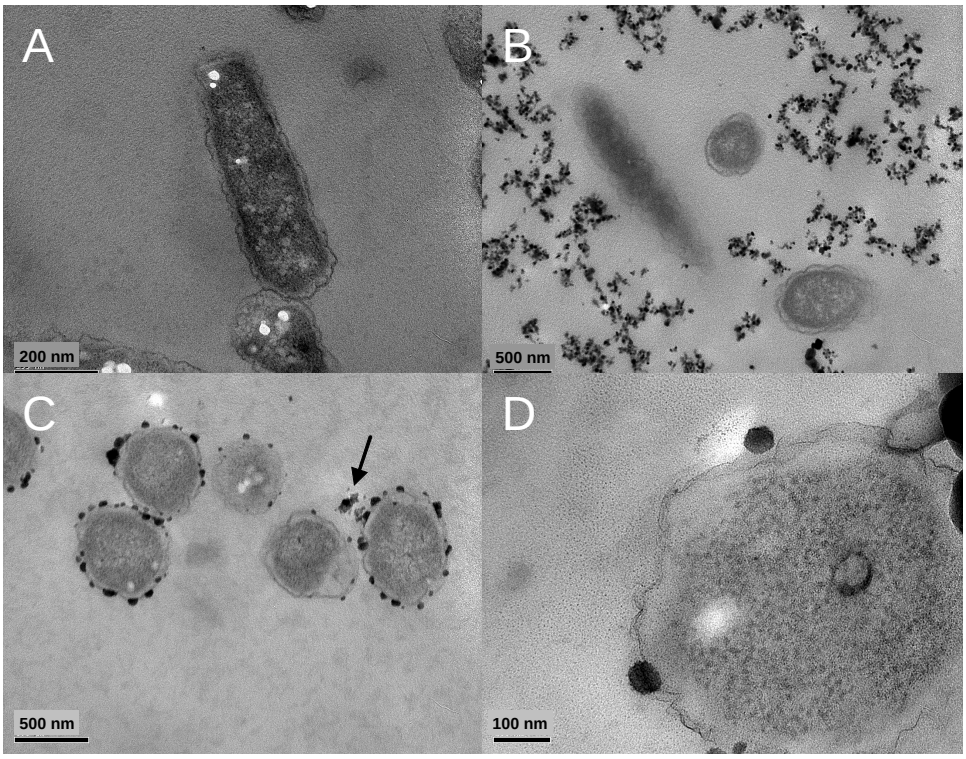

Figure 4.7. Transmission electron micrographs of *E. coli* K-12 for unexposed cultures (A) and cultures exposed for 1 h to 200 ppm TiO_2 (B) or 50 ppm ZVI (C, D).

4.3.6 Physicochemistry. Particle size measurements made on freshly prepared and shaken/incubated ZVI (50 ppm) and TiO_2 (200 ppm) suspensions are presented in Table 4.4. The peak of the particle size distribution was greater than 1 μm for both ZVI and TiO_2 for measurements made immediately after preparation of the suspensions, indicating rapid aggregation of the primary particles. After 1 h shaking at 37°C, the size of ZVI particles remaining in suspension was approximately 260 nm. Sedimentation of TiO_2 aggregates reduced the suspended particle count below the detection limit of the instrument after 1 h

shaking at 37°C. Mean particle size in suspensions containing bacteria was approximately 1100-1200 nm for bacteria alone or with TiO_2, and 1600 nm for bacteria with ZVI.

Table 4.4. Size and zeta potential of ZVI, TiO_2 and cell suspensions measured at 37°C. Values are mean ± SD of triplicate measurements.

Exposure	**Condition**	**Size, nm**	**Zeta Potential, mV**
ZVI 50 ppm	t=0	1220 ± 50	-18.6 ± 2.2
	Supernatant after 1 h incubation/shaking (no cells)	257 ± 26	-21.9 ± 0.8
	Supernatant after 1 h incubation/shaking with *E. coli* K-12	1610 ± 160	-13.2 ± 0.8
TiO_2 200 ppm	t=0	2420 ± 190	-15.9 ± 1.1
	Supernatant after 1 h incubation/shaking (no cells)	ND[a]	-21.5 ± 2.1
	Supernatant after 1 h incubation/shaking with *E. coli* K-12	1110 ± 290	-13.1 ± 2.5
PBS	Supernatant after 1 h incubation/shaking with *E. coli* K-12	1160 ± 40	-13.6 ± 0.5

[a] ND, not determined (particle count too low for accurate measurement).

Zeta potential measurements were negative for all suspensions tested (Table 4.4). The initial value for ZVI (50 ppm) without cells was -18.6 mV and decreased to -21.9 mV after 1 h shaking at 37°C. TiO_2 had an initial value of -15.9 mV, which decreased to -21.5 mV after 1 h shaking at 37°C. Suspensions containing bacteria all had zeta potential values of approximately -13 mV.

4.4 Discussion

Results of the viability experiments indicate that ZVI is toxic to *E. coli* under laboratory conditions after 1 h at concentrations above 100 ppm, while TiO_2 does not significantly

reduce viability after 1 h incubation in the dark at concentrations up to 2000 ppm. Previous reports of nanoscale ZVI toxicity in bacteria are not available. Antimicrobial activity of photo-activated TiO_2 has been well studied (*151*), but previous studies investigating TiO_2 toxicity in the absence of light found only moderate growth inhibition of *E. coli* at a concentration of 2000 ppm (*50*), and 95% survival after overnight incubation of TiO_2 with *Staphylococcus aureus* and *Bacillus subtilis* (*58*). Such limited toxicity in the absence of light is consistent with the generally accepted mode of action of TiO_2 toxicity via photo-catalyzed generation of ROS.

Experiments with mutant *E. coli* strains did not provide evidence that either ZVI or TiO_2 increases the rate of mutagenesis in a strain (IC203) susceptible to oxidative stress (OS) relative to its parent strain proficient in OS response (IC188). No significant increase in reversion rate was observed in either strain after exposure to ZVI or TiO_2, indicating that the observed toxicity of ZVI may not be due to generation of ROS and associated DNA damage and repair. This is also consistent with a study which found negative results for nanosized TiO_2 in the Ames bacterial reverse mutation test (*152*). Gene expression results in strain K-12 also provide evidence that cells are not provoked to an OS response, as indicated by down-regulation of superoxide dismutase and other OS genes after both ZVI and TiO_2 exposure.

Functional analysis of the gene expression profile of *E. coli* K-12 indicates that oxidative phosphorylation and electron transport are major pathways up-regulated by ZVI exposure. The oxidative side of the electron transport chain, particularly Complex I, is induced more strongly than ATP synthase on the phosphorylation side. All NADH dehydrogenase I chain A-N genes were up-regulated by ZVI exposure (1.7- to 5.0-fold

increase), as was the NADH dehydrogenase transcriptional regulator *lrhA*. Further evidence for increased cycling through the electron transport chain was provided by the increase in oxygen uptake rate observed after ZVI exposure (Table 4.3). This effect is similar to that observed with uncouplers of oxidative phosphorylation, which disrupt the proton motive force (PMF) across the inner membrane and accelerate the rate of oxidation without being hindered by the rate of proton translocation through ATP synthase (*153*). A study of the response of *E. coli* to the uncoupler 2,4-dinitrophenol found that 21 identified proteins were induced (*154*); seven of these were also up-regulated in the present study after ZVI exposure, but none were induced by TiO_2 exposure. Membrane damage has been observed after bacterial exposure to nanoparticles (*49, 59*) and could be responsible for leakage of protons. The ZVI observed at the cytoplasmic membrane in the TEM images would be expected to increase membrane permeability and facilitate proton transport. ZVI at the outer membrane could also be acting electrochemically to diminish the PMF by consumption of H^+ during coupled redox reactions. Disruption of the cytoplasmic membrane would presumably have a greater effect on PMF than proton consumption in the periplasmic space, but neither mechanism can be ruled out based on the current data. Such interference with energy metabolism could help explain the observed toxicity of ZVI. It also appears to be consistent with depolarization of the mitochondrial membrane observed in BV2 microglia exposed to ZVI (B. Veronesi, T.C. Long, T. Phenrat, N. Saleh, G.V. Lowry, data not shown), which could indicate a common mode of action. Microscopic examination of exposed microglia may provide additional evidence in this regard. The observed strong down-regulation of iron uptake and transport genes and genes encoding iron siderophores after ZVI exposure would be expected in an iron-rich environment.

Exposure to TiO_2 did not produce either up-regulation of oxidative phosphorylation genes or an increase in oxygen uptake. TiO_2 also did not induce toxic or stress response pathways, consistent with its lack of toxicity. Down-regulation of stress response pathways after TiO_2 exposure was also consistent with its minimal effect on viability.

Electron microscopy showed individual particles and small clusters of ZVI closely associated with cells, localized at the cell surface. This is consistent with a previous report of added iron oxide adsorbing to the surface of a Gram-negative iron-reducing bacterium (*155*), considering that ZVI particles accumulate an iron oxide shell in aerobic environments (*134*). Since no internalization of ZVI was observed, the effects of ZVI exposure on viability, gene expression, and oxygen uptake appear to have been mediated via membrane-associated processes. Close association of ZVI with the membrane could increase permeability and disrupt species and charge balances, such as electron transport and the proton-motive force necessary for ATP generation. Several studies have documented disruption of bacterial membranes following exposure to metal and metal oxide nanoparticles, including MgO, ZnO, CeO_2, and Ag (*33, 49, 54, 57*). Different shapes and lattice plane characteristics of silver nanoparticles have also been found to differentially affect *E. coli* toxicity and membrane integrity (*51*). No particle-cell association was observed for TiO_2-exposed cultures, even though TiO_2 aggregates were seen in the vicinity. Taken together, the combined results indicate that ZVI and TiO_2 produce different effects on bacteria.

Characterization of the physicochemical properties of nanoparticle suspensions is an important aspect of nanoparticle toxicity research (*17*). These properties will influence particle interactions with biological systems and should be measured under conditions paralleling the biological exposures. Measurements in the present study found that both ZVI

and TiO_2 aggregated rapidly in PBS buffer to form >1000 nm aggregates, comparable to the size of bacterial cells, and sedimentation of larger aggregates occurred during incubation despite shaking of the cultures. ZVI aggregates remaining in suspension after 1 h exposure were closer to the the 100 nm nominal upper range for nanoparticles. Electron microscopy provided evidence that both ZVI and TiO_2 aggregates were of a fractal nature and maintained nanoscale structural features, as has been described previously (*7*). In combined ZVI-bacterial suspensions, particle size increased relative to bacteria alone, consistent with both association of the ZVI particles with the cells and with increased hydrodynamic diameter due to observed cell surface alterations. Sedimentation of TiO_2 aggregates was more pronounced than for ZVI and prevented measurement of the particles remaining in suspension, although turbidity was visible in the cell-free tubes. Zeta potential measurements were negative for all suspensions and were of similar magnitude for ZVI and TiO_2. In suspensions containing bacteria, the magnitude of the negative charge was reduced, and associations between cells and similarly charged particles did not significantly affect surface charge.

The demonstrated utility of nanoscale ZVI in environmental applications for cleanup of contaminated sites may need to be balanced against the potential for negative effects on soil microflora. In particular, in situ remediation strategies should consider whether viability loss due to ZVI may limit the rate and extent of biodegradation in the subsurface. The apparent lack of TiO_2 toxicity in the absence of photoactivation could help alleviate concerns about ecotoxicity following its environmental release, although TiO_2 in surface waters or routes leading to human exposure may pose a risk. Long-term effects of ZVI may be mitigated by environmental formation of iron oxides, which appear to be less toxic in vitro to mammalian cells (B. Veronesi, T.C. Long, T. Phenrat, N. Saleh, G.V. Lowry, data not

shown). Subsurface sites remediated with large deposits of ZVI under anaerobic conditions may remain active (and bioactive) for some time, however. Anaerobic respiration and electron transport in organisms that use alternate terminal electron acceptors (such as nitrate or sulfate) could still be negatively impacted. In anaerobic microbes lacking complete electron transport pathways, the negative effect of ZVI on energy metabolism may be reduced because substrate-level phosphorylation does not depend on membrane-associated electron transport for ATP synthesis. However, the extent to which ZVI nanoparticles might disrupt other trans-membrane processes in anaerobic microbes has not been evaluated. Although the potential toxicity of ZVI to bacteria or archaea must still be evaluated under field conditions, results from this work may be useful in continued development of nanoparticle-based technologies for environmental treatment and remediation.

5. SUMMARY AND CONCLUSIONS

Rapid advances in the development of nanotechnology must be accompanied by research into the potential toxicity of nanomaterials. The research described here contributes to the growing body of knowledge on the potential health and environmental effects of nanotechnology by investigating the response of bacteria and mammalian brain cells to ZVI and TiO_2, two nanoparticles in widespread use for treatment and remediation applications. TiO_2 aggregated rapidly in biological media and was internalized by microglia, possibly through phagocytosis. TiO_2 also stimulated initial activiation of microglia to release ROS through the oxidative burst, with viability loss and entry into apoptotic pathways after extended exposure. Gene expression profiles in microglia after sublethal exposure to TiO_2 indicated up-regulation of signaling pathways associated with inflammation and apoptosis, with down-regulation of oxidative phosphorylation, energy production and oxidative stress. TiO_2 was not directly toxic to immortalized oxidative stress-susceptible dopaminergic neurons, but in primary cultures containing microglia, neuronal populations were reduced following TiO_2 exposure. This is consistent with current hypotheses on neurodegeneration which involve microglial activation as an important component of neuronal damage in well-known diseases (*48*). In *E. coli*, TiO_2 did not cause loss of viability, increased respiration, or other indications of toxicity, consistent with an indirect mode of action (microglial activation) for its toxicity in mammalian cells.

ZVI caused viability loss in bacteria after 1 h at concentrations of 100 ppm and above. *E. coli* responded to sublethal ZVI exposure with induction of electron transport genes and increased oxygen uptake rate, consistent with increased activity of the electron transport chain. However, there was no evidence that ZVI induced cellular responses indicative of oxidative stress. The observed down-regulation of OS response genes in *E. coli* is consistent with the role of ZVI as a reducing agent.

Ultrastructural analysis showed ZVI nanoparticles localized on the bacterial cell surface, which could interfere with maintenance of the proton-motive force necessary for ATP generation through oxidative phosphorylation. Other studies have found similar association of metal and metal oxide nanoparticles with bacterial membranes leading to cytotoxicity (*33, 49-54*). For example, analysis of the effect of crystal structure on toxicity has implicated the {1,1,1} face of silver nanoparticles as particularly reactive (*156*) and potentially associated with toxicity (*51, 53*). The ongoing formation of iron oxides and hydroxides during ZVI oxidation makes crystallographic analysis difficult, because amorphous (hydr)oxides are formed initially (*157*), but the magnetite shell around ZVI particles is of the cubic crystal system and could present a {1,1,1} face. It has also been suggested in studies on the toxicity of silver nanoparticles that internalized silver ions could inhibit respiratory enzymes, in turn causing increased generation of ROS and oxidative stress-related cytotoxicity (*54*), but no evidence was provided by the authors to support this mechanism. Although internalization would not be required for the observed ability of ZVI to interfere with membrane-bound electron transport, as noted above there was no evidence that ZVI led to oxidative stress in *E. coli* in the current study.

Comparison of toxicity results for ZVI and TiO_2 from this study may reveal themes that have implications for future nanoparticle toxicity research. One aspect differing among the two particles is redox activity, which is inherent for ZVI but requires photoactivation for TiO_2. Although overall oxidation of ZVI was low during the exposure period, it may have created a localized reducing environment, promoting redox reactions that affected components of the cell envelope. This is consistent with studies which found increased toxicity for zero-valent metals compared to their oxides and for metal-doped silica compared to pure silica nanoparticles with similar physical characteristics (*158*). With the focus on oxidative stress as a mechanism of particle toxicity, similar consideration should be given to the catalytic and redox activity of nanoparticles, as is done for ambient ultrafine particulate matter (*159*). The extent to which nanoparticles are able to catalyze and participate in redox reactions appears to be an important characteristic affecting toxicity.

Similarly, surface area has been proposed as a defining property for toxic effects, but surface reactivity may be more important (*160*). ZVI nanoparticles have a surface composed of iron oxides undergoing further oxidation, giving them much higher surface activity than TiO_2, which is stable in the absence of light. Results of the current work do not support a positive association between surface area and toxicity, with Degussa P25 TiO_2 having more than double the specific surface area of ZVI. However, TiO_2 showed faster and more extensive agglomeration than ZVI, possibly mitigating some of the surface area differential. For particles with low inherent toxicity, surface area may become a more important parameter (*161*). Other studies have implicated surface area as the parameter that determines the level of proinflammatory responses in otherwise low-toxicity particles (*162*). This indicates that surface area may be a valid driver of effects for comparison of nanoscale and

bulk scale versions of the same material, but that other factors (such as surface reactivity) are more important than surface area when comparing different materials. Other evidence that surface properties affect behavior is provided by comparison of medical imaging nanoparticles, which have surfaces similar to biological molecules and tend not to be toxic, with combustion-derived (e.g. fullerenes) and metal oxide nanoparticles, which are toxic (*163-165*). Reduction in surface reactivity is also known to reduce ROS generation and toxic effects in vitro and in vivo (*161, 166*). Primary particle size and surface charge (zeta potential) were similar for ZVI and TiO_2, indicating that size and charge alone do not explain the observed differential toxicity. Overall, results from this study indicate that nanoparticles of different composition and other characteristics provoke different responses in cell cultures and may act via different modes of action.

Further research could help identify the specific characteristics of nanoparticles that drive biological effects as well as provide insight into their mode of action. It would be useful to compare the toxicity of oxidizable metal nanoparticles (e.g., ZVI) with that of their more stable oxides (e.g., magnetite) to evaluate whether participation in redox chemistry increases toxicity. Comparison of metals or metal oxides with different crystal structures or presenting different crystal faces could support the observation of increased toxicity for silver nanoparticles with {1,1,1} faces (*51*). To distinguish between the effect of surface area and surface reactivity, the relative effects in these bacterial and mammalian cell systems could be compared for metalloid nanoparticles with similar surface area, but different surface reactivity as observed for carbon nanotubes vs. carbon black (*167*). The combined results of such studies could be used to develop a screening test for risk assessment of newly developed nanomaterials based on their physical, chemical, and crystallographic properties.

Mechanistic studies are needed to test for disruption of the PMF in bacteria during ZVI exposure, such as with a membrane-potential-dependent stain (*54*). Inspection of the bacterial TEM images indicated that some cells have more ZVI on the surface than others. Image analysis may be used to quantify the fractional coverage of individual cells, and the distribution of coverage values could be linked to viability results. Studies should also investigate reasons for the association of ZVI, but not TiO_2, with the cell envelope. If positively charged ferrous or ferric ions are present on the surface of ZVI particles undergoing oxidation, electrostatic attraction to negative charges on the bacterial envelope would contribute to the observed association, whereas uncharged TiO_2 would not be affected. Comparison of ZVI with iron oxide or surface-modified ZVI nanoparticles could help understand this phenomenon. Additionally, extension of the toxicity testing paradigm to ecologically relevant species (e.g. daphnia) and animal models will be an important component of risk assessment for these nanomaterials and could yield mechanistic insights.

Field and pilot studies are also needed to evaluate the biological effects of ZVI and TiO_2 remediation strategies under environmental conditions. Toxicity and biological response endpoints can be included along with chemical analyses measuring treatment efficiency. For example, in pilot field studies testing the use of ZVI for treatment of subsurface chlorinated solvent plumes, community analysis of the microbial population could be conducted prior to and following ZVI injection, or upstream and downstream of the plume, to determine if ZVI is altering the community composition by selective toxicity or enrichment (e.g., of iron-reducing bacteria) (*168*). A study on treatment of a munitions plume with an immobilized granular microscale ZVI barrier found increases in total bacterial counts and detected iron-reducing, sulfate reducing, and putative methanogenic

microorganisms in the barrier, although the effect on treatment efficiency was not evaluated (*169*). Groundwater samples above and below the plume could also be tested for residual ZVI and its oxidation products, along with analysis of bacterial toxicity, to evaluate overall effects on groundwater quality. Such testing would also be useful for applications involving surface-modified ZVI.

The initial implications for human and ecosystem health of the early cell culture studies conducted in this project are that TiO_2 may exhibit toxicity if it enters the body and activates immune responses. Environmental exposures may be of lesser importantance unless photoactivation is a possibility, such as might occur in surface waters. The tendency of TiO_2 to rapidly aggregate and settle would tend to remove it from suspension and move it to the sediment phase, where it presumably would be less active. ZVI appears to be directly toxic to mammalian cells without requiring microglial activation. Aging/oxidation and surface modification mitigate this toxicity, indicating that environmental weathering may reduce ZVI toxicity over time, and next-generation SM ZVI may have lower overall toxicity. Toxicity testing of emerging nanomaterials such as doped TiO_2 and newly developed surface-modifications will also be important for the future.

These studies may also have implications for applications of ZVI and TiO_2 in treatment and remediation. The use of TiO_2 in drinking water treatment should continue to be carefully monitored for human exposure due to its potential for microglia-mediated health effects. Again, release of TiO_2 into the environment may be of less concern due to its tendency to form aggregates which settle out away from light. Technologies that utilize immobilized TiO_2 are also promising (*67, 170, 171*). For ZVI applications, introduction of fresh ZVI into the environment should be handled with caution, although long-term health

and environmental effects would be mitigated by formation of less-toxic iron oxides. Rates of oxide formation may be low, since anoxic subsurface conditions would tend to maintain the activity and toxicity of large deposits of ZVI for some time. Field and pilot-scale evaluations of the ecotoxicity of ZVI and TiO_2 as described above would help address uncertainties and should be a component of research into the development of improved nanoparticle technologies for environmental remediation.

For TiO_2, both slurry-phase and fixed-bed or membrane-bound applications could benefit from effluent toxicity testing to determine if persistent residual compounds are formed during photochemical oxidation that may be toxic to bacteria or other species. Particle size analysis should also be done to determine the content of nanosize TiO_2 remaining in suspension; presumably most of the TiO_2 will be removed by agglomeration and sedimentation for reuse in slurry applications. Toxicity of this floc under simulated sunlight should also be investigated. Another possibility for fixed-bed and membrane-bound applications is to seed the influent with an indicator species, such as *E. coli*, then measure breakthrough and viability of the bacteria in the effluent compared to a control column containing no TiO_2. Such research would be an important part of the evaluation and risk assessment of these applications.

REFERENCES

1. Li, X. Q.; Elliott, D. W.; Zhang, W. X. Zero-valent iron nanoparticles for abatement of environmental pollutants: Materials and engineering aspects. *Crit. Rev. Solid State Mat. Sci.* **2006**, *31*, 111-122.

2. Kanel, S. R.; Greneche, J. M.; Choi, H. Arsenic(V) removal from groundwater using nano scale zero-valent iron as a colloidal reactive barrier material. *Environ. Sci. Technol.* **2006**, *40*, 2045-2050.

3. Cao, H. S.; Zhang, W. X. Stabilization of chromium ore processing residue (COPR) with nanoscale iron particles. *J. Hazard. Mater.* **2006**, *132*, 213-219.

4. Lowry, G. V.; Johnson, K. M. Congener-specific dechlorination of dissolved PCBs by microscale and nanoscale zerovalent iron in a water/methanol solution. *Environ. Sci. Technol.* **2004**, *38*, 5208-5216.

5. Schaefer, C. E.; Fuller, M. E.; Condee, C. W.; Lowey, J. M.; Hatzinger, P. B. Comparison of biotic and abiotic treatment approaches for co-mingled perchlorate, nitrate, and nitramine explosives in groundwater. *J. Contam. Hydrol.* **2007**, *89*, 231-250.

6. Saleh, N.; Sirk, K.; Liu, Y.; Phenrat, T.; Dufour, B.; Matyjaszewski, K.; Tilton, R. D.; Lowry, G. V. Surface modifications enhance nanoiron transport and NAPL targeting in saturated porous media. *Environ. Eng. Sci.* **2007**, *24*, 45-57.

7. Phenrat, T.; Saleh, N.; Sirk, K.; Tilton, R. D.; Lowry, G. V. Aggregation and sedimentation of aqueous nanoscale zerovalent iron dispersions. *Environ. Sci. Technol.* **2007**, *41*, 284-290.

8. Saleh, N.; Phenrat, T.; Sirk, K.; Dufour, B.; Ok, J.; Sarbu, T.; Matyjaszewski, K.; Tilton, R. D.; Lowry, G. V. Adsorbed triblock copolymers deliver reactive iron nanoparticles to the oil/water interface. *Nano. Lett.* **2005**, *5*, 2489-2494.

9. Quinn, J.; Geiger, C.; Clausen, C.; Brooks, K.; Coon, C.; O'Hara, S.; Krug, T.; Major, D.; Yoon, W. S.; Gavaskar, A.; Holdsworth, T. Field demonstration of DNAPL dehalogenation using emulsified zero-valent iron. *Environ. Sci. Technol.* **2005**, *39*, 1309-1318.

10. Ferguson, M. A.; Hering, J. G. TiO_2-photocatalyzed As(III) oxidation in a fixed-bed, flow-through reactor. *Environ. Sci. Technol.* **2006**, *40,* 4261-4267.

11. Daneshvar, N.; Salari, D.; Niaei, A.; Khataee, A. R. Photocatalytic degradation of the herbicide erioglaucine in the presence of nanosized titanium dioxide: Comparison and modeling of reaction kinetics. *J. Environ. Sci. Health B.* **2006**, *41,* 1273-1290.

12. Esterkin, C. R.; Negro, A. C.; Alfano, O. M.; Cassano, A. E. Air pollution remediation in a fixed bed photocatalytic reactor coated with TiO_2. *AIChE J.* **2005**, *51,* 2298-2310.

13. Higarashi, M. M.; Jardim, W. F. Remediation of pesticide contaminated soil using TiO_2 mediated by solar light. *Catal Today*. **2002**, *76,* 201-207.

14. Hagfeldt, A.; Graetzel, M. Light-induced redox reactions in nanocrystalline systems. *Chem. Rev.* **1995**, *95,* 49-68.

15. Hoffmann, M. R.; Martin, S. T.; Choi, W.; Bahnemann, D. W. Environmental applications of semiconductor photocatalysis. *Chem. Rev.* **1995**, *95,* 69-96.

16. Liu, Y.; Li, J.; Qiu, X.; Burda, C. Novel TiO_2 nanocatalysts for wastewater purification: tapping energy from the sun. *Water Sci. Technol.* **2006**, *54,* 47-54.

17. Nel, A.; Xia, T.; Mädler, L.; Li, N. Toxic potential of materials at the nanolevel. *Science*. **2006**, *311,* 622-627.

18. Berry, C. C.; Wells, S.; Charles, S.; Aitchison, G.; Curtis, A. S. G. Cell response to dextran-derivatised iron oxide nanoparticles post internalisation. *Biomaterials*. **2004**, *25,* 5405-5413.

19. Hussain, S. M.; Hess, K. L.; Gearhart, J. M.; Geiss, K. T.; Schlager, J. J. In vitro toxicity of nanoparticles in BRL 3A rat liver cells. *Toxicol. In Vitro*. **2005**, *19,* 975-983.

20. Gupta, A. K.; Gupta, M. Cytotoxicity suppression and cellular uptake enhancement of surface modified magnetic nanoparticles. *Biomaterials*. **2005**, *26,* 1565-1573.

21. Gupta, A. K.; Wells, S. Surface-modified superparamagnetic nanoparticles for drug delivery: preparation, characterization, and cytotoxicity studies. *IEEE Trans. Nanobioscience.* **2004**, *3*, 66-73.

22. Auffan, M.; Decome, L.; Rose, J.; Orsiere, T.; DeMeo, M.; Briois, V.; Chaneac, C.; Olivi, L.; Berge-Lefranc, J. L.; Botta, A.; Wiesner, M. R.; Bottero, J. Y. In vitro interactions between DMSA-coated maghemite nanoparticles and human fibroblasts: a physicochemical and cyto-genotoxical study. *Environ. Sci. Technol.* **2006**, *40*, 4367-4373.

23. Pisanic II, T. R.; Blackwell, J. D.; Shubayev, V. I.; Finones, R. R.; Jin, S. Nanotoxicity of iron oxide nanoparticle internalization in growing neurons. *Biomaterials*. **2007**, *28*, 2572-2581.

24. Albrecht, C.; Adolf, B.; Weishaupt, C.; Hohr, D.; Zeittrager, I.; Friemann, J.; Borm, P. J. Clara-cell hyperplasia after quartz and coal-dust instillation in rat lung. *Inhal. Toxicol.* **2001**, *13*, 191-205.

25. Bergmann, J. D.; Metker, L. W.; McCain, W. C.; Beall, P. A.; Michie, M. W.; Lee, R. B. Intratracheal instillation of zinc-cadmium sulfide (ZnCdS) in Fischer 344 rats. *Inhal. Toxicol.* **2000**, *12*, 331-346.

26. Hamilton, R. F., Jr.; Pfau, J. C.; Marshall, G. D.; Holian, A. Silica and PM1648 modify human alveolar macrophage antigen-presenting cell activity in vitro. *J Environ. Pathol. Toxicol. Oncol.* **2001**, *20 Suppl 1*, 75-84.

27. Gurr, J.-R.; Wang, A. S.; Chen, C.-H.; Jan, K.-Y. Ultrafine titanium dioxide particles in the absence of photoactivation can induce oxidative damage to human bronchial epithelial cells. *Toxicology*. **2005**, *213*, 66-73.

28. Sayes, C. M.; Wahi, R.; Kurian, P. A.; Liu, Y.; West, J. L.; Ausman, K. D.; Warheit, D. B.; Colvin, V. L. Correlating nanoscale titania structure with toxicity: a cytotoxicity and inflammatory response study with human dermal fibroblasts and human lung epithelial cells. *Toxicol. Sci.* **2006**, *92*, 174-185.

29. Wang, J. J.; Sanderson, B. J.; Wang, H. Cyto- and genotoxicity of ultrafine TiO_2 particles in cultured human lymphoblastoid cells. *Mutat. Res.* **2007**, *628*, 99-106.

30. Wang, J.; Zhou, G.; Chen, C.; Yu, H.; Wang, T.; Ma, Y.; Jia, G.; Gao, Y.; Li, B.; Sun, J.; Li, Y.; Jiao, F.; Zhao, Y.; Chai, Z. Acute toxicity and biodistribution of different

sized titanium dioxide particles in mice after oral administration. *Toxicol. Lett.* **2007**, *168*, 176-185.

31. Afaq, F.; Abidi, P.; Matin, R.; Rahman, Q. Cytotoxicity, pro-oxidant effects and antioxidant depletion in rat lung alveolar macrophages exposed to ultrafine titanium dioxide. *J. Appl. Toxicol.* **1998**, *18*, 307-312.

32. Warheit, D. B.; Webb, T. R.; Reed, K. L.; Frerichs, S.; Sayes, C. M. Pulmonary toxicity study in rats with three forms of ultrafine-TiO_2 particles: differential responses related to surface properties. *Toxicology*. **2007**, *230*, 90-104.

33. Brayner, R.; Ferrari-Iliou, R.; Brivois, N.; Djediat, S.; Benedetti, M. F.; Fievet, F. Toxicological impact studies based on *Escherichia coli* bacteria in ultrafine ZnO nanoparticles colloidal medium. *Nano Lett.* **2006**, *6*, 866-870.

34. Geiser, M.; Rothen-Rutishauser, B.; Kapp, N.; Schürch, S.; Kreyling, W.; Schulz, H.; Semmler, M.; Im Hof, V.; Heyder, J.; Gehr, P. Ultrafine particles cross cellular membranes by nonphagocytic mechanisms in lungs and in cultured cells. *Environ. Health Perspect.* **2005**, *113*, 1555-1560.

35. Kreyling, W. G.; Semmler, M.; Erbe, F.; Mayer, P.; Takenaka, S.; Schulz, H.; Oberdörster, G.; Ziesenis, A. Translocation of ultrafine insoluble iridium particles from lung epithelium to extrapulmonary organs is size dependent but very low. *J. Toxicol. Environ. Health A.* **2002**, *65*, 1513-1530.

36. Takenaka, S.; Karg, E.; Roth, C.; Schulz, H.; Ziesenis, A.; Heinzmann, U.; Schramel, P.; Heyder, J. Pulmonary and systemic distribution of inhaled ultrafine silver particles in rats. *Environ. Health Perspect.* **2001**, *109*, 547-551.

37. Meiring, J. J.; Borm, P. J.; Bagate, K.; Semmler, M.; Seitz, J.; Takenaka, S.; Kreyling, W. G. The influence of hydrogen peroxide and histamine on lung permeability and translocation of iridium nanoparticles in the isolated perfused rat lung. *Part Fibre. Toxicol.* **2005**, *2*, 3.

38. Oberdörster, G.; Sharp, Z.; Atudorei, V.; Elder, A.; Gelein, R.; Kreyling, W.; Cox, C. Translocation of inhaled ultrafine particles to the brain. *Inhal. Toxicol.* **2004**, *16*, 437-445.

39. Lockman, P. R.; Koziara, J. M.; Mumper, R. J.; Allen, D. D. Nanoparticle surface charges alter blood-brain barrier integrity and permeability. *J. Drug Target.* **2004**, *12,* 635-641.

40. Oberdörster, G.; Oberdörster, E.; Oberdörster, J. Nanotoxicology: an emerging discipline evolving from studies of ultrafine particles. *Environ. Health Perspect.* **2005**, *113,* 823-839.

41. Block, M. L.; Hong, J. S. Microglia and inflammation-mediated neurodegeneration: multiple triggers with a common mechanism. *Prog. Neurobiol.* **2005**, *76,* 77-98.

42. Colton, C. A.; Chernyshev, O. N.; Gilbert, D. L.; Vitek, M. P. Microglial contribution to oxidative stress in Alzheimer's disease. *Ann. N. Y. Acad. Sci.* **2000**, *899,* 292-307.

43. Liu, B.; Hong, J. S. Role of microglia in inflammation-mediated neurodegenerative diseases: mechanisms and strategies for therapeutic intervention. *J. Pharmacol. Exp. Ther.* **2003**, *304,* 1-7.

44. Streit, W. J.; Mrak, R. E.; Griffin, W. S. Microglia and neuroinflammation: a pathological perspective. *J. Neuroinflammation.* **2004**, *1,* 14.

45. Fariss, M. W.; Chan, C. B.; Patel, M.; Van, H. B.; Orrenius, S. Role of mitochondria in toxic oxidative stress. *Mol. Interv.* **2005**, *5,* 94-111.

46. Kreutzberg, G. W. Microglia: a sensor for pathological events in the CNS. *Trends Neurosci.* **1996**, *19,* 312-318.

47. Streit, W. J.; Conde, J. R.; Fendrick, S. E.; Flanary, B. E.; Mariani, C. L. Role of microglia in the central nervous system's immune response. *Neurol. Res.* **2005**, *27,* 685-691.

48. Block, M. L.; Zecca, L.; Hong, J. S. Microglia-mediated neurotoxicity: uncovering the molecular mechanisms. *Nat. Rev. Neurosci.* **2007**, *8,* 57-69.

49. Stoimenov, P. K.; Klinger, R. L.; Marchin, G. L.; Klabunde, K. J. Metal oxide nanoparticles as bactericidal agents. *Langmuir.* **2002**, *18,* 6679-6686.

50. Adams, L. K.; Lyon, D. Y.; McIntosh, A.; Alvarez, P. J. Comparative toxicity of nano-scale TiO_2, SiO_2 and ZnO water suspensions. *Water Sci. Technol.* **2006**, *54*, 327-334.

51. Pal, S.; Tak, Y. K.; Song, J. M. Does the antibacterial activity of silver nanoparticles depend on the shape of the nanoparticle? A study of the Gram-negative bacterium *Escherichia coli*. *Appl. Environ. Microbiol.* **2007**, *73*, 1712-1720.

52. Sondi, I.; Salopek-Sondi, B. Silver nanoparticles as antimicrobial agent: a case study on *E. coli* as a model for Gram-negative bacteria. *J. Colloid Interface Sci.* **2004**, *275*, 177-182.

53. Morones, J. R.; Elechiguerra, J. L.; Camacho, A.; Holt, K.; Kouri, J. B.; Ramírez, J. T.; Yacaman, M. J. The bactericidal effect of silver nanoparticles. *Nanotechnology*. **2005**, *16*, 2346-2353.

54. Lok, C. N.; Ho, C. M.; Chen, R.; He, Q. Y.; Yu, W. Y.; Sun, H.; Tam, P. K. H.; Chiu, J. F.; Che, C. M. Proteomic analysis of the mode of antibacterial action of silver nanoparticles. *J. Proteome Res.* **2006**, *5*, 916-924.

55. Tong, Z.; Bischoff, M.; Nies, L.; Applegate, B.; Turco, R. F. Impact of fullerene (C_{60}) on a soil microbial community. *Environ. Sci. Technol.* **2007**, *41*, 2985-2991.

56. Lyon, D. Y.; Fortner, J. D.; Sayes, C. M.; Colvin, V. L.; Hughe, J. B. Bacterial cell association and antimicrobial activity of a C_{60} water suspension. *Environ. Toxicol. Chem.* **2005**, *24*, 2757-2762.

57. Thill, A.; Zeyons, O.; Spalla, O.; Chauvat, F.; Rose, J.; Auffan, M.; Flank, A. M. Cytotoxicity of CeO_2 nanoparticles for *Escherichia coli*. Physico-chemical insight of the cytotoxicity mechanism. *Environ. Sci. Technol.* **2006**, *40*, 6151-6156.

58. Huang, L.; Li, D. Q.; Lin, Y. J.; Wei, M.; Evans, D. G.; Duan, X. Controllable preparation of Nano-MgO and investigation of its bactericidal properties. *J. Inorg. Biochem.* **2005**, *99*, 986-993.

59. Tang, Y. J.; Ashcroft, J. M.; Chen, D.; Min, G.; Kim, C. H.; Murkhejee, B.; Larabell, C.; Keasling, J. D.; Chen, F. F. Charge-associated effects of fullerene derivatives on microbial structural integrity and central metabolism. *Nano Lett.* **2007**, *7*, 754-760.

60. Oberdörster, E. Manufactured nanomaterials (fullerenes, C_{60}) induce oxidative stress in the brain of juvenile largemouth bass. *Environ. Health Perspect.* **2004**, *112*, 1058-1062.

61. US House of Representatives, Office of Science. In *Environmental and Safety Impacts of Nanotechnology: What Research is Needed?* *http://www.house.gov/science/press/109/109-165.htm*; 2005.

62. Dunphy Guzmán, K. A.; Taylor, M. R.; Banfield, J. F. Environmental risks of nanotechnology: National Nanotechnology Initiative funding, 2000-2004. *Environ. Sci. Technol.* **2006**, *40*, 1401-1407.

63. Allen, N. S.; Edge, M.; Sandoval, G.; Verran, J.; Stratton, J.; Maltby, J. Photocatalytic coatings for environmental applications. *Photochem. Photobiol.* **2005**, *81*, 279-290.

64. Fisher, J.; Egerton, T. Titanium Compounds, Inorganic. In *Kirk-Othmer Encyclopedia of Chemical Technology*, John Wiley & Sons: New York, 2001.

65. Choi, H.; Stathatos, E.; Dionysiou, D. D. Sol-gel preparation of mesoporous photocatalytic TiO_2 films and TiO_2/Al_2O_3 composite membranes for environmental applications. *Appl Catal B-Environ*. **2006**, *63*, 60-67.

66. Konstantinou, I. K.; Albanis, T. A. TiO_2-assisted photocatalytic degradation of azo dyes in aqueous solution: kinetic and mechanistic investigations: A review. *Appl Catal B-Environ*. **2004**, *49*, 1-14.

67. Balasubramanian, G.; Dionysiou, D. D.; Suidan, M. T.; Baudin, I.; Laîné, J. M. Evaluating the activities of immobilized TiO_2 powder films for the photocatalytic degradation of organic contaminants in water. *Appl Catal B-Environ*. **2004**, *47*, 73-84.

68. Wolf, R.; Matz, H.; Orion, E.; Lipozencic, J. Sunscreens--the ultimate cosmetic. *Acta Dermatovenerol. Croat.* **2003**, *11*, 158-162.

69. Kaida, T.; Kobayashi, K.; Adachi, M.; Suzuki, F. Optical characteristics of titanium oxide interference film and the film laminated with oxides and their applications for cosmetics. *J. Cosmet. Sci.* **2004**, *55*, 219-220.

70. Bermudez, E.; Mangum, J. B.; Wong, B. A.; Asgharian, B.; Hext, P. M.; Warheit, D. B.; Everitt, J. I. Pulmonary responses of mice, rats, and hamsters to subchronic inhalation of ultrafine titanium dioxide particles. *Toxicol. Sci.* **2004**, *77*, 347-357.

71. Oberdörster, G.; Finkelstein, J. N.; Johnston, C.; Gelein, R.; Cox, C.; Baggs, R.; Elder, A. C. Acute pulmonary effects of ultrafine particles in rats and mice. *Res. Rep. Health Eff. Inst.* **2000**, *96*, 5-74.

72. Warheit, D. B.; Brock, W. J.; Lee, K. P.; Webb, T. R.; Reed, K. L. Comparative pulmonary toxicity inhalation and instillation studies with different TiO_2 particle formulations: impact of surface treatments on particle toxicity. *Toxicol. Sci.* **2005**, *88*, 514-524.

73. Zhang, A. P.; Sun, Y. P. Photocatalytic killing effect of TiO_2 nanoparticles on Ls-174-t human colon carcinoma cells. *World J Gastroenterol.* **2004**, *10*, 3191-3193.

74. Ramires, P. A.; Romito, A.; Cosentino, F.; Milella, E. The influence of titania/hydroxyapatite composite coatings on in vitro osteoblasts behaviour. *Biomaterials*. **2001**, *22*, 1467-1474.

75. Peters, K.; Unger, R. E.; Kirkpatrick, C. J.; Gatti, A. M.; Monari, E. Effects of nano-scaled particles on endothelial cell function in vitro: studies on viability, proliferation and inflammation. *J Mater. Sci. Mater. Med.* **2004**, *15*, 321-325.

76. Wamer, W. G.; Yin, J. J.; Wei, R. R. Oxidative damage to nucleic acids photosensitized by titanium dioxide. *Free Radic. Biol. Med.* **1997**, *23*, 851-858.

77. Renwick, L. C.; Donaldson, K.; Clouter, A. Impairment of alveolar macrophage phagocytosis by ultrafine particles. *Toxicol. Appl. Pharmacol.* **2001**, *172*, 119-127.

78. Beck-Speier, I.; Dayal, N.; Karg, E.; Maier, K. L.; Roth, C.; Ziesenis, A.; Heyder, J. Agglomerates of ultrafine particles of elemental carbon and TiO_2 induce generation of lipid mediators in alveolar macrophages. *Environ. Health Perspect.* **2001**, *109 Suppl 4*, 613-618.

79. Nakagawa, Y.; Wakuri, S.; Sakamoto, K.; Tanaka, N. The photogenotoxicity of titanium dioxide particles. *Mutat. Res.* **1997**, *394*, 125-132.

80. Nemmar, A.; Hoet, P. H.; Vanquickenborne, B.; Dinsdale, D.; Thomeer, M.; Hoylaerts, M. F.; Vanbilloen, H.; Mortelmans, L.; Nemery, B. Passage of inhaled particles into the blood circulation in humans. *Circulation*. **2002**, *105,* 411-414.

81. Samet, J. M.; DeMarini, D. W.; Malling, H. V. Do airborne particles induce heritable mutations? *Science*. **2004**, *304*, 971-972.

82. Lockman, P.; Oyewumi, M.; Koziara, J.; Roder, K.; Mumper, R.; Allen, D. Brain uptake of thiamine-coated nanoparticles. *J. Controlled Release*. **2003**, *93,* 271-282.

83. Colton, C. A.; Gilbert, D. L. Production of superoxide anions by a CNS macrophage, the microglia. *FEBS Lett.* **1987**, *223,* 284-288.

84. Segal, A. W.; Abo, A. The biochemical basis of the NADPH oxidase of phagocytes. *Trends Biochem. Sci.* **1993**, *18,* 43-47.

85. De Giorgi, F.; Lartigue, L.; Bauer, M. K.; Schubert, A.; Grimm, S.; Hanson, G. T.; Remington, S. J.; Youle, R. J.; Ichas, F. The permeability transition pore signals apoptosis by directing Bax translocation and multimerization. *FASEB J.* **2002**, *16,* 607-609.

86. Fernandes, M. A.; Santos, M. S.; Vicente, J. A.; Moreno, A. J.; Velena, A.; Duburs, G.; Oliveira, C. R. Effects of 1,4-dihydropyridine derivatives (cerebrocrast, gammapyrone, glutapyrone, and diethone) on mitochondrial bioenergetics and oxidative stress: a comparative study. *Mitochondrion.* **2003**, *3,* 47-59.

87. Oberdörster, G.; Maynard, A.; Donaldson, K.; Castranova, V.; Fitzpatrick, J.; Ausman, K.; Carter, J.; Karn, B.; Kreyling, W.; Lai, D.; Olin, S.; Monteiro-Riviere, N.; Warheit, D.; Yang, H. Principles for characterizing the potential human health effects from exposure to nanomaterials: elements of a screening strategy. *Part. Fibre Toxicol.* **2005**, *2*.

88. Wu, X. F.; Block, M. L.; Zhang, W.; Qin, L.; Wilson, B.; Zhang, W. Q.; Veronesi, B.; Hong, J. S. The role of microglia in paraquat-induced dopaminergic neurotoxicity. *Antioxid. Redox. Signal.* **2005**, *7,* 654-661.

89. Block, M. L.; Wu, X.; Pei, Z.; Li, G.; Wang, T.; Qin, L.; Wilson, B.; Yang, J.; Hong, J. S.; Veronesi, B. Nanometer size diesel exhaust particles are selectively toxic to dopaminergic neurons: the role of microglia, phagocytosis, and NADPH oxidase. *FASEB J.* **2004**, *18,* 1618-1620.

90. Shafer, L. L.; McNulty, J. A.; Young, M. R. Brain activation of monocyte lineage cells: brain-derived soluble factors differentially regulate BV2 microglia and peripheral macrophage immune functions. *Neuroimmunomodulation.* **2002**, *10*, 283-294.

91. Kirchnerova, J.; Herrera Cohen, M.-L.; Guy, C.; Klvana, D. Photocatalytic oxidation of n-butanol under fluorescent visible light lamp over commercial TiO_2 (Hombicat UV100 and Degussa P25). *App. Cat. A.* **2005**, *282*, 321-332.

92. Dionysiou, D.; Suidan, M.; Bekoua, E.; Baudin, I.; Lainé, J.-M. Effect of ionic strength and hydrogen peroxide on the photocatalytic degradation of 4-chlorobenzoic acid in water. *App. Cat. B.* **2000**, *26*, 153-171.

93. Lide, D. *CRC Handbook of Chemistry and Physics*; CRC Press: Boca Raton, FL, 2005.

94. Dutta, P. K.; Ray, A. K.; Sharma, V. K.; Millero, F. J. Adsorption of arsenate and arsenite on titanium dioxide suspensions. *J Colloid Interface Sci.* **2004**, *278*, 270-275.

95. Invitrogen Corp. Generating and detecting reactive oxygen species. In *The Handbook - A Guide to Fluorescent Probes and Labeling Technologies*, Invitrogen Corporation: Carlsbad, CA, 2005;Chapter 18.2.

96. Hurum, D. C.; Agrios, A. G.; Gray, K. A.; Rajh, T.; Thurnauer, M. Explaining the enhanced photocatalytic activity of Degussa P25 mixed-phase TiO_2 using EPR. *J. Phys. Chem. B.* **2003**, *107*, 4545-4549.

97. Phillips, D. M. Electron microscopy: use of transmission and scanning electron microscopy to study cells in culture. *Methods Cell Biol.* **1998**, *57*, 297-311.

98. Ferguson, M. A.; Hoffmann, M. R.; Hering, J. G. TiO_2-photocatalyzed As(II) oxidation in aqueous suspensions: reaction kinetics and effects of adsorption. *Environ. Sci. Technol.* **2005**, *39*, 1880-1886.

99. Limbach, L. K.; Li, Y.; Grass, R. N.; Brunner, T. J.; Hintermann, M. A.; Muller, M.; Gunther, D.; Stark, W. J. Oxide nanoparticle uptake in human lung fibroblasts: effects of particle size, agglomeration, and diffusion at low concentrations. *Environ. Sci. Technol.* **2005**, *39*, 9370-9376.

100. Geiser, M. Morphological aspects of particle uptake by lung phagocytes. *Microsc. Res. Tech.* **2002**, *57*, 512-522.

101. Rimai, D. S.; Quesnel, D. J.; Busnaia, A. A. The adhesion of dry particles in the nanometer to micrometer-size range. *Coll Surf A (Physiocochemical and Engineering Aspects)*. **2000**, *165*, 3-10.

102. Emerit, J.; Edeas, M.; Bricaire, F. Neurodegenerative diseases and oxidative stress. *Biomed. Pharmacother.* **2004**, *58*, 39-46.

103. Long, T.; Saleh, N.; Phenrat, T.; Swartz, C.; Parker, J.; Lowry, G. V.; Veronesi, B. Metal oxide nanoparticles produce oxidative stress in CNS microglia and neurons: physicochemical, cellular and genomic analysis. *The Toxicologist*. **2006**, *75*.

104. Nagaveni, K.; Hegde, M. S.; Ravishankar, N.; Subbanna, G. N.; Madras, G. Synthesis and structure of nanocrystalline TiO_2 with lower band gap showing high photocatalytic activity. *Langmuir*. **2004**, *20*, 2900-2907.

105. Uchino, T.; Tokunaga, H.; Ando, M.; Utsumi, H. Quantitative determination of OH radical generation and its cytotoxicity induced by TiO_2-UVA treatment. *Toxicol. In Vitro*. **2002**, *16*, 629-635.

106. Kreyling, W. G.; Semmler, M.; Möller, W. Dosimetry and toxicology of ultrafine particles. *J. Aerosol Med.* **2004**, *17*, 140-152.

107. Donaldson, K.; Stone, V. Current hypotheses on the mechanisms of toxicity of ultrafine particles. *Ann. Ist. Super. Sanita*. **2003**, *39*, 405-410.

108. Renwick, L. C.; Brown, D.; Clouter, A.; Donaldson, K. Increased inflammation and altered macrophage chemotactic responses caused by two ultrafine particle types. *Occup. Environ. Med.* **2004**, *61*, 442-447.

109. Veronesi, B.; de Haar, C.; Lee, L.; Oortgiesen, M. The surface charge of visible particulate matter predicts biological activation in human bronchial epithelial cells (BEAS-2B). *Toxicol. Appl. Pharmacol.* **2002**, *178*, 144-154.

110. Veronesi, B.; Oortgiesen, M. Neurogenic inflammation and particulate matter (PM) air pollutants. *Neurotoxicology*. **2001**, *22*, 795-810.

111. Pooler, M.; Makwana, O.; Carter, J.; Beck-Speier I.; Kreyling W.; Veronesi, B. Electrostatic charge on nanoparticles activates CNS macrophages (microglia). *The Toxicologist CD -- An official journal of the Society of Toxicology*. **2005**, *84*.

112. Husemann, J.; Loike, J. D.; Anankov, R.; Febbraio, M.; Silverstein, S. C. Scavenger receptors in neurobiology and neuropathology: their role on microglia and other cells of the nervous system. *Glia*. **2002**, *40*, 195-205.

113. Kim, J. K.; Lee, W. K.; Lee, E. J.; Cho, Y. J.; Lee, K. H.; Kim, H. S.; Chung, Y.; Kim, K. A.; Lim, Y. Mechanism of silica- and titanium dioxide-induced cytotoxicity in alveolar macrophages. *J. Toxicol. Environ. Health A.* **1999**, *58*, 437-450.

114. Afaq, F.; Abidi, P.; Matin, R.; Rahman, Q. Activation of alveolar macrophages and peripheral red blood cells in rats exposed to fibers/particles. *Toxicol. Lett.* **1998**, *99*, 175-182.

115. Long, T. C.; Saleh, N.; Tilton, R. D.; Lowry, G. V.; Veronesi, B. Titanium dioxide (P25) produces reactive oxygen species in immortalized brain microglia (BV2): implications for nanoparticle neurotoxicity. *Environ. Sci. Technol.* **2006**, *40*, 4346-4352.

116. Mattson, M. P. Mechanisms of neuronal apoptosis and excitotoxicity. In *Pathogenesis of neurodegenerative disorders*, 1 ed.; Humana Press: Baltimore, 2001;Chapter 1.

117. Zhou, W.; Hurlbert, M. S.; Schaack, J.; Prasad, K. N.; Freed, C. R. Overexpression of human alpha-synuclein causes dopamine neuron death in rat primary culture and immortalized mesencephalon-derived cells. *Brain Res.* **2000**, *866*, 33-43.

118. Maier, W. E.; Kodavanti, P. R.; Harry, G. J.; Tilson, H. A. Sensitivity of adenosine triphosphatases in different brain regions to polychlorinated biphenyl congeners. *J. Appl. Toxicol.* **1994**, *14*, 225-229.

119. Shi, J. Y.; Chen, J.; Feng, Z. C.; Chen, T.; Lian, Y. X.; Wang, X. L.; Li, C. Photoluminescence characteristics of TiO_2 and their relationship to the photoassisted reaction of water/methanol mixture. *J. Phys. Chem. C.* **2007**, *111*, 693-699.

120. Wiesner, M. R.; Lowry, G. V.; Alvarez, P.; Dionysiou, D.; Biswas, P. Assessing the risks of manufactured nanomaterials. *Environ. Sci. Technol.* **2006**, *40*, 4336-4345.

121. Xia, T.; Kovochich, M.; Brant, J.; Hotze, M.; Sempf, J.; Oberley, T.; Sioutas, C.; Yeh, J. I.; Wiesner, M. R.; Nel, A. E. Comparison of the abilities of ambient and manufactured nanoparticles to induce cellular toxicity according to an oxidative stress paradigm. *Nano Lett.* **2006**, *6*, 1794-1807.

122. Tusher, V. G.; Tibshirani, R.; Chu, G. Significance analysis of microarrays applied to the ionizing radiation response. *Proc. Natl. Acad. Sci. U. S. A.* **2001**, *98*, 5116-5121.

123. Pagès, G.; Guérin, S.; Grall, D.; Bonino, F.; Smith, A.; Anjuere, F.; Auberger, P.; Poysségur, J. Defective thymocyte maturation in p44 MAP Kinase (Erk 1) knockout mice. *Science*. **1999**, *286*, 1374-1377.

124. Artuch, R.; Colome, C.; Vilaseca, M. A.; Pineda, M.; Campistol, J. [Ubiquinone: metabolism and functions. Ubiquinone deficiency and its implication in mitochondrial encephalopathies. Treatment with ubiquinone]. *Rev. Neurol.* **1999**, *29*, 59-63.

125. Kroemer, G.; Jaattela, M. Lysosomes and autophagy in cell death control. *Nat. Rev. Cancer.* **2005**, *5*, 886-897.

126. Rothen-Rutishauser, B. M.; Schürch, S.; Haenni, B.; Kapp, N.; Gehr, P. Interaction of fine particles and nanoparticles with red blood cells visualized with advanced microscopic techniques. *Environ. Sci. Technol.* **2006**, *40*, 4353-4359.

127. Rothen-Rutishauser, B.; Muhlfeld, C.; Blank, F.; Musso, C.; Gehr, P. Translocation of particles and inflammatory responses after exposure to fine particles and nanoparticles in an epithelial airway model. *Part. Fibre Toxicol.* **2007**, *4*, 9.

128. Champion, J. A.; Mitragotri, S. Role of target geometry in phagocytosis. *Proc. Natl. Acad. Sci. U. S. A.* **2006**, *103*, 4930-4934.

129. Sabokbar, A.; Pandey, R.; Athanasou, N. A. The effect of particle size and electrical charge on macrophage-osteoclast differentiation and bone resorption. *J. Mater. Sci. Mater. Med.* **2003**, *14*, 731-738.

130. Reilly, C. A.; Veranth, J.; Veronesi, B.; Yost, G. S. Vanilloid receptors in the respiratory tract. In *Toxicology of the Lung (vol 22)*, Fourth ed.; Gardner, D. E. Ed.; CRC Press: Boca Raton, 2006;Chapter 8.

131. Kim, S. R.; Lee, D. Y.; Chung, E. S.; Oh, U. T.; Kim, S. U.; Jin, B. K. Transient receptor potential vanilloid subtype 1 mediates cell death of mesencephalic dopaminergic neurons in vivo and in vitro. *J. Neurosci.* **2005**, *25*, 662-671.

132. Project on Emerging Nanotechnologies. *The Nanotechnology Consumer Product Inventory*; Woodrow Wilson International Center for Scholars: Washington, DC, 2007.

133. Tungittiplakorn, W.; Cohen, C.; Lion, L. W. Engineered polymeric nanoparticles for bioremediation of hydrophobic contaminants. *Environ. Sci. Technol.* **2005**, *39*, 1354-1358.

134. Liu, Y.; Majetich, S. A.; Tilton, R. D.; Sholl, D. S.; Lowry, G. V. TCE dechlorination rates, pathways, and efficiency of nanoscale iron particles with different properties. *Environ. Sci. Technol.* **2005**, *39*, 1338-1345.

135. Tratnyek, P. G.; Johnson, R. L. Nanotechnologies for environmental cleanup. *Nano Today*. **2006**, *1*, 44-48.

136. Nagaveni, K.; Sivalingam, G.; Hegde, M. S.; Madras, G. Photocatalytic degradation of organic compounds over combustion-synthesized nano-TiO_2. *Environ. Sci. Technol.* **2004**, *38*, 1600-1604.

137. Liu, Z.; He, Y.; Li, F.; Liu, Y. Photocatalytic treatment of RDX wastewater with nano-sized titanium dioxide. *Environ. Sci. Pollut. Res. Int.* **2006**, *13*, 328-332.

138. Maynard, A. D.; Aitken, R. J.; Butz, T.; Colvin, V.; Donaldson, K.; Oberdörster, G.; Philbert, M. A.; Ryan, J.; Seaton, A.; Stone, V.; Tinkle, S. S.; Tran, L.; Walker, N. J.; Warheit, D. B. Safe handling of nanotechnology. *Nature*. **2006**, *444*, 267-269.

139. Ponder, S. M.; Darab, J. G.; Mallouk, T. E. Remediation of Cr(VI) and Pb(II) aqueous solutions using supported, nanoscale zero-valent iron. *Environ. Sci. Technol.* **2000**, *34*, 2564-2569.

140. Zhang, Q. L.; Lin, Y. C.; Chen, X.; Gao, N. Y. A method for preparing ferric activated carbon composites adsorbents to remove arsenic from drinking water. *J. Hazard. Mater*. **2007**.

141. Lay, J. C.; Bennett, W. D.; Ghio, A. J.; Bromberg, P. A.; Costa, D. L.; Kim, C. S.; Koren, H. S.; Devlin, R. B. Cellular and biochemical response of the human lung after intrapulmonary instillation of ferric oxide particles. *Am. J. Respir. Cell Mol. Biol.* **1999**, *20*, 631-642.

142. Nurmi, J. T.; Tratnyek, P. G.; Sarathy, V.; Baer, D. R.; Amonette, J. E.; Pecher, K.; Wang, C.; Linehan, J. C.; Matson, D. W.; Penn, R. L.; Driessen, M. D. Characterization and properties of metallic iron nanoparticles: spectroscopy, electrochemistry, and kinetics. *Environ. Sci. Technol.* **2005**, *39*, 1221-1230.

143. Blattner, F. R.; Plunkett, G.; Bloch, C. A.; Perna, N. T.; Burland, V.; Riley, M.; ColladoVides, J.; Glasner, J. D.; Rode, C. K.; Mayhew, G. F.; Gregor, J.; Davis, N. W.; Kirkpatrick, H. A.; Goeden, M. A.; Rose, D. J.; Mau, B.; Shao, Y. The complete genome sequence of *Escherichia coli* K-12. *Science*. **1997**, *277*, 1453-&.

144. Blanco, M.; Urios, A.; Martinez, A. New *Escherichia coli* WP2 tester strains highly sensitive to reversion by oxidative mutagens. *Mutat. Res.* **1998**, *413*, 95-101.

145. Maron, D. M.; Ames, B. N. Revised methods for the *Salmonella* mutagenicity test. *Mutat. Res.* **1983**, *113*, 173-215.

146. Wu, Z. J.; Irizarry, R. A.; Gentleman, R.; Martinez-Murillo, F.; Spencer, F. A model-based background adjustment for oligonucleotide expression arrays. *J Am. Stat. Assoc.* **2004**, *99*, 909-917.

147. Benjamini, Y.; Hochberg, Y. Controlling the false discovery rate: a practical and powerful approach to multiple testing. *J. R. Stat. Soc. , Ser. B, Methodol.* **2006**, *57*, 289-300.

148. Mortelmans, K.; Zeiger, E. The Ames *Salmonella*/microsome mutagenicity assay. *Mutat. Res.* **2000**, *455*, 29-60.

149. Williams, G. J.; Breazeale, S. D.; Raetz, C. R. H.; Naismith, J. H. Structure and function of both domains of ArnA, a dual function decarboxylase and a formyltransferase, involved in 4-amino-4-deoxy-L-arabinose biosynthesis. *J. Biol. Chem.* **2005**, *280*, 23000-23008.

150. Meddows, T. R.; Savory, A. P.; Grove, J. I.; Moore, T.; Lloyd, R. G. RecN protein and transcription factor DksA combine to promote faithful recombinational repair of DNA double-strand breaks. *Molecular Microbiology*. **2005**, *57*, 97-110.

151. Gogniat, G.; Thyssen, M.; Denis, M.; Pulgarin, C.; Dukan, S. The bactericidal effect of TiO_2 photocatalysis involves adsorption onto catalyst and the loss of membrane integrity. *FEMS Microbiol. Lett.* **2006**, *258,* 18-24.

152. Warheit, D. B.; Hoke, R. A.; Finlay, C.; Donner, E. M.; Reed, K. L.; Sayes, C. M. Development of a base set of toxicity tests using ultrafine TiO_2 particles as a component of nanoparticle risk management. *Toxicol. Lett.* **2007**, *doi:10.1016/j.toxlet.2007.04.008*.

153. Chen, Y.; Suzuki, I. Effect of uncouplers on endogenous respiration and ferrous iron oxidation in a chemolithoautotrophic bacterium *Acidithiobacillus* (*Thiobacillus*) *ferrooxidans*. *FEMS Microbiol. Lett.* **2004**, *237,* 139-145.

154. Gage, D. J.; Neidhardt, F. C. Adaptation of *Escherichia coli* to the uncoupler of oxidative phosphorylation 2,4-dinitrophenol. *J. Bacteriol.* **1993**, *175,* 7105-7108.

155. Glasauer, S.; Langley, S.; Beveridge, T. J. Intracellular iron minerals in a dissimilatory iron-reducing bacterium. *Science*. **2002**, *295,* 117-119.

156. Ajayan, P. M.; Marks, L. D. Quasimelting and phases of small particles. *Phys. Rev. Lett.* **1988**, *60,* 585.

157. Stumm, W.; Morgan, J. J. *Aquatic Chemistry: Chemical Equilibria and Rates in Natural Waters*; John Wiley & Sons: New York, NY, 1996.

158. Limbach, L. K.; Wick, P.; Manser, P.; Grass, R. N.; Bruinink, A.; Stark, W. J. Exposure of engineered nanoparticles to human lung epithelial cells: influence of chemical composition and catalytic activity on oxidative stress. *Environ. Sci. Technol.* **2007**, *41,* 4158-4163.

159. Cho, A. K.; Sioutas, C.; Miguel, A. H.; Kumagai, Y.; Schmitz, D. A.; Singh, M.; Eiguren-Fernandez, A.; Froines, J. R. Redox activity of airborne particulate matter at different sites in the Los Angeles Basin. *Environ Res.* **2005**, *99,* 40-47.

160. Warheit, D. B.; Webb, T. R.; Colvin, V. L.; Reed, K. L.; Sayes, C. M. Pulmonary bioassay studies with nanoscale and fine-quartz particles in rats: toxicity is not dependent upon particle size but on surface characteristics. *Toxicol. Sci.* **2007**, *95,* 270-280.

161. Duffin, R.; Tran, L.; Brown, D.; Stone, V.; Donaldson, K. Proinflammogenic effects of low-toxicity and metal nanoparticles in vivo and in vitro: highlighting the role of particle surface area and surface reactivity. *Inhal. Toxicol.* **2007**, *19*, 849-856.

162. Monteiller, C.; Tran, L.; MacNee, W.; Faux, S.; Jones, A.; Miller, B.; Donaldson, K. The pro-inflammatory effects of low-toxicity low-solubility particles, nanoparticles and fine particles, on epithelial cells in vitro: the role of surface area. *Occup. Environ. Med.* **2007**, *64*, 609-615.

163. Donaldson, K. Resolving the nanoparticles paradox. *Nanomedicine*. **2006**, *1*, 229-234.

164. Borm, P. J.; Müller-Schulte, D. Nanoparticles in drug delivery and environmental exposure: same size, same risks? *Nanomedicine*. **2006**, *1*, 235-249.

165. Duffin, R.; Mills, N. L.; Donaldson, K. Nanoparticles-a thoracic toxicology perspective. *Yonsei Med. J.* **2007**, *48*, 561-572.

166. Albrecht, C.; Knaapen, A. D.; Becker, A.; Höhr, D.; Haberzettl, P.; van Schooten, F. J.; Borm, P. J.; Schins, R. P. F. The crucial role of particle surface reactivity in respirable quartz-induced reactive oxygen/nitrogen species formation and APE/Ref-I induction in rat lung. *Respir. Res.* **2005**, *6*, 129.

167. Lam, C. W.; James, J. T.; McCluskey, R.; Arepalli, S.; Hunter, R. L. A review of carbon nanotube toxicity and assessment of potential occupational and environmental health risks. *Crit. Rev. Toxicol.* **2006**, *36*, 189-217.

168. Van Nooten T.; Lieben, F.; Dries, J.; Pirard, E.; Springael, D.; Bastiaens, L. Impact of microbial activities on the mineralogy and performance of column-scale permeable reactive iron barriers operated under two different redox conditions. *Environ Sci. Technol.* **2007**, *41*, 5724-5730.

169. Da Silva, M. L. B.; Johnson, R. L.; Alvarez, P. J. J. Microbial characterization of groundwater undergoing treatment with a permeable reactive iron barrier. *Environ. Eng. Sci.* **2007**, *24*, 1122-1127.

170. Cho, I. H.; Park, J. H.; Kim, Y. G. Oxidative degradation and toxicity reduction of trichloroethylene (TCE) in water using TiO_2/solar light: comparative study of TiO_2 slurry and immobilized systems. *J. Environ. Sci. Health A Tox. Hazard. Subst. Environ. Eng*. **2005**, *40*, 1033-1044.

171. Kuo, W. S.; Ho, P. H. Solar photocatalytic decolorization of methylene blue in water. *Chemosphere*. **2001**, *45*, 77-83.